INVESTIGATION OF K^* PRODUCTION BY 6 GeV/c K^- INCIDENT ON LIQUID HYDROGEN

by

USHA MALLIK

A dissertation submitted to the Graduate Faculty in Physics in partial fulfillment of the requirements for the degree of Doctor of Philosophy, The City University Of New York.

1978

This manuscript has been read and accepted for the Graduate Faculty in Physics in satisfaction of the dissertation requirement for the degree of Doctor of Philosophy.

6/13/78
date

Chairman of Examining Committee

7/22/78
date

Executive Officer

Supervisory Committee

The City University of New York

ABSTRACT

INVESTIGATION OF K^* PRODUCTION BY 6 GeV/c K^-

INCIDENT ON LIQUID HYDROGEN

by

USHA MALLIK

Advisor: Professor Seymour J. Lindenbaum

We have studied the reaction $K^- + p \rightarrow \bar{K}^0\pi^+\pi^- + n$ at an incident K^- momentum of 6 GeV/c. The experiment was carried out using the Multi-Particle Spectrometer (MPS) facility at the Brookhaven National Laboratory. The Alternating Gradient Synchrotron supplied a Medium Energy Separated Beam of $\sim 10^4$ K^- per AGS spill. The neutron recoil was obtained by selecting on the missing mass.

The data sample consisted of $\sim$ 14,000 events and represents the largest statistics in the $K^0_s\pi^-\pi^+$ mode in any experiment performed so far. The $K^*(1420)$ peak as well as a second peak at $\sim$ 1750 MeV were observed in the $K^0_s\pi^-\pi^+$ effective mass spectrum. The total cross sections for both the peaks were obtained. The 1420 mass region was studied at various t intervals and the differential cross section as a function of t was calculated.

ACKNOWLEDGEMENTS

The Multi Particle Spectrometer was a long awaited facility which became a reality by the end of 1974. The current experiment was run in two parts, the Fall of 1975 and the Winter of 1976. This experiment, because of its complexity and the vast size of the apparatus used, involved many individuals both directly and indirectly. First, the author is deeply indebted to Professor Seymour J. Lindenbaum, the author's thesis advisor, for the experimental idea, encouragement and inspiration. The author also expresses her deep gratitude for Dr. Satoshi Ozaki, for his continuous assistance and guidance.

Warmest thanks are due to Drs. Kenneth J. Foley, J. Harvey Goldman, Martin A. Kramer, William A. Love, Thomas W. Morris, Alfred C. Saulys, and Erich H. Willen for their physics insights and valuable help. Most sincere thanks are expressed towards Drs. Asher Etkin, Anthony A. Fainberg, Stephen Jacobs, I.J. Kim, Edward D. Platner, and C. Dean Wheeler for their professional expertise.

The author is grateful for the assistance of Steven E. Eiseman, Carl L. Jacobs and the MPS group technicians: H. Arnesen, A. Bono, D. Brady, M. Conforte, T. Cannizzo, D. David, S. Hasselriis, L. Hawkins, G. Leigh, W. Lundgren. T. Mogavero, C. Nielson, A. Roesch, L. Toler and R. Wheeler. The author also thanks the staff of the Brookhaven On-Line Data Facility, D. Bartolomeo, L. Davis, A. Friedman, J. Gould, R. Imossi, H. Langenbach, and C. Zein for their contribution to this experiment.

Efforts of Ms. Elizabeth Russell, Ms. Jeanne Scully, and Ms. Sharon Smith, in typing and preparing the manuscript are thankfully acknowledged. The author is appreciative of the efforts of the staff of the Illustration and the Photography in preparing the graphic materials.

Last but not the least the valuable discussions with and the encouragements of Drs. Edward O. Salant and Nicholas P. Samios are greatly appreciated.

TABLE OF CONTENTS

TABLE OF CONTENTS (Cont'd.)

TABLE OF CONTENTS (Cont'd.)

TABLE OF CONTENTS (Cont'd.)

LIST OF TABLES

LIST OF TABLES (Cont'd.)

TABLE

LIST OF FIGURES

LIST OF FIGURES (Cont'd.)

CHAPTER I

INTRODUCTION

1. Experiment

The present experiment was performed to investigate the K^* phenomena in the $K\pi\pi$ decay mode through the following reaction

$$K^- + p \rightarrow \bar{K}^{*o} + n \qquad (1)$$
$$\bar{K}^{*o} \rightarrow K^o_s \pi^+\pi^-$$
$$K^o_s \rightarrow \pi^+\pi^-$$

The charge exchange channel was selected in order to avoid the high background problem of the diffractive channels. Furthermore, this decay mode was of interest since K^*'s of both natural and the unnatural spin-parity can decay into the $K\pi\pi$ final state. The $K\pi$ final state, in contrast, is limited to only the K^*'s of the natural spin-parity.

The experiment was carried out using the Multiparticle Spectrometer (MPS) and the Alternating Gradient Synchrotron (AGS) of Brookhaven National Laboratory (BNL). A 6 GeV/c incident K^- beam from the Medium Energy Separated Beam (MESB) was incident on a 50 cm long liquid hydrogen target. The target was placed inside the main spectrometer magnet along with the particle detectors; this provided a large solid angle acceptance for multiparticle final states. For 10^4 incident K^- available per AGS spill and an average acceptance of 20% in the mass region of 1.1 to 2.0 GeV a sensitivity of $\sim$ 10 events per hour per μb of $\sigma \cdot BR$ (a product of the production cross section and the branching ratio) was estimated.

2. Motivation

The status of the K^*'s at the time of planning of the experiment in 1973 was far from clear. The $K^*(890)$ was perhaps the only well-understood member of the family. The $K^*(1420)$ peak clearly contained at least a $J^P = 2^+$ resonance. The observed mass asymmetry on the two sides of $K^*(1420)$, the 'Q' region, the 'L' region and the strange member of the 3^- meson nonet needed a great deal of attention. For a better understanding it was important to have an experiment with good statistics and a low enough background. In 1974 a great deal of excitement took place with the discovery of the narrow resonance J/ψ. States corresponding to the radial and the orbital excitation were observed in the $q\bar{q}$ meson model with the charmed quarks. Also from this point of view, a new look at the 'old' spectroscopy was (and still is) very important to unravel the corresponding states in the non-charmed mesons.

3. Current Status

Table 1 is a current compilation of the $K\pi$ and/or $K\pi\pi$ resonances, some of which are established and some claimed by one or more groups. Table 2 lists the SU(3) nonets with which the various strange meson members are assumed to be associated.

a. Natural Spin-Parity Series:

[$J^P = 0^+$ strange mesons]

$\kappa(1250)$, the strange member of the '0^+ nonet' (Ref. 3) was observed in the following three reactions:

i. $K^-p \to (K^-\pi^+)n$ at 10 and 16 GeV/c by the Aachen-Berlin-CERN-London-Vienna collaboration (Ref. 4). The mass and width reported

TABLE 1

A Current Compilation of Strange Meson Resonances†

STATE	MASS	WIDTH	J^P	OBSERVED DECAY MODES
$K^*(890)$	892.2 ± 0.5	49.4 ± 1.8	1^-	$K\pi$
$\kappa(1250)$	1250 ± 100	~450	0^+	$K\pi$
$Q_1(1290)$	~1290	~210	1^+	$K\rho$ $\kappa\pi, K\omega, K\epsilon, K^*\pi$
$Q_2(1400)$	~1400	~190	1^+	$K^*\pi$ $\kappa\pi, K\epsilon, K\rho$
$\kappa'(1425)$	~1425	~250	0^+	$K\pi$
$K^*(1420)$	1421 ± 3	108 ± 10	2^+	$K\pi, K^*\pi$ $K\rho, K\omega, K\eta$
$K'(1400)$	~1404	~230	0^-	$K\epsilon, K^*\pi, K\rho$
$K^{*\prime}(1650)$	~1650	~275	1^-	$K\pi$
$L(1760)$	~1765	broad	2^-	$K\pi\pi$
$K^*(1780)$	~1780	~175	3^-	$K\pi, K\pi\pi$

† The values of mass and width are from Reference 1 except for those of K* (890) and K* (1420) which are from Reference 2.

TABLE 2

SU(3) $[q\bar{q}]$ CLASSIFICATION OF MESONS:†

	S	I^G	J^P	C_n	
0^- nonet					
$\pi(140)$	0	1^-	0^-	+	
K(496)	±1	1/2	0^-		
$\eta(549)$	0	0^+	0^-	+	
$\eta'(960)$	0	0^+	$(0 \text{ or } 2)^-$	+	
0^+ nonet					
$\delta(970)$	0	1^-	0^+	+	*
$\kappa(1250)$	±1	1/2	0^+		*
S*(993)	0	0^+	0^+	+	*
ϵ (600)	0	0^+	0^+	+	*
1^- nonet					
$\rho(770)$	0	1^+	1^-	-	
K*(890)	±1	1/2	1^-		
$\omega(783)$	0	0^-	1^-	-	
Φ (1019)	0	0^-	1^-	-	
$1^{+(+)}$ nonet					
$A_1(1100)$	0	1^-	1^+	+	*
$Q_A(1335)$	±1	1/2	1^+		
D(1288)	0	0^+	1^+	+	*
E(1420)	0	0^+	1^+	+	*
$1^{+(-)}$ nonet					
B(1235)	0	1^+	1^+	-	
$Q_B(1355)$	±1	1/2	1^+		

TABLE 2

SU (3) $[q\,\bar{q}]$ CLASSIFICATION OF MESONS: (cont'd)

	S	I^G	J^P	C_n	
2^+ nonet					
A_2 (1310)	0	1^-	2^+	+	
K*(1420)	± 1	1/2	2^+		
f (1270)	0	0^+	2^+	+	
f'(1514)	0	0^+	2^+	+	
2^- nonet					
A_3(1640)	0	1^-	2^-	+	*
L(1765)	± 1	1/2	2^-		*
3^- nonet					
g(1680)	0	1^+	3^-	-	
K*(1780)	± 1	1/2	3^-		
ω'(1675)	0	0^-	3^-		*

* Not sufficiently convincing.

Q_A & Q_B are combinations of Q_1 & Q_2.

† complied from Reference 2.

were

$M = 1245 \pm 30$ MeV; $\Gamma = 485 \pm 80$ MeV.

ii. $K^+n \rightarrow (K^+\pi^-)p$ at 4.6, 8.25 and 12 GeV/c (Ref. 5). A broad and smooth resonance-like structure centered around 1250 MeV was claimed in the above case.

iii. $K^\pm p \rightarrow (K^\pm\pi^+)n$, $(K^\pm\pi^+)\Delta^o$

$\rightarrow (K^\pm\pi^-)\Delta^{++}$

at 13 GeV/c (Ref. 1), by a SLAC wire chamber experiment. The mass and width observed were

$M = \sim 1200$ MeV; $\Gamma = \sim 450$ MeV.

$\underline{\kappa'(1425)}$, a heavier strange scaler meson, was also reported by the SLAC group in the reactions described above (Ref. 1). The mass and width given were:

$M = \sim 1425$ MeV; $\Gamma = \sim 250$ MeV.

$\underline{[J^P = 1^-$ strange mesons$]}$

$\underline{K^*(890)}$ has been observed and established by numerous experiments. The parameters in Table 1 are from the Particle Data Group Compilation (Ref. 2).

Evidence of a heavy vector meson $\underline{K^*(1650)}$ was unraveled by the SLAC group in the reaction $K^\pm p \rightarrow K^\pm\pi^+\pi^-p$ at 13 GeV/c (Ref. 1). The mass and width claimed were:

$M = 1650 \pm 50$ MeV; $\Gamma = 275 \pm 50$ MeV.

$\underline{[J^P = 2^+$ strange mesons$]}$

$\underline{K^*(1420)}$ mass and width have been established by numerous groups. Earlier partial wave analysis strongly favored $J^P = 2^+$.

However, the partial wave analysis[†] of the high statistics data of some recent experiments showed the mass of the $J^P = 2^+$ $K^*(1420)$ to be considerably higher than that given in the Particle Data Group compilation (Ref. 2).

i. The SLAC wire chamber 13 GeV/c experiment in the reaction channels mentioned earlier in the discussion of $\kappa(1250)$ deduced the mass and the width

$M = 1434 \pm 7$ MeV; $\Gamma = 100 \pm 4$ MeV.

ii. A BNL-MPS wire chamber experiment, $K^-p \to (K^-\pi^+)n$ at 6 GeV/c (Ref. 6), found

$M = 1433 \pm 3$ MeV; $\Gamma = 96 \pm 14$ MeV.

iii. A CERN collaboration (Aachen-Geneva-Zurich) spark chamber experiment, $K^-p \to \bar{K}^o\pi^+\pi^-n$ at 10 GeV/c (Ref. 7), found

$M = 1428 \pm 7$ MeV, $\Gamma = 118 \pm 10$ MeV.

[$J^P = 3^-$ strange mesons]

The situation was rather unclear in the mass region between 1.65 and 1.8 GeV where mainly higher spin resonances were reported. Reports of structure in $K2\pi$ and $K3\pi$ at $\sim$ 1660 MeV were obtained (three standard deviation effect) in two bubble chamber experiments in the following channels;

$K^-p \to K^-\omega^o p$ at 3.8 GeV/c by Carmony et al. (Ref. 8);

and $K^+p \to K^+\pi^+\pi^-p$

$\to K^o\pi^+\pi^o p$ at 4.97 GeV/c by Jobes et al. (Ref. 9).

---

† Note: The partial wave amplitudes were obtained either by trying to fit the density matrix elements or by trying to describe the scattering amplitudes themselves. In either case the Isobar model was assumed.

Two more bubble chamber experiments observed a four standard deviation bump in K3π spectrum. The reaction channels, the measured mass and the width are listed below:

$K^-p \to K^-\pi^+\pi^-\pi^o p$ at 7.3 GeV/c by a BNL Bubble Chamber Group (Ref. 10) found

$M = 1710 \pm 15$ MeV; $\Gamma = 110 \pm 50$ MeV,

and $K^+p \to K^o\pi^+\pi^+\pi^-p$ at 5.0 GeV/c by Charriere et al. (Ref. 11) found $M = 1660$ MeV; $\Gamma = 60$ MeV.

Ample evidence of a (natural spin-parity) resonance in the neighborhood of 1.76 GeV existed mainly in the Kπ but also in the Kππ channel. One of the earliest experiments to observe the resonance with statistical significance was the following Purdue Group Bubble Chamber study (Ref. 12):

$$K^+n \to K^+\pi^-p$$
$$\to K^o\pi^+\pi^-p$$
$$\to K^+\pi^o\pi^-p$$

at 9 GeV/c. A five standard deviation effect was observed in the Kπ effective mass in which the mass and the width measured were:

$M = 1753 \pm 12$ MeV; $\Gamma = 60 \pm 20$ MeV.

The two Kππ channels together showed a four standard deviation effect where the mass and the width measured were:

$M = 1768 \pm 14$ MeV; $\Gamma = 50 \pm 20$ MeV.

Two more experiments reported on the spin and the parity of a resonance in the region, although the measurements of the mass and the width did not agree. They were $K^+n \to K^+\pi^-p$ at 12 GeV/c (Ref. 13) which found

$M = \sim 1850$ MeV,

a broad resonance with the decay angular distribution consistent with an F-wave, and $K^- p \to K^- \pi^+ n$ at 7.3 GeV/c (Ref. 14); a four standard deviation effect was observed with

$$M = 1760 \text{ MeV}; \quad \Gamma < 80 \text{ MeV}$$

and spin ≠ 0.

Three recent experiments added more information on the subject as follows:

i. $K^- p \to K^- \pi^+ n$ and $K^+ p \to K^+ \pi^- \Delta^{++}$ at 13 GeV/c (Ref. 15)

which found

$$M = 1776 \pm 26 \text{ MeV}; \quad \Gamma = 270 \pm 70 \text{ MeV}.$$

ii. $K^- p \to \bar{K}^o \pi^- p$

$\to K^- \pi^+ n$ at 14.3 GeV/c (Ref. 16) found

$$M = 1780 \pm 30 \text{ MeV}; \quad \Gamma = 120 \pm 40 \text{ MeV}$$

in the non-charge-exchange channel, and

$$M = 1840 \pm 30 \text{ MeV}; \quad \Gamma = 100 \pm 40 \text{ MeV}$$

in the charge exchange channel.

iii. $K^- p \to K^- \pi^+ n$ at 10 and 16 GeV/c (Ref. 17) found

$$M = 1871 \pm 10 \text{ MeV}; \quad \Gamma = 285 \pm 40 \text{ MeV}.$$

The most important contribution towards the establishment of the resonance and its quantum numbers ($J^P = 3^-$) came from the following CERN proton synchrotron experiment:

$$K^+ p \to K^o_s \pi^+ p$$
$$\hookrightarrow \pi^+ \pi^-$$

at 10 GeV/c (Ref. 18), which measured the mass and the width to be

$$M = 1779 \pm 11 \text{ MeV}; \quad \Gamma = 135 \pm 22 \text{ MeV},$$

with very high statistics.

An MPS experiment run almost simultaneously with the present experiment in the channel $K^-p \to K^-\pi^+n$ at 6 GeV/c (Ref. 19) confirmed the $K^*(1780)$ a $J^P = 3^-$ state. The measured mass and the width obtained by a moment analysis of the $K\pi$ system were:

$$M = 1786 \pm 8 \text{ MeV}; \quad \Gamma = 95 \pm 31 \text{ MeV}.$$

Very recently $K^*(1780)$ has been reported in a three-body decay mode by a CERN collaboration (Aachen-Geneva-Zurich) in the reaction $K^-p \to \bar{K}^0\pi^+\pi^-n$ at 10 GeV/c (Ref. 7) which found

$$M = 1812 \pm 28 \text{ MeV}; \quad \Gamma = 181 \pm 24 \text{ MeV},$$

and $J^P = 3^-$ was obtained after a preliminary partial wave analysis.

b. Unnatural Spin-Parity Series:

[$J^P = 0^-$ strange mesons]

K'(1400), a heavy kaon, has been observed by the SLAC group in the reaction $K^\pm p \to K^\pm\pi^+\pi^-p$ at 13 GeV/c (Ref. 1) with mass and width

$$M = \sim 1404 \text{ MeV}; \quad \Gamma = \sim 230 \text{ MeV}.$$

[$J^P = 1^+$, the 'Q' mesons]

There were controversies whether Q_1 (and/or Q_2) was simply a kinematic enhancement (of the "Deck" type) or a real resonance. Three recent experiments studied the Q-region; the SLAC wire chamber experiment, $K^\pm p \to K^\pm\pi^+\pi^-p$ at 13 GeV/c (Ref. 1), the Aachen-Berlin-CERN-London-Vienna collaboration bubble chamber experiment,

$$K^-p \to K^-\pi^+\pi^-p$$
$$\to \bar{K}^0\pi^-\pi^0p \quad \text{at 10, 14 and 16 GeV/c (Ref. 20), and the}$$

Amsterdam-CERN-Nijmegen-Oxford collaborative experiment at CERN,

$$K^-p \to K^-\pi^+\pi^-p$$
$$\to \bar{K}^0\pi^-\pi^0p \quad \text{at 4.2 GeV/c (bubble chamber) (Ref. 21).}$$

All three groups did partial wave analysis on the $K\pi\pi$ system. All the experiments claimed Q_1 as a resonance; however, Q_2 was claimed as a resonance by only the SLAC group (Ref. 1) which had substantially better statistics than the others.

According to the $q\bar{q}$ scheme of meson nonets, two $J^P = 1^+$ strange meson resonances are expected to exist, so, if Q_2 is considered as a resonance, then the corresponding SU(3) members are Q_A and Q_B, a mixture of Q_1 and Q_2 [$J^{PC}(Q_A) = 1^{++}$, $J^{PC}(Q_B) = 1^{+-}$]. The mixing angle is $\sim 45°$ since Q_1 decays into $K\rho$ and Q_2 decays into $K^*\pi$ almost exclusively.

The mass and the width of Q_1 obtained by all three groups were consistent with each other, giving

$$M = \sim 1290 \text{ MeV}; \quad \Gamma = \sim 200 \text{ MeV}$$

(Refs. 1, 20, 21). For Q_2 they were

$$M = \sim 1400 \text{ MeV}; \quad \Gamma = \sim 200 \text{ MeV}$$

(Ref. 1).

[$J^P = 2^-$, The 'L' meson]

There have been many indications of an unnatural spin parity resonance in the mass region between 1.7 and 1.8 GeV in the $K\pi\pi$ diffractive channel (Refs. 22, 23, 24, 25, 26, and 27). This was named L (Ref. 22) and was seen to decay into $K^*(1420)\pi$ (Refs. 23, 24, 25, and 26) and $K^*\rho$ (Ref. 27). After performing partial wave analysis (Ref. 28) the L-structure was found by these authors to be a composite structure due to a summation of several partial waves, none of which resonated.

The mass region above 1900 MeV has also proved to be very rich in terms of the strange meson resonances, however, it will not be discussed here.

CHAPTER II

EXPERIMENTAL SETUP

1. MESB Layout

The Alternating Gradient Synchrotron (AGS) at Brookhaven National Laboratory (BNL) accelerated protons up to 28.5 GeV with a circulating beam intensity of $\sim 10^{13}$ protons per pulse. The accelerator provided $\sim$ 1 sec of beam every 2.4 seconds. The beam was extracted from the AGS ring and was split. One part of the beam was delivered to the B target station where secondary particles for the Medium Energy Separated Beam (MESB) were produced off a tungsten target.

Figure 1 shows the layout of the MESB (Ref. 29). The beam transport system accepted the secondary particles produced at an angle of 6° at the external target B. Quadrupoles Q_1, Q_2, and Q_3 (a triplet) made the beam parallel in the vertical plane before it entered the DC separators, Sep. 1 and Sep. 2. C_1 was an adjustable horizontal collimator (heavimet) which controlled the beam intensity and was set to be 20.3 cm wide. D1, a dipole bending magnet was the momentum selector and bent the beam by 8°. Sep. 1 and Sep. 2 were a pair of (10 m long) parallel plate DC separators with 5.1 cm gap. They operated at an electric field of 86.6 KV/cm (220 KV/inch) and a magnetic field of 300 G and deflected the π^- and $\bar{p}$ beam vertically while leaving the desired K^- beam undeflected. Q_4 and Q_5 formed a quadrupole doublet which focussed the beam vertically at the mass slit M (heavimet) and horizontally at the center of the second collimator C_2. The gap of the mass slit was set at .14 cm as a compromise between the K beam

FIG. 1 LAY-OUT OF THE MESB

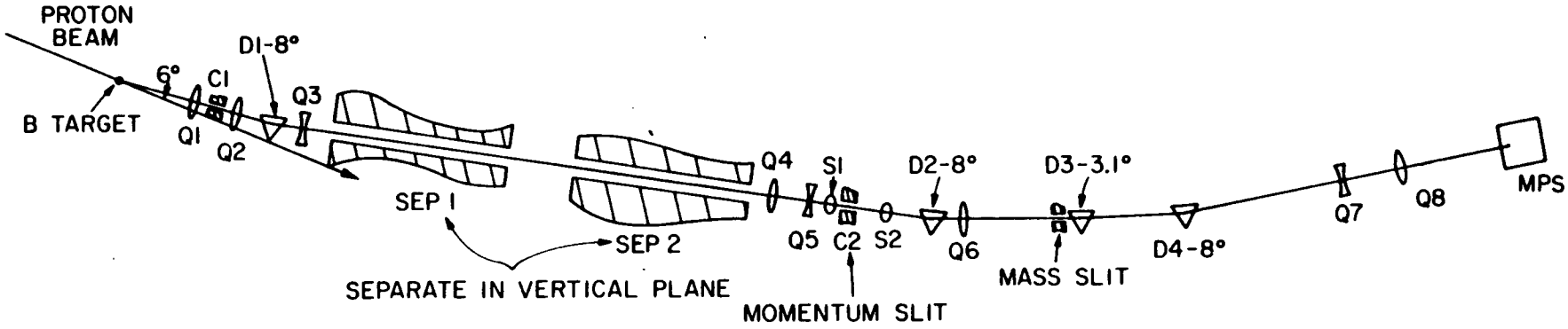

MEDIUM ENERGY SEPARATED BEAM

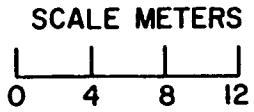

flux and degree of the Kπ separation. The dimension of each plate was 20.5 cm wide x 122 cm long. The spatial separation (between π and K) and the vertical image size at the mass slit were .12 cm and .08 cm (FWHM) respectively giving the effectiveness of separation (defined as image separation/image size) to be 1.5. This gave K flux to π flux ratio of approximately 3 to 2. Q_4 also acted as a field lens for the off-momentum particles. An adjustable horizontal collimator C_2 (identical to C_1) determined the momentum acceptance of the beam. The opening of C_2 was set for $\Delta p/p$ of ± 2.5%. Sextupole S1 reduced chromatic aberration of the vertical image at the mass slit. D_2, a dipole magnet bent the beam by 8° and steered it towards the MPS area. Quad Q6 helped in momentum recombination at the MPS target. Dipole D_3 bent the beam by another 3° and swept out the low energy particles produced in the mass slit. D_4, a dipole magnet, bent the beam by 8° and was used as part of the beam spectrometer to measure the momentum of each incident particle. Q_7 and Q_8 formed a quadrupole doublet and focussed the beam onto the MPS target. The spot size of the beam at the center of the target was 2 cm x 4 cm.

2. Experimental Apparatus

a. Beam Spectrometer:

The momentum of each incident particle was measured by the MPS incident beam spectrometer shown in Fig. 2. Seven pairs of proportional wire chambers (H1 - H7), each of which measured an x and a

FIG. 2 SCHEMATIC DIAGRAM OF THE INCIDENT BEAM SPECTROMETER

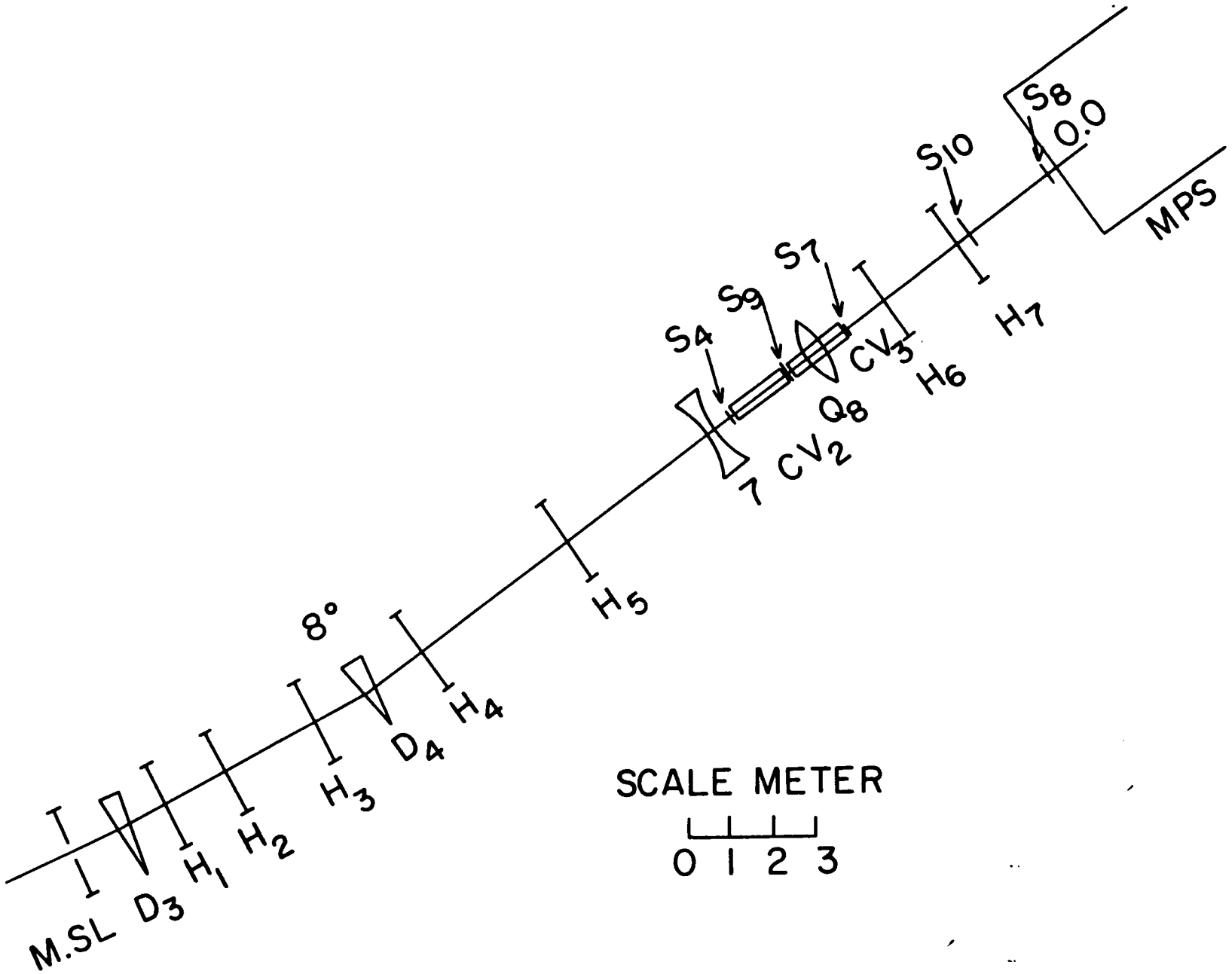
S8
0.0
S10
MPS
S7
S9
S4
CV3
H6
H7
Q8
CV2
7
H5
8°
H4
D4
H3
H2
H1
D3
M.SL
SCALE METER
0 1 2 3

y coordinate,† were used. The principal parameters of these chambers are listed in Table 3. H1 to H5 with the bending magnet D4 in-between measured the momentum, and H6 and H7 determined the position and direction of each particle as it entered the MPS magnetic field. A scintillation counter S_2 determined the time of the particle arrival while the scintillation counters S_1, S_2, S_4, S_7 with veto scintillators, S_8, S_9, and S_{10} defined the beam. The dimensions of these counters are listed in Table 4. CV_2 and CV_3 were two threshold Cerenkov counters used for selecting kaons (described later).

The momentum and the angular resolutions obtained by the incident beam spectrometer were $\Delta p/p = \pm .25\%$ and $\Delta\theta \sim \pm 1$ mrad, respectively.

b. MPS Magnet:

The main feature of the spectrometer was a large C magnet (Ref. 30) weighing 650 tons with 10 KG central field. An isometric view of the magnet is shown in Fig. 3. The magnet aperture was 457.2 cm deep by 182.9 cm wide by 121.9 cm high and had twelve 12.7 cm slots every 30.9 cm on the top pole (Fig. 3) to allow insertion of the magnetostrictive spark chambers. The magnet could be rotated $\pm 15^{\circ}$ about a pivot point $\sim$ 45 cm inside the magnet from its upstream end.

Field mapping was done at 3 excitations, namely 9.5 kA, 6 kA and 3.35 kA which produced central fields of approximately 10 kG, 7.5 kG and 5 kG respectively. Measurements were made around the periphery of and within two rectangular boxes, one enclosing most of the MPS field,

---

† Coordinate Systems: A right-hand coordinate system was used with x increasing towards the open side of the MPS magnet, y increasing vertically upwards and z increasing along the beam direction. The MPS magnet was rotated by $\sim 1^{\circ}$ with respect to the incident beam direction. The pivot point of the magnet was chosen as the origin for both the beam coordinate system and the MPS coordinate system. The field mapping system used the center of the magnet as the origin.

TABLE 3

List of Proportional Wire Chambers and Their Parameters

	BEAM P.W.C.		TRIGGER P.W.C.
Spacing between anode and cathode	.356 cm (.140")		.635 cm (.250")
Signal plane	Au coated W wires ~.018 m.m in diameter (.7 mils)		Au coated W wires ~.025 m.m in diameter (1 mil)
Spacing of signal wires	.98 m.m (26 to an inch)		~2.5 m.m (10 to an inch)
Thickness of mylar windows	~.03 m.m		
Dimension	H1-H5 20.3cmx5cm (8" x 2")	H6-H7 20.3cmx10.1cm (8" x 4")	TPx1, TPx2 182.9cmx120.7cm (72" x 47.5")
Active wires	X = 128 Y = 64	X = 192 Y = 64	480 640
Cathode plane	.01m.m thick Al foil		non-mag stainless steel wires .13 m.m (.005 in) diameter and 1.3 m.m apart (20/inch)

TABLE 4

List of Scintillation Counters and Dimensions

COUNTER	SHAPE	HEIGHT cm	WIDTH cm	THICKNESS cm	USED in
S1	rectangular	2.5	17.8	.6	coincidence
S2	"	8.9	19.7	.3	"
S4	disc	Diameter =	25.4	.3	"
S7	retangular	7.6	20.3	.3	"
S8	annulus	Ext. 10.16 Int. 5.1	20.3 7.6	.3	veto
S9	circular ring	Diameter(ext.) = 45.7 Diameter(int.) = 24.8		.6	"
S10	rectanguler annulus	Ext. 22.9 Int. 7.0	30.5 14.6	.6	"

FIG. 3 ISOMETRIC VIEW OF THE MPS MAGNET

MPS MAGNET

Weight	650 tons
Gap	6' wide x 4' high x 15' long
Central Field	10kG
Coils	14 pancakes, 11 turns ea.
Power	10,000 A @ 240V
Cooling Water	400 GPM @ 20°C rise
Downward Force at Midplane	550 tons (magnet powered)
Support	4 hydrostatic bearings, 30" dia. on steel plates
Rotation	± 15°, pivot 18" inside upstream end

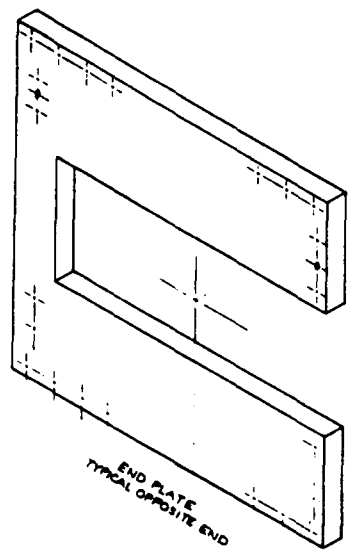

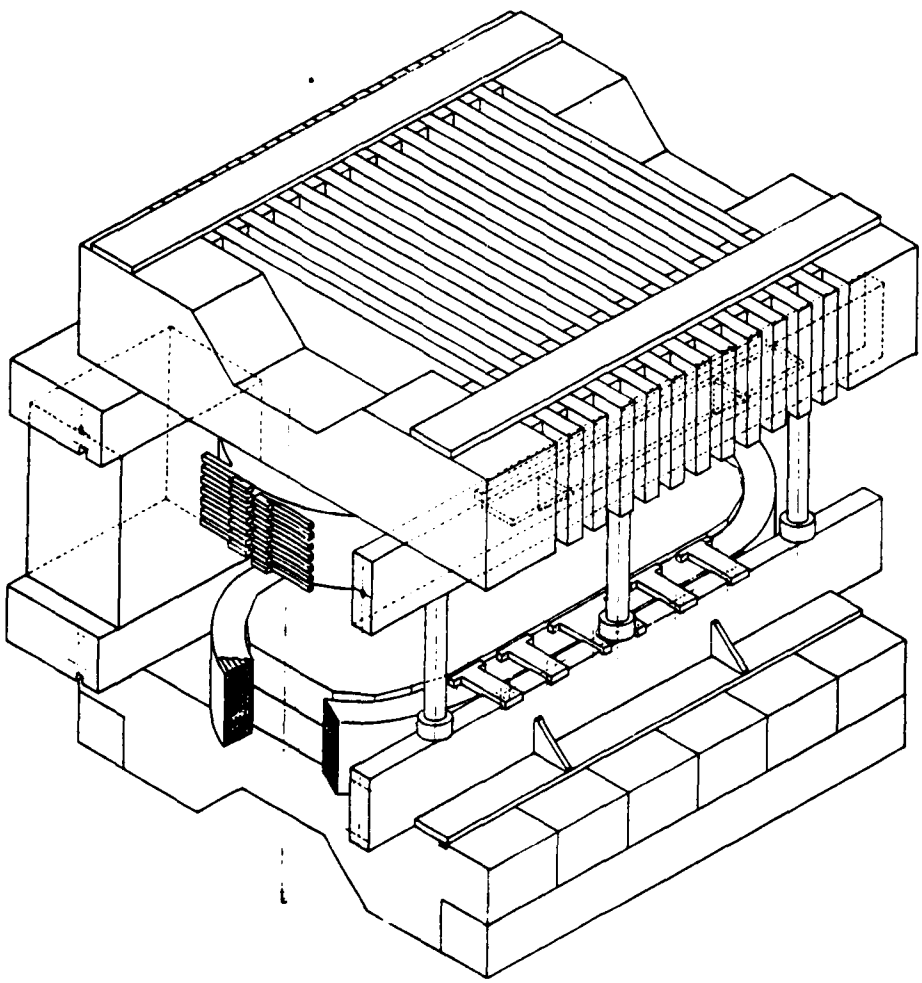

the other extending out about 90 cm between two of the support posts. B_y was measured throughout the whole box and B_x on the planes at the x limits. Each set of data contained 12 strings of measurements at a fixed x, y value for each inch in the z direction from z = -610 cm to z = 406 cm in the magnet coordinate system (x = 0 was the magnet centerline, y = 0 the medium plane and z = 0 the center of the magnet).

The measurements were fitted with series of Fourier - hyperbolic functions (solutions of the Laplace equation) with a resultant accuracy or rms deviation less than .1% in the field volumes and $\sim$ .2% in parts of the periphery near the poles.

c. Liquid Hydrogen Target:

The liquid H_2 target was enclosed in a cylindrical cell of .018 cm thick mylar 50 cm long and 7.62 cm in diameter. It was wrapped in 40 layers of 'superinsulation' (aluminized mylar) .00064 cm in thickness. The entire unit was placed in a cylindrical vacuum jacket of 2.5 cm thick PVC foam and 17.8 cm outside diameter with windows of .025 cm thick mylar at each end.

d. The Main Spectrometer:

Figure 4 shows the layout of the main spectrometer. The downstream detectors in the MPS magnet consisted of two trigger proportional wire chambers TPX1 and TPX2 (x coordinate measuring only) and seven XUVX and seven YY spark chamber modules. Magnetrostrictive readout was used for all spark chambers. Each XUVX module contained two X gaps, one U and one V (wires at $\pm 15^{\circ}$ angle to those of the X gaps) gap while the YY modules contained two Y gaps. In all cases the readout wands were located outside the magnet in the low field region.

FIG. 4 THE MAIN SPECTROMETER LAYOUT

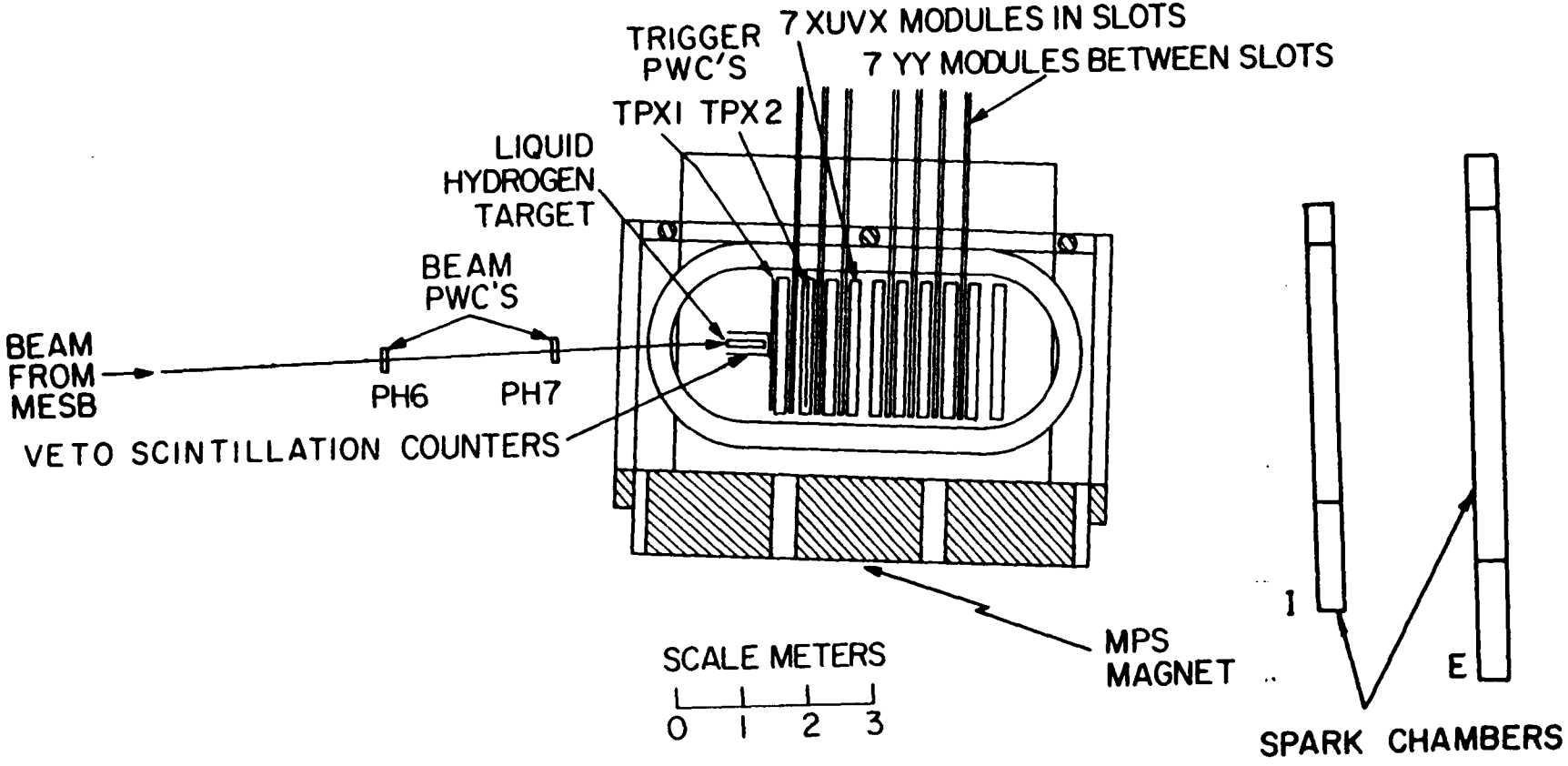
TRIGGER PWC'S
7 XUVX MODULES IN SLOTS
7 YY MODULES BETWEEN SLOTS
TPX1 TPX2
LIQUID HYDROGEN TARGET
BEAM PWC'S
BEAM FROM MESB
PH6
PH7
VETO SCINTILLATION COUNTERS
MPS MAGNET
SCALE METERS
0 1 2 3
1
E
SPARK CHAMBERS

Two modules of magnetostrictive spark chambers (I and E) each containing two X gaps, two Y gaps and 1 W gap (45° to X), were the only detectors used downstream of the MPS magnet (Fig. 4).

Four scintillation counters 96 cm (length) x 38 cm x 38 cm surrounded the vacuum jacket of the target in the form of an open-ended rectangular box. These vetoed events with charged recoil particles at wide angles. For the later part of the data taking run, the box was lined with 3 mm thick lead to provide a γ veto.

e. Detectors

i. Beam Cerenkov Counters:

CV_2 and CV_3 were two high pressure gas Cerenkov counters of the threshold type (Ref. 31). The vessels used were of iron for CV_2 and Al for CV_3 (which was placed inside the quadrupole Q_8 to conserve space along the beam line). Each radiator was $\sim$ 152.4 cm long and $\sim$ 28.58 cm in diameter. CV_2 was used for pion detection and CV_3 detected both π's and K's. Table 5 lists some important parameters of the counters.

ii. Proportional Wire Chambers (PWC's)

Sixteen multi-wire proportional chambers were used in the experimental setup, fourteen in the beam spectrometer and two in the main spectrometer. Each chamber consisted of a central signal plane at ground potential (anode) and one high voltage cathode plane on either side spaced equally apart. Mylar or Aclar was used for the windows. The parameters of these chambers are listed in Table 3. The gas circulated through these contained $\sim$ 80% Argon, $\sim$ 15-20% isobutane, $\sim$ .5-1% Freon 13B1 and $\sim$ 4-7% dimethoxymethane. The operating voltage was $\sim$ 4 kV. The signal from each wire was amplified and discriminated

TABLE 5

List of Cerenkov counters and Essential Parameters

	GAS	PRESSURE p.s.i.a.	INDEX OF REFRACTION AT 20°C	END WINDOWS	THRESHOLD β	THRESHOLD γ
CV_2	*a) Fr 12	14.7	1.00107	~.025 cm(.01") mylar	.99893	21.62
	*b) Fr 114	18.7	1.0013		.9984	17.68
CV_3	Fr 12	*a) 54.7	1.00399	~.24 cm(3/32") aluminum	.9958	10.92
		*b) 64.7	1.00472		.9950	10.01

β_π at 6 GeV/C = .99946, γ_π = 30.43

β_K at 6 GeV/C = .99665, γ_K = 12.23

* a → '75 Fall run

b → '76 Winter run

to form a standard logic pulse output. The logic pulses from each chamber were sent to a linear adder, the output pulse height of which was proportional to the number of hits in the chamber for any one event. This determined the track multiplicity at each chamber for each event. The output signal (logic pulse) from each wire was simultaneously sent to a strobe buffer circuit to record the wires which were hit.

iii. Spark Chambers

There were forty-two wire spark chambers with magnetostrictive readout (Ref. 32) placed in the MPS magnet. Two parallel planes spaced $\sim$ 1.3 cm apart with tensioned Aluminum alloy wires running in the same direction formed a sparking gap. The Al wire spacing and diameter were $\sim$ 1 mm and 125 μm respectively on each plane. Four (two) gaps were stacked together to form an XUVX(YY) module with an aclar window (50 μm thick) on either side. The gas mixture circulated in the chambers consisted of 89% Ne, 10% He, and 1% ethyl alcohol. Some operating and geometrical parameters are listed in Table 6.

The magnetostrictive readout wire stretched across the sparking wires. The magnetic field caused by the flow of the pulsed current in the sparking wire created a striction pulse (a longitudinal pressure wave, or sound pulse) in the readout wire which propagated along it with the velocity of sound. At the end of the readout wire the sound pulse generated an electrical signal in a pickup coil. The high voltage pulse itself generated an acoustic pulse on the readout wire at each end of the active area of the chamber; these were called the 'fiducials'. The first fiducial started a set of eight digitizing scalers which count a 20 MHz clock. Each real spark stopped one

TABLE 6

List of Wire Spark Chambers and Their Parameters

High voltage for sparking	M.P.S. chs 4 K.V. downst. chs ~7 K.V.	at the Chamber.		
Clearing field voltage D.C.	M.P.S. chs ~ 50 V downst. chs 150 V			
Typical dead time	~ 30 ms			
No. of different kind of gaps used inside magnet	14X	14Y	7U	7V
Wires in them	vertical	horizontal	+15° to vertical	-15° to vertical
Dimension	180 cm wide x 120 cm high			
No. of gaps downst. of the magnet	4X	4Y	2W	
	vertical	horizontal	45° to vertical	
Dimension I	290 cm x 91 cm			
E	396 cm x 122 cm			

subsequent scaler, thus giving the time of sound propagation. Since there were eight scalers associated with each plane up to eight sparks could be accommodated.

Each plane of a gap was read out separately in opposite directions for each spark and the final spark position was obtained by averaging in the computer the two readings from a chamber gap. This minimized the error in the position measurement arising from the angle the tracks make with respect to the plane normal, the non-uniformities in the magnetostrictive wand and delay due to spark formation time.

3. Triggering the System:

Figure 5 shows the diagram of the trigger logic. A good beam particle was defined as $SH\bar{A}_K$, where:

$$S = S_1 \cdot S_2 \cdot S_3 \cdot S_4 \cdot S_7$$

$$H = H_1 \cdot H_3 \cdot H_4 \cdot H_5 \cdot H_6 \cdot H_7$$

$$\bar{A} = \bar{S}_8 + \bar{S}_9 + \bar{S}_{10} + (\overline{H_{1x} \geq 2}) + (\overline{H_{6x} \geq 2}) + (\overline{H_{6y} \geq 2}) + (\overline{H_{7x} \geq 2}) + (\overline{H_{7y} \geq 2})$$

and $K = \bar{C}_2 \cdot C_3$

where A · B stands for a coincidence between A and B, and A + B stands for "OR" between A and B. Here S's stand for the signals from the corresponding scintillation counters denoted by the suffixes, H's for those of the beam PWC's (both X and Y's unless specified otherwise in the suffix), and C's for those of the Cerenkov counters (Fig. 2). Typically $(H \geq n)$, where n is an integer, stands for demanding n or more particles through the PWC. $(\overline{H \geq n})$ stands for vetoing events with n or more.

FIG. 5 SCHEMATIC DIAGRAM OF THE ESSENTIALS OF THE TRIGGER LOGIC

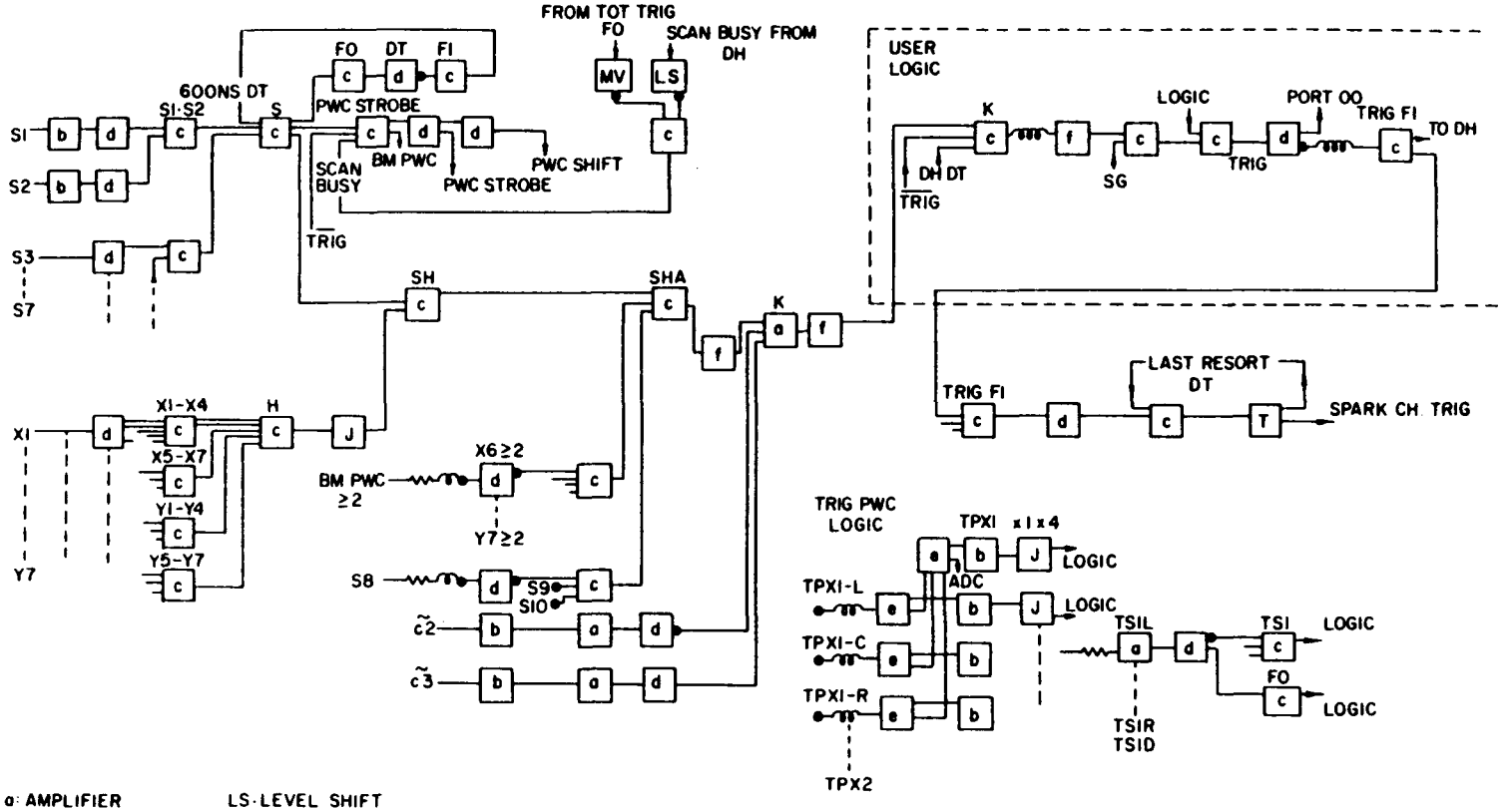

a: AMPLIFIER	LS: LEVEL SHIFT
b: LIN. F.O.	ADC: ANALOG DIGITAL CONVERTER
c: COINCIDENCE	DH: DATA HANDLER
d: DISCRIMINATOR	DT DEAD TIME
e: LIN FI-FO	FI FAN IN
f: F.O.	FO FAN OUT
T: TRANSLATOR	J JOERGER DISCRIMINATOR
MV MULTI VIBRATOR	SG SWITCH GATE

Profile Triggers: The spectrometer was triggered when a good beam particle was detected ($SH\bar{A}_K$).

Data Triggers: The data triggers required two to four charged particles going through the center part of TPX1 (TPX1C), no charged particle through either left or right side of TPX1 (TPX1L, TPX1R),† four to six charged particles through TPX2 and none through the veto-box around the target. Expressed in the trigger logic symbols it was:

$$S\cdot H\cdot\bar{A}_K(DT)\cdot(TPX1C \geq 2)\cdot(TPX2 \geq 4)\cdot\overline{(TPX1L \geq 1)}\cdot\overline{(TPX1R \geq 1)}$$
$$\cdot\overline{(TPX1C \geq 5)}\cdot\overline{(TPX2 \geq 7)}\cdot\overline{(TS1R)}\cdot\overline{(TS1L)}$$

where S H $\bar{A}_K$(DT) = $SH\bar{A}_K$ with proper dead time (DT)

TPXC, TPXL, TPXR = center, left and right region of the TPX

TS1R, TS1L = right and left side of the target veto TS1.

Figure 6 shows a typical event readout cycle timing. For every good beam particle trigger signals from all the PWC's were strobed into the buffer and held for enough time (beam trigger dead time $\sim$ 500 nsec) to determine whether the final data trigger requirement was satisfied. As soon as a data trigger arrived, the spark chambers were fired. To avoid spurious electronics signals due to spark chamber noise, the trigger signal also generated the 'Quiet gates' which disabled all the input gates to the data acquisition electronics until the spark chamber firing was over. Meanwhile, the Data Handler (DH), upon receiving a trigger, put out its own dead time for the completion of the interrogation of all active devices as part of its readout cycle. The readout cycle of the data handler is explained in the following section.

---

† In order to facilitate this trigger logic, TPX1 was divided into three zones, TPX1L, TPX1C and TPX1R.

FIG. 6 A TYPICAL EVENT CYCLE TIMING

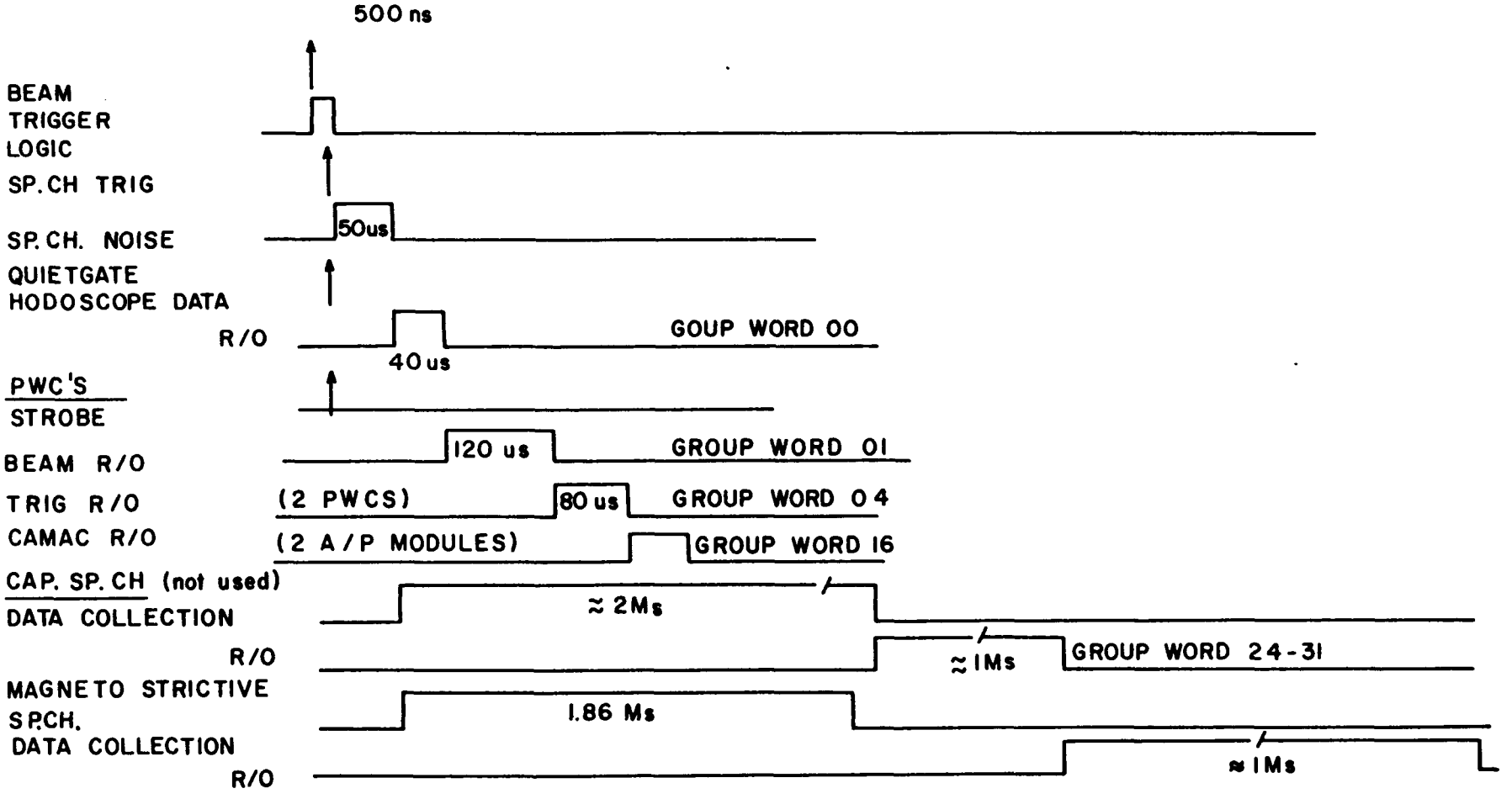
500 ns
BEAM
TRIGGER
LOGIC
SP.CH TRIG
SP.CH. NOISE
50us
QUIETGATE
HODOSCOPE DATA
R/O
GOUP WORD 00
40 us
PWC'S
STROBE
BEAM R/O
120 us
GROUP WORD 01
TRIG R/O
(2 PWCS)
80 us
GROUP WORD 04
CAMAC R/O
(2 A/P MODULES)
GROUP WORD 16
CAP. SP. CH (not used)
DATA COLLECTION
≈ 2Ms
R/O
≈ 1Ms
GROUP WORD 24-31
MAGNETO STRICTIVE
SP.CH.
DATA COLLECTION
1.86 Ms
R/O
≈ 1Ms

The total effective dead time was the inclusive OR of the 'Quiet gate', the data handler dead time and the characteristic dead time assigned to each active device (for instance 30 msec for spark chambers).

4. Data Handler:

The Data Handler consisted of the data acquisition electronics and a 16-K-bytes buffer memory of 18 bit bytes. After each trigger it collected, formatted and stored the information from all the devices into the buffer by interrogating the corresponding device controllers. After the AGS pulse the data handler transmitted the stored data to the magnetic tape unit (for recording) and a predetermined fraction of it to the PDP10 data link (for on-line analysis) simultaneously.

The data handler communicated with each device through a DEVICE PORT which could be switched in by throwing manual switches on the data handler. Table 7 shows the device port assignment of each device. The data handler interrogates the 'active device ports' sequentially. The data format is discussed later. The group numbers in general represented the address of the device controllers connected with the device port. The group words were generated by the data handler (except that the magnetostrictive device controller generated the group words from 33 to 62) to address the corresponding device controller. Upon command each controller examined the local data buffers, scalers or CAMAC unit connected to it, formatted and transmitted the data in 18-bit words to the data handler. The last group (#63) of information was generated and loaded by the data handler and contained the trigger bit and other pertinent information about the event.

TABLE 7

List of Devices Used and Their Group and Port Numbers

DEVICE	PORT #	GROUP #'s
Hodoscope (fast gates)	00	00
Beam PWC's	01	01
Trigger PWC's	02	04
CAMAC System	04	16
Capacitive Spark Chambers	06	not used
Magnetostrictive Spark Chambers	07	32 - 62

At the end of every AGS pulse (which typically contained ∿ ten events) the data handler read in the contents of a buffer containing 16 Digital Volt-Meter (DVM) readings taken immediately after the previous AGS spill and 32 high speed scaler readings. These data and settings of the thumbwheel switches on the data handler were formatted as a 'main block' and recorded as part of the stored data.

5. Data Format:

As mentioned earlier after each AGS spill which contained several events, the data handler put out a main block. Each event was contained in a sub-block.

Main Block Format: Fig. 7a shows the main block format. The data handler started generating this with a thirty-six bit byte information for every user, which consisted of information pertinent to the user, then the CAMAC scaler data and the DVM (described later) data. Following this information obtained from the thumbwheel switches on the data handler was written (e.g. momentum, MPS angle, beam type) and then the total word count of the block. Then there was a check sum word (a parity check for the generated data). The last word was an identifier word for the main block containing the block number, the sub-block number (which was zero for the main block), and the clock.

Event Record (or Sub-Block): Each event within a spill was written as a record and identified by a sub-block number. The data handler interrogated the active device ports in the order shown in Table 7. After storing the data from the device it generated a 'group-word' characteristic of the device controller as shown in

FIG. 7a DATA FORMAT OF THE MAIN BLOCK

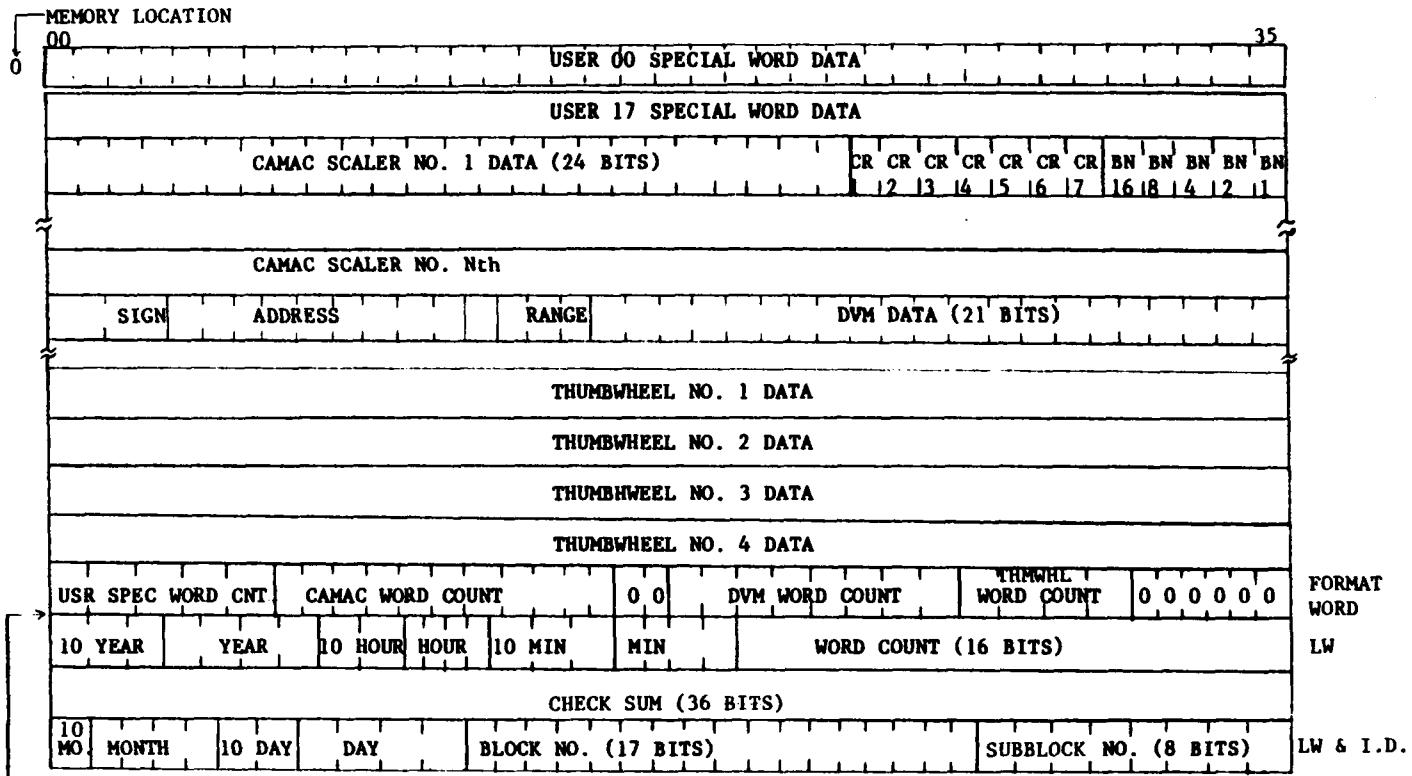

Bit 00 M.S. Bit 35 L.S.

A fill word of all "1's" will be inserted here if the words stored up to this point are an even number.

NOTE: 1. Bits 16, 17, 30-35 of the format words are set to 0, to distinguish it from the all '1's fill word.

2. Subblock No. & Block No. to be counted & Displayed by an internal scaler.

Fig. 7b. The last device interrogated was magnetostrictive spark chambers and in this case the device controller generated the corresponding group words. After accumulation of the data, group word number 63 was generated by the data handler containing information pertinent to the trigger type of each active user, the active devices, active users, total number of eighteen-bit bytes in the event and the total number of bytes in group 63. Then there was the checksum word for parity check. The last two eighteen bit bytes identifying the sub-block in Fig. 7a were generated by the data handler during transmission of the data but not stored in the data handler memory.

The data handler transmitted the data to the tape and the PDP10 in the reverse order of accumulation, i.e. the main block was written out first starting with the main block identification word. Then the last event in the spill was written out with the sub-block identification at the beginning and so on. A core image of the data handler was called a box-dump.

FIG. 7b DATA FORMAT OF THE SUB (EVENT) - BLOCK

1 EVENT

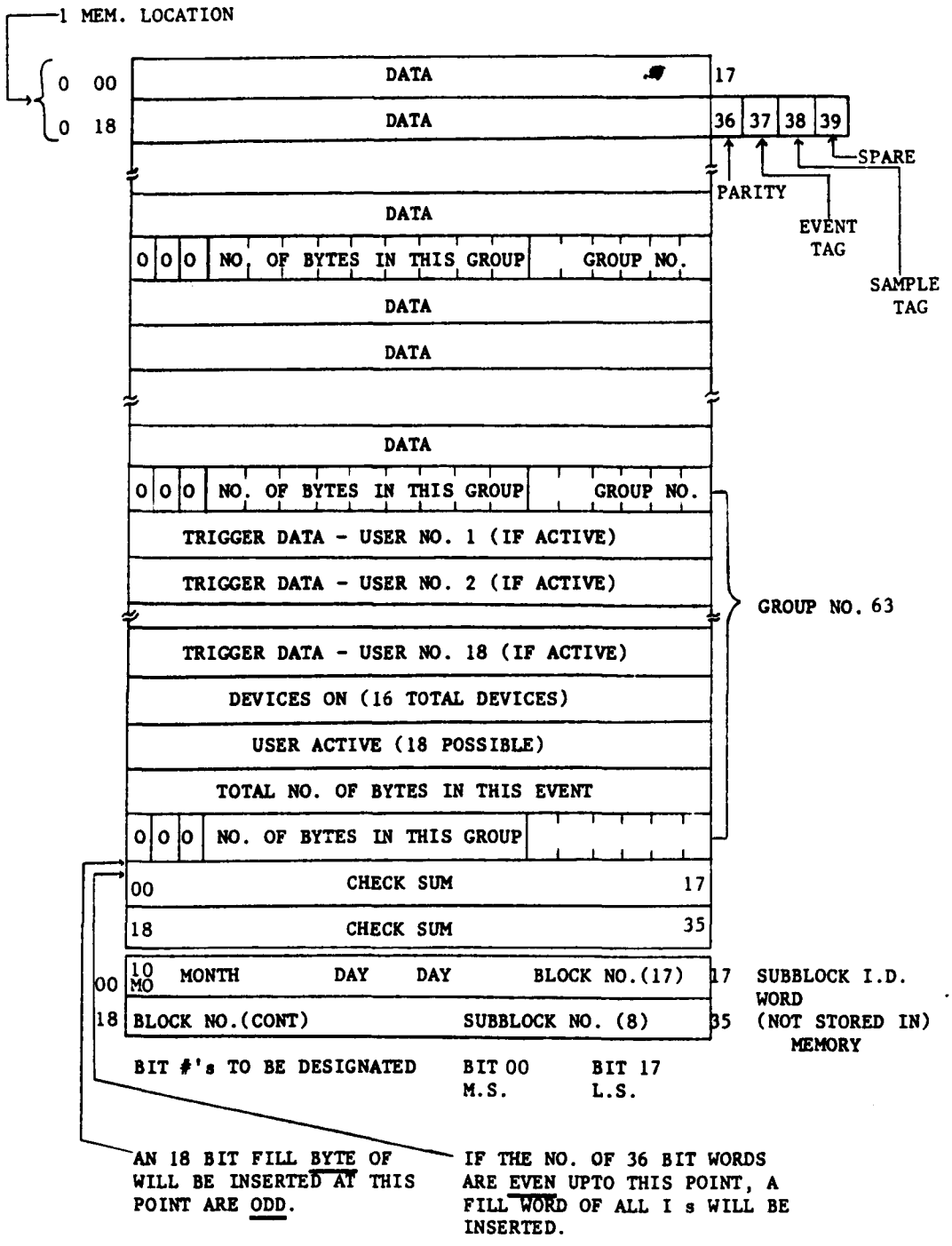
1 MEM. LOCATION
0 00
0 18
DATA
17
DATA
36
37
38
39
SPARE
PARITY
EVENT TAG
SAMPLE TAG
DATA
0 0 0 NO. OF BYTES IN THIS GROUP GROUP NO.
DATA
DATA
DATA
0 0 0 NO. OF BYTES IN THIS GROUP GROUP NO.
TRIGGER DATA - USER NO. 1 (IF ACTIVE)
TRIGGER DATA - USER NO. 2 (IF ACTIVE)
GROUP NO. 63
TRIGGER DATA - USER NO. 18 (IF ACTIVE)
DEVICES ON (16 TOTAL DEVICES)
USER ACTIVE (18 POSSIBLE)
TOTAL NO. OF BYTES IN THIS EVENT
0 0 0 NO. OF BYTES IN THIS GROUP
00 CHECK SUM 17
18 CHECK SUM 35
00 10 MO MONTH DAY DAY BLOCK NO.(17) 17
18 BLOCK NO.(CONT) SUBBLOCK NO. (8) 35
SUBBLOCK I.D. WORD (NOT STORED IN) MEMORY
BIT #'s TO BE DESIGNATED
BIT 00 M.S.
BIT 17 L.S.
AN 18 BIT FILL BYTE OF WILL BE INSERTED AT THIS POINT ARE ODD.
IF THE NO. OF 36 BIT WORDS ARE EVEN UPTO THIS POINT, A FILL WORD OF ALL I s WILL BE INSERTED.

CHAPTER III

EXPERIMENTAL PROCEDURE

1. Data Taking:

The data were recorded on magnetic tapes. A predetermined fraction but random sample of the data was simultaneously sent to the PDP10 computer of the On-Line Data Facility via a data link (connected to the data handler) for on-line analysis to monitor the experiment. The experiment was run in the fall of 1975 (September) and winter of 1976 (February-March) with a total AGS machine time of 250 hours. The data from each period consisted of 252 and 204 magnetic tapes respectively. A few percent of the magnetic tapes were for alignment runs (with liquid H_2 taken out of the target) and some special runs (efficiency determining, etc.) for various calibration purposes and monitoring the stability of the detection equipment. Each data tape contained typically $\sim$ 9000 triggers. In the normal data taking mode one to two profile triggers were accepted in every beam spill for spark chamber efficiency (one-track) monitoring, resolution determination, etc. About one quarter of the fall data was taken without the veto box around the target. In the winter run the veto box was lined with Pb to provide a γ veto.

2. Monitoring:

Continuous monitoring of the equipment and the data was essential for recording satisfactory data. The most important monitoring was the on-line analysis of part of the data which provided diagnostics

of the experiment, immediate warning of equipment malfunction, information on the performance of the detectors, and indications of the kind of physics the experiment would yield. The scaler system, the DVM system and the alarm system were also vital in monitoring and are described briefly.

a. Scaler System:

As shown in Fig. 5, there were numerous fan-outs at different stages of the fast electronics, some of which were connected to scalers to monitor the rates visually, e.g., S, SH, $SH\bar{A}$, $SH\bar{A}_K$, $SH\bar{A}_K(DT)$, TPX efficiencies, number of triggers. These counts per AGS spill were displayed on a CRT display screen by CAMAC scalers and recorded by the data handler after each AGS spill as a part of the data. Some scaler counts were accumulated throughout the run for later analysis.

b. DVM System:

The Hewlett Packard Model 2402 system with a 200 channel scanner was used, 125 of which were used in reading out the shunt currents of all the magnets, the hall (probe) currents and voltages of all the dipole magnets used in the system including the MPS magnet, spark chamber clearing fields voltage, beam separator voltages, temperature of the alcohol bath for the gas circulated through the spark chambers, analog signal for the target positions, etc. A printout of the readings was available from the DVM system on command. Successive 16 DVM readings were taken for each AGS pulse after each beam spill and treated as part of the data. Hence each channel was monitored about every eight data transmissions.

c. Alarm System:

The various gas systems were monitored by an alarm system using sensors with upper and lower critical limits. An out-of-range indication in the system sounded an audio alarm insuring immediate attention. Similar audio alarms were used to indicate PWC high voltage trip-offs or unusual temperature rise in the MPS magnet.

3. On-Line Monitoring:

The most important monitoring of the equipment was done by the on-line program in the PDP10 computer. After every AGS spill the data handler transmits the contents of its memory to the PDP10 data link which accepted the transmission only if it finished analyzing the previous one. About 10% of the total events recorded were analyzed by the on-line program. The various tasks performed by the on-line program are listed below.

a. It monitored all the DVM readings. If a particular reading changed outside its preset tolerance, a warning message was typed out on the teletype.

b. The PWC and the magnetostrictive chamber data were checked for proper readouts and fiducials. If any deviation from the expected form took place, the specific error occurrence and the chamber number was typed out on the teletype.

c. The transmitted data was checked for the correct format and in case of any error the appropriate message was typed out.

d. The on-line program displayed PWC wire maps, raw sparks, pattern recognized tracks in different views (xz, yz), useful histograms and various scatter plots on the CRT display upon users request.

e. It performed a complete analysis of the small sample of events and calculated the chamber efficiencies (for profile events only) and the effective and missing masses. The results were available as histogram-displays.

f. Statistics were accumulated through the course of each run and a complete printout (hard copy) with all the relevant information was obtained on command when one (or more) 'run' ended.

The program execution could be interrupted by the user at any time to find out any of the above information. The basic algorithms of the on-line program used were very similar to those of the off-line data processing program and are discussed later in detail.

4. A Special Program:

Beam Tuning: Beam magnet settings were calculated for certain incident momenta. Adjustments to those settings were needed to optimize the beam flux, the separation ratio, and the final focus onto the target, as well as for running at a slightly different momentum. The program calculated and displayed two-dimensional scatter plots of the incident momentum, x, y, dx/dz, dy/dz (one versus another) at various Z's to check the beam optics and to achieve the final focus by making adjustments on the magnet settings effectively. In some cases an extrapolation was necessary to achieve this (sometimes backwards through quadrupoles and dipoles where not enough detectors were present). The beam tuning program had these options of visual displays built in. Since it did not involve the downstream information,

spark chamber data were not incorporated. Therefore, using simpler track reconstruction program for beam PWC's, the program accumulated statistics at a much higher rate than the normal analysis program.

CHAPTER IV

DATA REDUCTION

1. Introduction

The data tapes were processed by the CDC 7600 computer of the Brookhaven Central Scientific Computing Facility with the off-line analysis program PAD16 developed for MPS. Events were reconstructed and the result of analysis for the selected ones were written out on summary tapes. Each data tape contained $\sim$ 9,000 triggers and yielded $\sim$ 200 events of the type

$$K^- p \rightarrow K^0_S \pi^+ \pi^- + \text{neutrals}$$
$$\qquad\qquad\quad \hookrightarrow \pi^+ \pi^-$$

The typical processing time for each tape was 800 seconds (CPU time). The data sample written on the summary tapes was further reduced by applying a wide neutron cut (discussed later) to the missing mass from $K^0_S \pi^+ \pi^-$ in the reaction above. This reduction as well as the analysis of the final data sample to yield physics output was accomplished with the summary tape analysis program HERKN.

2. Off-Line Processing Program

A flow chart of the processing program used to analyze the data tapes is shown in the block diagram in Fig. 8. The boxes represent the major steps involved in the analysis and each was accomplished by a package of subroutines.

a. Initialization:

This consisted of reading in the geometrical and alignment parameters, fiducials, chamber to scaler correspondence (for spark

FIG. 8 FLOW CHART OF THE OFF-LINE PROCESSING PROGRAM

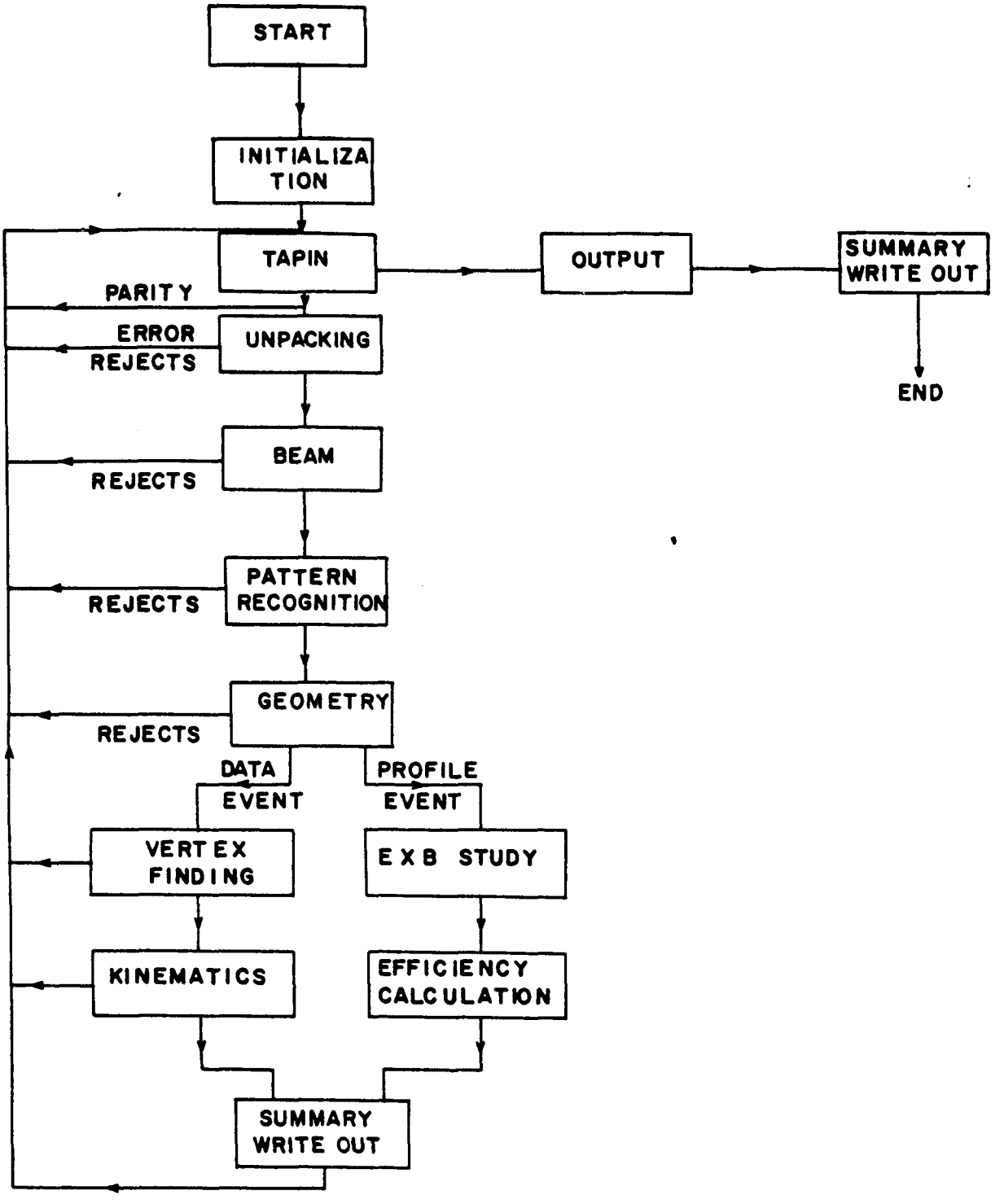
START
INITIALIZATION
TAPIN
OUTPUT
SUMMARY WRITE OUT
END
PARITY
ERROR REJECTS
UNPACKING
BEAM
REJECTS
PATTERN RECOGNITION
REJECTS
GEOMETRY
REJECTS
DATA EVENT
PROFILE EVENT
VERTEX FINDING
EXB STUDY
KINEMATICS
EFFICIENCY CALCULATION
SUMMARY WRITE OUT

chambers only) and momentum and magnetic field coefficients for the MPS magnetic field and coefficients for E x B correction (described in Chapter V). It also zeroed the arrays relevant for keeping statistics and setting up the histograms. Table 8 lists the major subroutines used and their purpose.

b. Unpacking:

The expected format of the data on magnetic tape was described earlier. Any deviation from it was considered a fault and the event was abandoned. A count of the number of occurrences of the various faults was kept and printed out on the output at the end of the tape. Table 9 shows the major subroutines for unpacking where SPARK1 was the guiding routine (Ref. 33).

i. Main Block Analysis: Each main block was unpacked by subroutine MBLK1 for year, day, hour, run number, and word count pertaining to the total number of words in the spill. In case of the first main block of a run, the thumbwheel switches were unpacked (MPS magnet current and rotation angle, target information, incident particle momentum, type of beam, etc.). DVM and scaler information were unpacked as well. In case no main block was found within the first twenty records the analysis of the tape was to be abandoned while printing out the reason of the error exit.

ii. Sub-Block (Event) Analysis: The sub-block ID word was unpacked and the block and the sub-block numbers were stored. The length of the record was unpacked and stored as well. Next a search for the Group words was made and the first byte location and the number of bytes associated with each Group word were stored. A word containing a flag for each device for which data were encountered was set up.

TABLE 8

List of Principal Subroutines and Their Purpose for 'Initialization'

Main Purpose	Subroutine Name	Called By	Purpose
Initialization	BININP	MAIN	to set up histograms
	PREAD	MAIN	to read in parameters
	WIPE	MAIN	to zero the necessary arrays

TABLE 9

List of Principal Subroutines and Their Purpose for 'Unpacking'

Main Purpose	Subroutine Name	Called From	Purpose
Guiding routine	SPARK1	MPSDAR (main)	to decode the formatted data
Unpacking the main block	MBLK1	SPARK1	to unpack the information from the thumbwheel switches
	CAMAC	MBLK1	to process the scaler data
	DVMSUM	MBLK1	to process the DVM data
Unpacking the magneto-strictive spark chamber data	MAGP	SPARK1	to record the scaler counts and number of scalers in each plane of each chamber.
	PUTWAY	MAGP	to check for repeated sparks etc. and to put away co-ordinates by plane numbers (by calling PROC)
	PROC	PUTWAY	to compute co-ordinates from scaler counts by finding the fiducials.
	FIDSMY	PROC	to set fiducials for each readout
	RAVAGE	PROC	to average the two read-outs from a spark chamber gap.
Unpacking the PWC data	PWCP	SPARK1	guiding routine, to check group words and data words.
	PUTWAY	PWCP	to check for the validity of data and to put away co-ordinates by plane number (by calling PWC)
	PWC	PUTWAY	to compute real co-ordinates from the wire numbers
Unpacking trigger information	TRIG1	SPARK1	to unpack trigger related information

This flag was checked against the combination of devices supposed to be present.

Magnetostrictive Chamber Data: As shown in Table 9, subroutine MAGP was called to unpack the magnetostrictive chamber data (if present as indicated by the flag). Once the scaler counts for each plane were unpacked by MAGP they were stored with the corresponding plane number by subroutine PUTWAY. Coordinates were computed by subroutine PROC (which monitored the fiducial statistics by calling subroutine FIDSMY). The final spark position was obtained by averaging the readings of each spark from the two planes in a spark chamber (in subroutine RAVAGE).

Proportional Wire Chamber Data: If the PWC groups contained data they were unpacked by subroutine PWCP. Again subroutine PUTWAY stored the plane number, number of signals from the plane and the wire numbers. Coordinates in cm were computed from wire numbers by subroutine PWC.

Trigger Type Determination: Once the data from the detectors were unpacked the trigger type information was examined in subroutine TRIGI. For a regular data run each event was associated with one or more trigger bits indicating the trigger category of the event. The absence of a trigger bit was considered a fatal error and the event was abandoned.

Checks were built into the unpacking process at every step to guard against faulty data or equipment malfunction. In each case of error occurrence (fatal or non-fatal) an error message and the number of times it occurred were printed out in the final output.

c. Beam:

After unpacking an event the momentum and the trajectory of the incident particle were determined by this program package. Table 10 lists the major subroutines in 'BEAM' and their purposes.

Working Principle: A single incident particle hit in each of the four x chambers, H_{1x}, H_{3x}, H_{4x}, H_{5x} (H_2 was not operational) and in both x and y of H_6 and H_7 was required. Otherwise the event was rejected. The xz component of the incident momentum was calculated as:

$$P_{xz} = CM \times DVMV/(SIN5-SIN3)$$

where DVMV ≡ D4 shunt current reading;

CM ≡ normalization constant;

SIN5 ≡ sine of the xz projection of the angle of the particle emergent from D4;

SIN3 ≡ sine of the xz projection of the angle of the particle incident at D4.

The sine of the angles were calculated as:

$$SIN3 = SLP3/(1 + SLP3^2)^{1/2}$$

and $$SIN5 = SLP5/(1 + SLP5^2)^{1/2}$$

where SLP3 and SLP5 signified dx/dz, the corresponding slope in xz. The slopes were calculated using the information from the four PWC's around D4 taking the nominal bend angle of 8° into account. The xz component of the momentum was calculated. A straight line fit was done in the yz view between H_1 and H_5. This required a minimum of two single hits in H_{1y} through H_{5y}. The incident momentum was then calculated. As shown in Table 10 subroutine BEAM was the guiding routine.

TABLE 10

List of Principal Subroutines and Their Purpose in 'BEAM'"

Subroutine Name	Called From	Purpose
BEAM	WHERE*	guiding routine, to calculate momentum, position and direction of the incident particle
MPROT	BEAM	to rotate the co-ordinate system of the beam into that of the MPS
PROJ	BEAM	to project the track given a slope and a point on the track

*called from the Main Program to decide the flow of the program according to the user logic.

Information from H_6 and H_7 was used to determine the position and the direction of the track (dx/dz, dy/dz) before entering the MPS magnetic field. The track was extrapolated to the center of the target (or to any z inside the magnet) by using subroutines PTHMPS and FIZ. These two subroutines were part of the utility program package. The extrapolation procedure is described below.

Extrapolation: The extrapolation was done in two steps. For each beam particle, PTHMPS calculated the 'deviations' from a projected straight line trajectory and their 'derivatives' at five reference planes by using the momentum coefficients.† The momentum, charge, the x-position, the y-position, dx/dz and dy/dz of the particle at the z of the entrance of the MPS magnetic field were the input information to PTHMPS. The second step was to calculate the position (s and y) and the slope of the particle at any given z between the reference planes. This was performed by method of interpolation by subroutine FIZ using the values of the 'deviations' and their 'derivatives' on the reference plane closest to the given z.

d. Pattern Recognition:

The pattern recognition part of the program consisted of two packages, 'CAB' and 'TPX12'. 'CAB' (Ref. 34) dealt with tracks long enough to go through at least two YY modules and 'TPX12' (Ref. 35)

---

† NOTE: The magnetic field measurements were used to compute all the relevant trajectories through the magnet. Then these trajectories were used to generate the product of momentum and the angular (or linear) deviation ($P\Delta\theta$ or $P\Delta\chi$) as a function of the experimental observables, e.g. position and slopes. This function was then expressed as a set of orthogonal Tchebycheff polynomials in each observable. The coefficients of these polynomials were the momentum coefficients.

with shorter tracks which extended only from TPX1 to TPX2. There were one YY(4S) and one XUVX(3S) module between these trigger PWC's.

i. CAB:

Since the y projections of the tracks were very close to straight lines, a pattern of sparks forming a straight line was looked for in the y view by subroutine YTRACK starting at the downstream end. A track was initiated if sparks were found in both the y chambers of a module and in at least one of the two y chambers in the module immediately upstream. Then the track was projected further upstream and more sparks from successive chambers were associated with the track. The track parameters (e.g., slope) were updated as the track was extended. The particular track-following attempt was abandoned if no spark was found on the track in three y chambers in a row. Attempts were made to initialize a new track moving upstream until only two YY modules were left. Any three sparks on any three of the first four chambers could initiate a track. Subroutine LINK then attempted to join the non-overlapping segments found. Up to nine Y tracks could be accommodated.

Then starting at the downstream end the u and v sparks belonging to each y track were picked up and the track projected on the two x chambers in every module. This was done by cycling through all the u and v sparks and saving the track pieces module by module (when an XUVX combination was found to be consistent with the y's) in subroutine XTRACK.

Subroutine XLINK then linked those XUVX pieces which formed part of a circle in the xz plane. If all the track segments did not lie on a smooth circle, up to three different levels of fitting were

tried in succession. In the first level if only one spark (or two if adjacent ones) of all the segments did not lie on a circle the spark was rejected and the track fitting considered successful. In case of failure, the second level tried was to split the track in two halves to see if either half formed part of a circle independently. If this attempt failed the third stage was tried. This consisted of checking if the x sparks from any two modules (starting at the downstream end) lay on a circle. When successful other sparks were checked and added to the track if consistent with the circle. XLINK was unsuccessful if none of these three stages succeeded.

If a track segment was found in two adjacent modules, a circle fit was tried by subroutine XMED to pick up x sparks in the two adjacent modules, one upstream and one downstream of these two. If a track segment was found in only one x module subroutine XSHORT tried a linear extrapolation to find x sparks on the two adjacent modules.

In case of success of XLINK, XMED or XSHORT, subroutine XTEND tried to extend the x tracks into the modules which only had u, v sparks and no x sparks. Finally a more sophisticated y track extension was done by subroutine YXTEND using an arc sine projection of a helix from the x tracks found and the track parameters (e.g., pitch, radius and center of curvature in the xz plane) were calculated.

ii. FILPWC:

Once the pattern recognition routines ('CAB') reconstructed the tracks through the spark chambers, subroutine FILPWC tried to sort out the signals on the TPX's that corresponded to the tracks. A circular extrapolation of the tracks in the xz plane was used. If any of the signals on either of the TPX's lay within the tolerance of

the tracks (1.0 cm) the signals were tagged. In case of multiple signals within the tolerance the one closest to the track was chosen.

iii. TPX12:

For each cluster in TPX1 not already assigned to a track, a track fitting attempt was tried with each cluster in TPX2. It consisted of a circle fit in x vs. z in TPX1, TPX2, 3SX12 and 3SX34.† Both of the spark chambers had to have sparks within the tolerance of the circle otherwise a new combination of sparks was tried until all the sparks were exhausted. When a circle fit was found ($\sigma \leq .6$ cm) a straight line fit in y vs. arc length s in the sparks in at least three chambers out of 4SY12, 4SY34, 3SU12 and 3SV12 was searched for. If a track in this view corresponded to the one in xz view the spark combination was set aside to be tagged later (after all the combinations corresponding to all the signals in TPX1 were tried and the best ones kept). In case of an exceptionally good fit ($\sigma \leq .15$ cm) the sparks were tagged at this point and the track saved. Two tracks could not have more than one spark in common either in the xz or in the ys view. TPX12 could accommodate up to 9-N tracks where N (≤ 9) was the number of tracks found by 'CAB'. In case an additional track was found the one with the worst chi-squared among the tracks found by 'TPX12' was replaced. At this point the fitted track information was transferred to the arrays of 'CAB' and XTEND and YXTEND were used to search for the extension of the tracks downstream of TPX1.

---

† 3SX12 and 3SX34 were the two x measuring spark chambers between TPX1 and TPX2.

e. Geometry:

Geometry found the best values of the track parameters by the least squared fit method (Ref. 36). The parameters describing the track were evaluated at the upstream end of the track. They were the x and the y coordinates (x_o, y_o), the azimuth (ϕ_o), the dip or the pitch of the helix (s_o) and the curvature of the track (c_o). This was done in three stages.

Stage 1: Approximation to a circular helix:

Subroutine RADIUS used the beginning, middle and end sparks of the track in xz and yz projection to construct a circular helix in three dimensions. Then it calculated the preliminary values of the parameters mentioned above and the arc distances between the three points.

Stage 2: Integrated orbit through the three points:

These parameters were used by subroutine INIT to swim the orbit through the three points successively. The actual swimming was done by subroutine XTRAPT which will be discussed later. The parameters of the orbit were adjusted so as to force the integrated orbit to go through the beginning, the middle and the end sparks. The swimming procedure was then integrated to make up for the local non-uniformities of the magnetic field over the integrated path.

Stage 3: Least squared fit:

A least-squared fit was done to find the best values of the track parameters thus obtained. This was controlled by subroutine SPFIT and done in subroutine AUX which was called at three levels of the fit:

i. To initialize the least squared fit;

ii. To swim the track from each data point (spark) on the track to the one immediately downstream by XTRAPT and calculate the deviations and their derivatives with respect to the parameters;

iii. To solve the least squared fit equations.

The technique used for ii) and iii) are explained in the Appendix.

f. Vertex Finding and Fitting:

Once the tracks were reconstructed, two prong neutral Vee vertices and then production vertices were searched for. Up to a maximum of ten vertices could be accommodated.

The controlling subroutine was VERTEX. Tracks belonging to K_s^o or Λ^o type decay vertices were searched for (in VERTXD) by cycling through all possible combinations of two oppositely charged tracks. Two such tracks were considered to be intersecting if the closest distance of approach between them (in APROCH) was less than 2 cm.

When two tracks intersected subroutine VERFIT calculated the vertex position by minimizing

$$\chi^2 = \sum_i \frac{d_i^2}{\sigma_i^2}$$

where d_i = distance from the fitted vertex point to a tangent to the orbit at the intersection point and

σ_i = error in track position along the distance normal,

calculated by projecting the errors in the orbit parameters back to the intersection point. χ^2 was minimized in a fashion similar to that of the track orbit fitting, yielding vertex coordinates and their errors and correlations. In the case of a two-prong vertex, the

vertex point lay on the line of closest approach of the two tracks. A chi-squared of less than 25 for the fit was considered as an acceptable vertex. Next the vertex position was checked to be within the decay fiducial volume (in VERTXD), the upstream end of which was two standard deviations upstream of the upstream end of the target and the downstream end was 2 cm downstream of TPX2. In case two tracks intersected more than once within the fiducial volume the one with the smaller separation was accepted.

The effective masses of the neutral decay vertices were then calculated in subroutine MASCK. The mass limits for a decay vertex to be accepted as a K^o ($\bar{K}^o$) or a Λ^o ($\bar{\Lambda}^o$) are described in Table 12. In case one track was common to two or more decay vertices ('tree') with acceptable effective masses, the one with the effective mass nearest to the standard $\bar{K}^o$ mass was chosen. The tracks forming the 'good' decay vertices were flagged and the effective masses saved.

A search for the production vertex was now made (in subroutine VERTXB) amongst the tracks that were not flagged as belonging to the decay vertices. Since a production vertex consisted of the intersection of the beam track with one or more different tracks APROCH was now used to find how many 'intersected' with the beam track by finding the closest distance of approach of each track with the beam track as before. Tracks intersecting with the beam track within five standard deviations of their average intersection point in z were accepted to have originated from the same production vertex. The error in x or y was negligible compared to that in z ($\leq$ 10%).

Once the number of tracks belonging to the production vertex was found, subroutine VERFIT fitted the vertex point and calculated the χ^2.

In case of an unacceptable χ^2 (> 25) repeated attempts to fit the production vertex were made with VERFIT by excluding at each step the track with the largest deviation from the fitted vertex point.

g. Summary Tape Writing: HTROUTINES:

Once the momentum of each track and the vertices were determined the effective and missing masses at the vertices were calculated assuming all the tracks as pion tracks. A typical yield of about 200 events per data tape was obtained for the reaction:

$$K^- + p \rightarrow K^0_s \pi^+ \pi^- + \text{neutrals}$$
$$\hookrightarrow \pi^+ \pi^-$$

The cuts corresponding to the $\bar{K}^0$ mass and the missing mass squared are discussed in detail in Chapter V.

A summary of each profile event and each event with at least one K^0_s type decay vertex accompanied by two-prong production vertex was written out on the summary tape (H-tapes) by the 'HTROUTINES' package. The summary consisted of the pattern recognition, geometry and vertex finding output and some special records from each tape. The special records contained the scaler readings, calculated efficiencies of the chambers, parameter values, information from the thumbwheel switches, DVM readings, PWC profiles and event statistics. The special records were written out at the end of processing each data tape.

Because of the large number of data tapes a further reduction of the volume was done by selecting the desired kind of events (and writing them out) to yield the physics results. Both reading and writing of the summary tapes were accomplished by 'HTROUTINES' which was also used as part of the kinematic program for analysis of the data summary.

3. Summary Tape Processing Program

a. Overview:

As mentioned earlier the final selection as well as the kinematic analysis of the data were done by the kinematic program. The program packages it consisted of are described below:

i. HARD6: Contained the main analysis program and is described in detail later.

ii. HUTIL: Utility package containing Input/Output (I/O) and histogramming routines.

iii. HTROUTINES: Performed packing/unpacking of the events before/after writing out/reading each record in the buffer. This included both the event and the special records.

iv. HETYAW: Dealt with outputting the special records, using the same routines as that of the processing program.

v. DVMPAK: Used processing program routines for DVM printout from the special records.

In addition, packages 'CHARM' and 'KIOWA' were used when two-dimensional (scatter) plots were wanted.

b. Main Processing Program Package:

HARD6: Table 11 lists by category the subroutines used in 'HARD6' beside the main program.

The MAIN program controlled the I/O and the overall logic of the whole program. It initialized histograms, zeroed necessary arrays to keep counts including the number of files (typically after each run there was an EOF [end of file] to be processed), number of files already processed and number of files (if any) to be skipped. Events were read in while checking against repeated events (by keeping track

TABLE 11

List of Principal Routines and Their Purpose
in the Summary Tape Processing Program

Main Purpose & Category	Subroutine Name	Called From	Purpose
Main Program	MAIN		to initialize and also the guiding routine.
Category a)	STAT	MAIN	to keep statistics of events and the EOF's.
General usage routines	SIVKIN	Kinematic routines e.g. KIN24	to calculate Kinematic variables in a reaction.
	USET	"	to set up mass and momentum for SIVKIN.
Category b)	TRSTAT	MAIN	to check the trigger type and then direct the flow of the program accordingly.
Experiment dependent routines	KIN24	TRSTAT	to perform kinematic analysis for the data triggers.
Category c)	ADK	KIN24	to control calculation of $\cos\theta$ and Φ in the Gottfried-Jackson frame of the $\bar{K}^{o}PI\ PI^{+}$ decay normal.
Gottfried-Jackson Co-ordinate transformation	LRNTZ	ADK	to perform Lorentz transformation
	ROMAT	ADK	to determine rotation matrix between two three dimensional vectors.
	ROT	ADK	to rotate one vector into another set of co-ordinates given the rotation matrix.
Category d) fiducial volume determination	ARCLEN	KIN24	to determine the track length up to a given Z.

of the block number and the sub-block number), special records were written out if asked for, and after the desired number of files were processed, final printout was obtained. Some of this was accomplished by calling various subroutines as indicated in Table 11 for those belonging to this package.

i. Category a: Subroutine STAT was called from MAIN with two different flags, one for keeping count of the EOF's and the other for keeping statistics of the events. Special records were skipped. The kinematic variables such as the invariant effective mass (of $K^o_s\pi^-\pi^+$ from reaction 1), missing mass, total energy in the center of mass, four-momentum transfer, x, y, z component of the momenta of the effective mass and the missing mass were calculated in subroutine SIVKIN. A maximum of four prongs could be reconstructed. The mass and the momentum of each prong was set up before SIVKIN was called. Subroutine USET was called for each prong to set up the momentum array for SIVKIN.

ii. Category b: This consisted of the experiment dependent routines. Subroutine TRSTAT was called by MAIN for the event records. The trigger bits were checked and the appropriate kinematic routine was called accordingly. The only such routine used for this experiment was KIN24 which analyzed the data triggers.

KIN24: Analysis as well as selection of the data events were accomplished in KIN24. For each event a 'good' production vertex was required. This consisted of two oppositely charged prongs and a beam track. Then each of the decay vertices was reconstructed after checking out the charge and the track number of both prongs. The effective mass of the decay vertex was calculated and if within the acceptable range for a $\bar{K}^o$, the effective mass and the square of the

missing mass corresponding to all four prongs ($K_s^o\pi^+\pi^-$) at the production vertex were calculated. If the square of the missing mass lay within the tolerance of that of a neutron as shown in Tables 13 and 14, the event was written out (if the program was used for the purpose of selecting the events) or the decay vertex tagged (if the program was used for analysis only). The cuts used for selection and analysis are shown in Table 13 and Table 14 respectively. These are discussed in detail in Chapter V in the discussion of the data. In addition, the decay vertex was required to be downstream of the production vertex in z for selection (2 standard deviations downstream for kinematic) purpose. The rest of KIN24 was used for analysis only. A major part consisted of the reduction of the background under the signal and is described in Chapter V.

Kinematic Cuts: $K_s^o\pi^-$ and $\pi^+\pi^-$ (at production vertex) effective mass spectra were investigated for intermediate $K^*(890)$ and ρ production. Cuts were made accordingly to investigate different intermediate channels and are discussed in the next chapter.

iii. Category c: This contained a set of subroutines to determine the angular distributions in the Gottfried-Jackson frame of the $K_s^o\pi^+\pi^-$ system. Subroutine ADK determined the normal to the $K_s^o\pi^+\pi^-$ plane and calculated the corresponding cos θ and ϕ (where θ and ϕ are the polar and the azimuthal angle of the normal respectively) in the rest frame of the resonance produced ($\bar{K}^{*o} \rightarrow \bar{K}^o\pi^+\pi^-$) for each event.† Subroutine LRNTZ was used to perform Lorentz transformation of a

---

† In case of a three-body decay, the normal to the decay plane containing the momenta of the three particles (in the Gottfried-Jackson frame) shows the equivalent angular distribution of either of the particles in a two-body decay (Ref. 37).

vector by a boost in the z-direction. Subroutine ROMAT calculated the transformation matrix between two three-dimensional vectors. Subroutine ROT used the transformation matrix to transform a vector to the desired coordinate system.

iv. Category d: Subroutine ARCLEN was used to make a fiducial volume cut by the track-length. It used the pattern recognition parameters to get the projection of the track on the xz plane. This was approximated to a circle and the intersection of this with the desired chamber was determined.

CHAPTER V

DISCUSSION OF THE DATA AND RESULTS

1. Discussion of the Summary Tape Selections

a. Selection of the Final H-Tape Event Sample:

The processing program calculated the effective masses at the decay and the production vertices. The decay vertices were flagged according to their effective masses. Once a decay vertex was flagged under a particular category (in the order shown in Table 12), further attempt at identifying it under any other category was abandoned. Events with one production vertex and at least one decay vertex of the K_s^o type were written on the primary H-tapes by the processing program.

The data sample contained in the primary H-tapes was further reduced by the summary tape processing program. Events satisfying all of the following conditions were written on the final H-tapes:

i. Contained a two-prong production vertex with an intersecting beam track;

ii. Had at least one neutral decay vertex with a K_s^o mass (assuming the tracks to be due to π^+ and π^-); and

iii. The square of the missing mass recoiling from the $K_s^o\pi^-\pi^+$ was between .36 and 1.44 GeV^2 (assuming the two charged tracks at the production vertex to be pions). This was sufficiently wide to include all events of the type $K^-p \rightarrow K_s^o\pi^-\pi^+ + n$.

Table 13 lists the total number of events on the final H-tapes from the fall and the winter data runs.

TABLE 12

Calculation of the Effective Mass at the Decay Vertex

Attribution of Mass of the track according to the charge of the track		Effective mass range in GeV	Neutral V flag
π	π	.475 - .525	K_s^o
P	π	1.11 - 1.122	Λ
π	$\bar{P}$	1.11 - 1.122	$\bar{\Lambda}$

TABLE 13

Event sample on final H-tape
(before fiducial volume cut)

Cuts applied	Range	Number of events selected Fall	Winter
$K_s^o \bar{\pi} \pi^+$ missing mass squared	.36 - 1.44 Gev^2	~ 44,000	~26,000
K_s^o effective mass	.475 - .525 GeV		

b. Background Reduction

i. Background under the neutron spectrum: Figures 9a and 9b show the missing mass square spectrum for the events written on the final H-tapes. Figures 10a and 10b show the same for the events that survived cuts ii, iii, iv, and v, listed in Table 14. The cuts are described below. Comparison of Figs. 9 and 10 clearly show that these cuts reduce the background under the neutron peak. The fractions of the event sample lost by the individual cuts or by various combinations of them are listed in Table 15.†

1. K^o_s-Λ overlap: the positively charged particle was assumed to be a proton and if the effective mass at the decay vertex fell within a Λ-mass the event was discarded.

2. Forward recoil proton: the positive track from the production vertex was assumed to be due to a proton (instead of a pion) corresponding to the reactions

$$K^- p \rightarrow \bar{K}^o \pi^- p$$
$$\rightarrow \bar{K}^o \pi^- \pi^o p$$

and events for which the square of the missing mass of $K^o_s \pi^- p$ fell in the range of -.01 to .09 GeV^2, were eliminated.

3. Four-prong production vertex events: the production vertex was relatively poorly determined compared to the decay vertex. As a result, there was some confusion of prompt 4-prong production with that of the decaying neutral Vee plus two-prong events. For small

---

† A fiducial volume cut (namely, each of the four charged tracks from the event reached at least as far downstream as $\sim$ 145 cm from the center of the target,-location of the second x measuring spark chamber downstream of TPX2) was imposed in all the analysis from here on.

FIG. 9a SQUARE OF THE MISSING MASS SPECTRUM RECOILING FROM $K^{o}_{s}\,\pi^{-}\pi^{+}$; FALL DATA, FROM FINAL H-TAPE

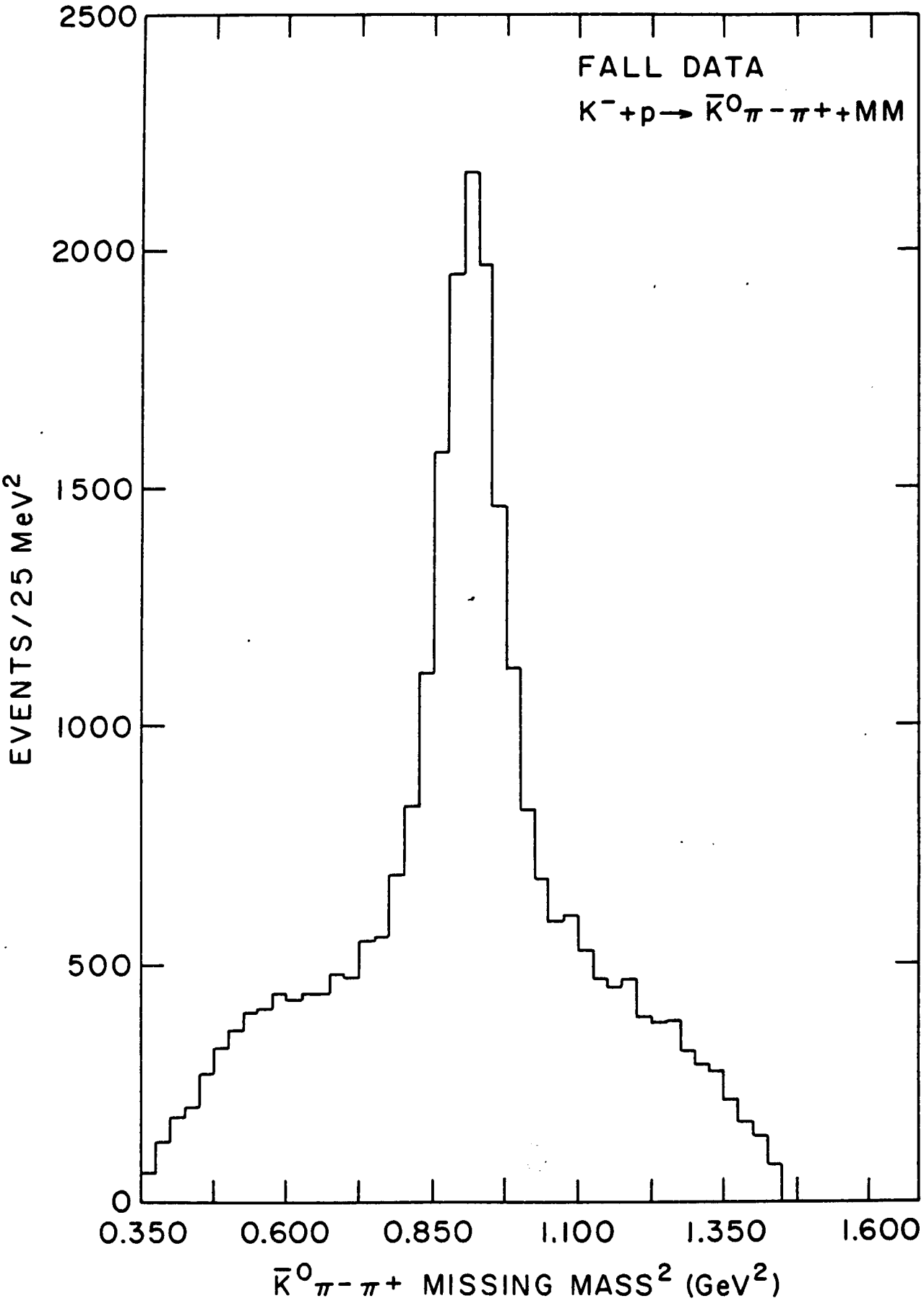
FALL DATA
$K^- + p \rightarrow \bar{K}^0 \pi^- \pi^+ + MM$
EVENTS/25 MeV^2
2500
2000
1500
1000
500
0
0.350
0.600
0.850
1.100
1.350
1.600
$\bar{K}^0 \pi^- \pi^+$ MISSING MASS^2 (GeV^2)

FIG. 9b SQUARE OF THE MISSING MASS SPECTRUM, RECOILING FROM $K^{o}_{s}\,\pi^{-}\pi^{+}$; WINTER DATA, FROM FINAL H-TAPE

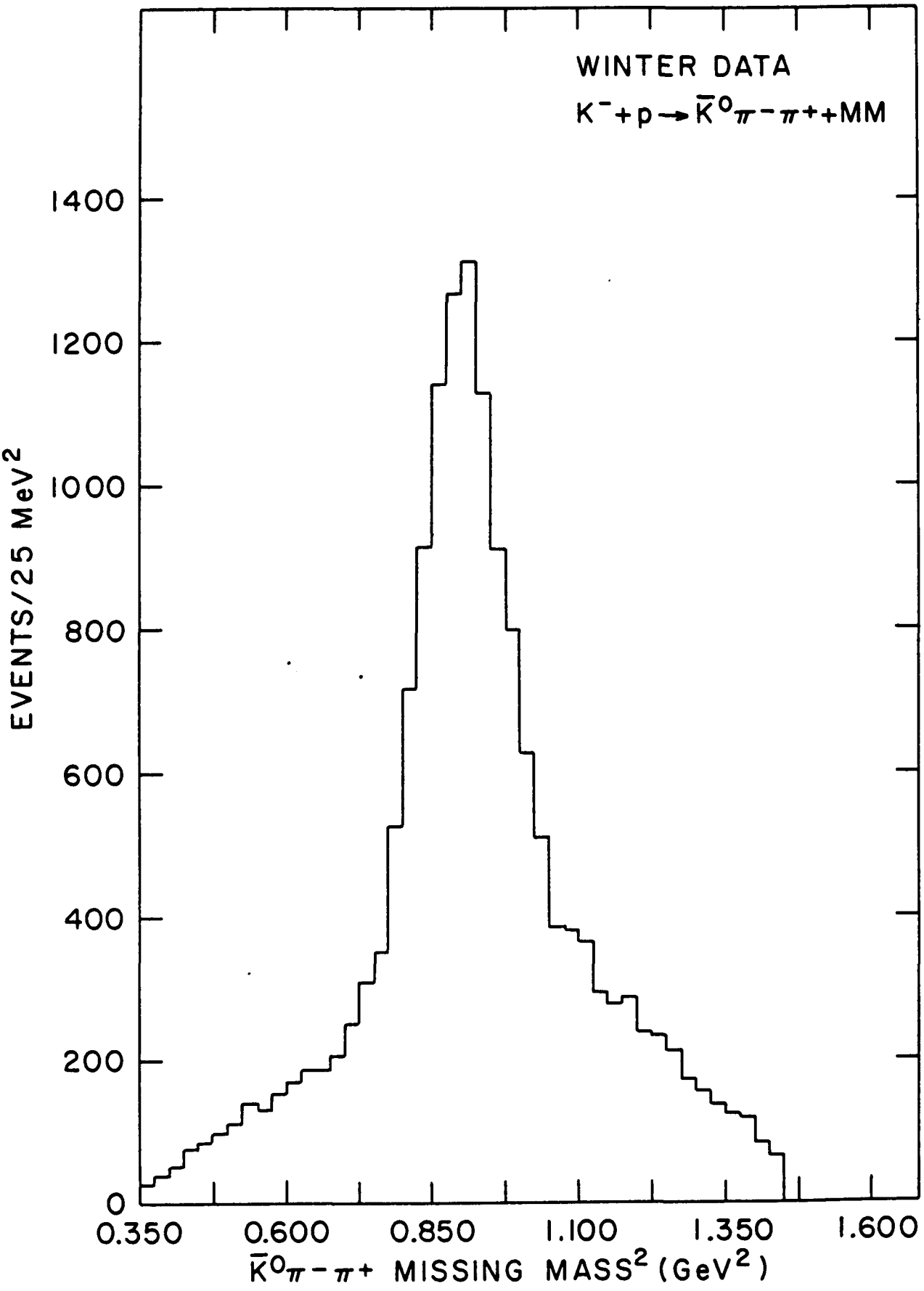
WINTER DATA
$K^- + p \rightarrow \bar{K}^0 \pi^- \pi^+ + MM$
EVENTS/25 MeV^2
0
200
400
600
800
1000
1200
1400
0.350
0.600
0.850
1.100
1.350
1.600
$\bar{K}^0 \pi^- \pi^+$ MISSING MASS^2 (GeV^2)

FIG. 10a SQUARE OF THE MISSING MASS SPECTRUM RECOILING FROM $K_s^o \pi^- \pi^+$; FALL DATA, AFTER KINEMATIC CUTS ii, iii, iv and v IN TABLE 14

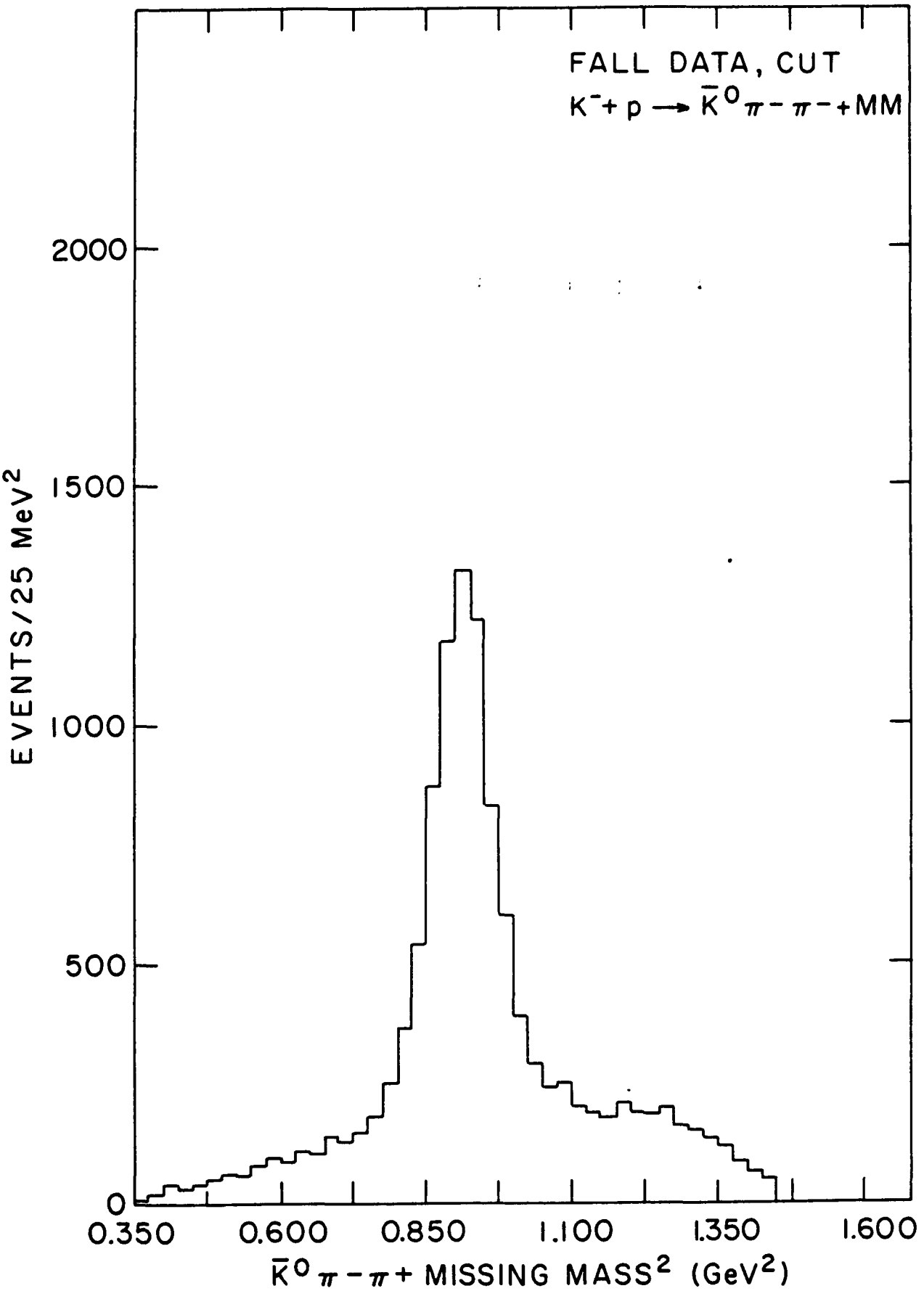
FALL DATA, CUT
$K^- + p \rightarrow \bar{K}^0 \pi^- \pi^- + MM$
2000
1500
1000
500
0
EVENTS/25 MeV^2
0.350
0.600
0.850
1.100
1.350
1.600
$\bar{K}^0 \pi^- \pi^+$ MISSING MASS^2 (GeV^2)

FIG. 10b SQUARE OF THE MISSING MASS SPECTRUM RECOILING FROM $K_s^o \pi^- \pi^+$; WINTER DATA, AFTER KINEMATIC CUTS ii, iii, iv and v IN TABLE 14

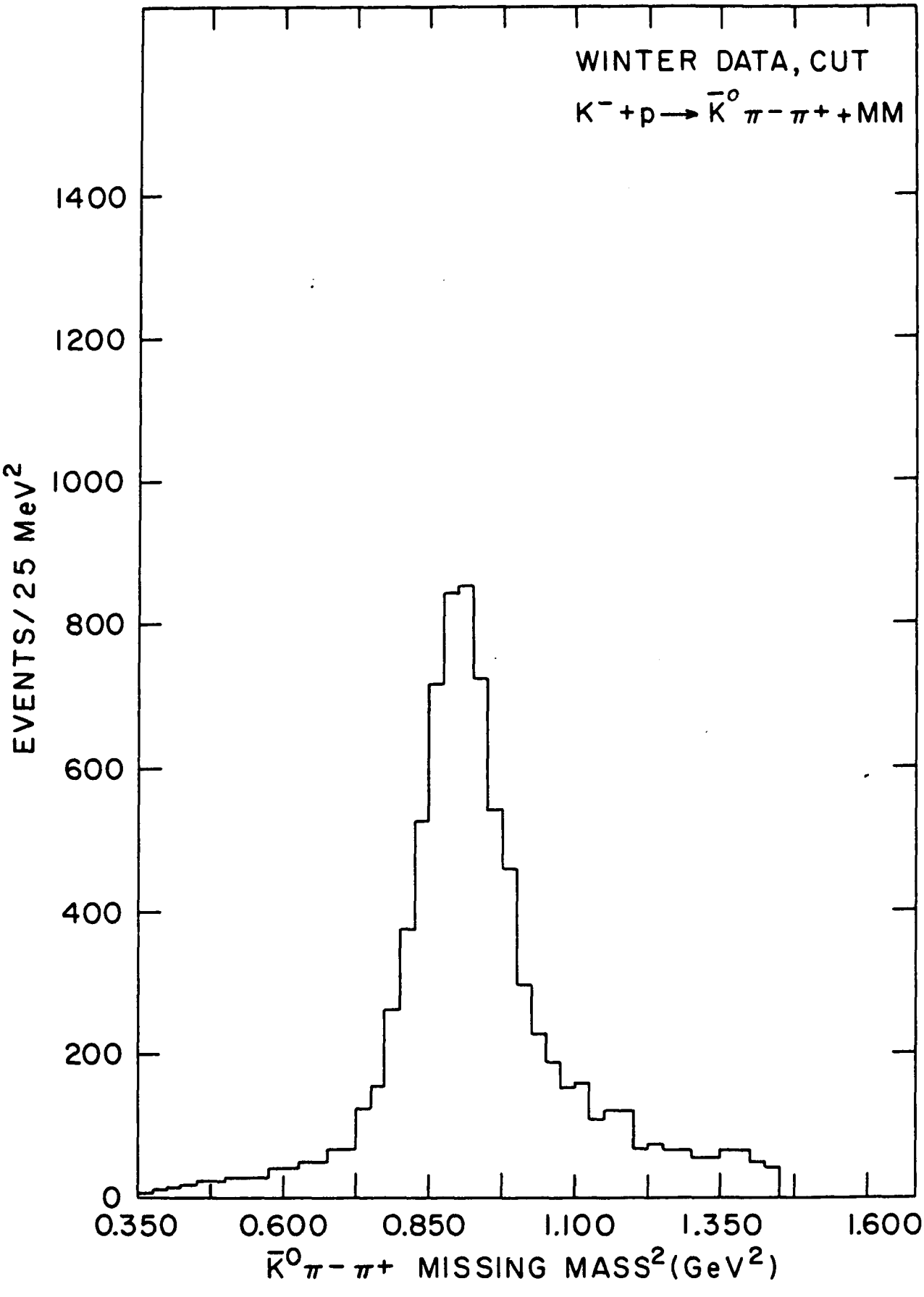
WINTER DATA, CUT
$K^- + p \rightarrow \bar{K}^o \pi^- \pi^+ + MM$
EVENTS/25 MeV^2
1400
1200
1000
800
600
400
200
0
0.350
0.600
0.850
1.100
1.350
1.600
$\bar{K}^0 \pi^- \pi^+$ MISSING MASS^2(GeV^2)

TABLE 14

Type of Cuts and Their Ranges Used for the Fall and the Winter Data

	Cuts	Range in Fall data	Range in Winter data	Used in Selecting final data sample or Kinematics
i)	$K_s^o \bar{\pi} \pi^+$ (missing mass)^2	.7875 to 1.0375 GeV^2	.75 to 1.05 GeV^2	Selection
ii)	K_s^o effective mass	.490 to .502 GeV	.489 to .503 GeV	Selection
iii)	K_s^o -Λ overlap	1.11 to 1.12 GeV	1.11 to 1.12 GeV	Selection
iv)	$K_s^o \pi^-$ P (missing mass)^2	-.01 to .09 Gev^2	-.01 to 09 GeV^2	Selection
v)	$\Delta z/\delta z$	$\geq$ 2.0	$\geq$ 2.0	Selection
vi)	K*(890) cut (inclusive)†	.83 to .9[illegible] GeV	.83 to .95 GeV	Kinem
vii)	K*(890) cut (exclusive)†	.80 to .98 GeV	.80 to .98 GeV	Kinem
viii)	ρ cut (inclusive)	.62 to .92 GeV	.62 to .92 GeV	Kinem

† K^* (890) cut (inclusive) was for investigating $K^*(890)^-\pi^+$ intermediate isobaric state, defined as '$K^*(890)$ in' channel later; $K^*(890)$ cut (exclusive) was for investigating $K_s^o\pi^-\pi^+$ state, without intermediate $K^*(890)$ production, - defined as '$K^*(890)$ out' channel later.

TABLE 15

Number of Events Survived after Various Cuts
(after fiducial vol. cut and $\chi^2 \leq 1.4$ cut in constrained fit)

Type of Cuts	Fall		Winter	
	Events	% Lost	Events	% Lost
Total K_S^o $\pi^+\pi^-$ events on the final H-tape	26241		15882	
after ii) cut in Table 14	18075	31%	11417	28%
after iii) cut in Table 14	26122	.5%	15826	.4%
after iv) cut in Table 14	20882	20%	13630	14%
after v) "	20401	22%	12514	21%
after ii) & iv) "	14148	46%	9766	39%
after ii), iv) & v) "	11836	55%	8155	49%
after ii), iii), iv) & v) "	11788	55%	8131	49%
in K_S^o spectrum with cuts i), iii), iv) & v)	9942	62%	7624	52%
in $K\pi\pi$ spectrum with cuts i), ii), iii), iv) & v)	7590	71%	5942	63%
" with vi)	4213		3344	
" with vii)	2741		2124	
" with viii)	3943		3151	

production angles, reactions of the kind

$$K^- p \rightarrow K^- \pi^+ \pi^- p$$

could be reconstructed as a two-particle production vertex (K^- and p) and a distinct 2-prong decay vertex (the $\pi^+\pi^-$ form a K^o_s). To reduce the number of such events only the ones with $\Delta S/\delta S \geq 2.0$ were accepted where

$\Delta S \equiv$ distance between the production and the decay vertex

$\delta S \equiv (\delta x)^2 + (\delta y)^2 + (\delta z)^2$ = error in the position measurement of the production vertex.

Since the errors in the x and the y positions (δx and δy) were negligible compared to that in z (δz) and $\Delta z \geq \Delta x, \Delta y$, the actual cut used was $\Delta z/\delta z \geq 2.0$. Typically, this amounted to a Δz of $\sim$ 1.25 cm.

4. K^o_s mass cut: the accepted mass range for K^o_s is shown in Table 14. It was determined after inspecting the K^o_s mass resolution (discussed later).

From Figs. 10a and 10b (fall and winter) we estimated the resolution of the missing mass squared to be σ = 125 MeV^2 for the fall data and σ = 150 MeV^2 for the winter data. Hence the final missing mass squared cut $\pm 2\sigma$ is listed in Table 14. The background under the spectrum was estimated to be $\sim$ 23% of the total events.

ii. Background under the K^o_s spectrum: The contamination in the K^o_s spectrum due to the misidentified Λ's was reduced by the missing mass squared cut made for the H-tape events (.36 - 1.44 GeV). The K^o_s-Λ overlap (discussed earlier) events amounted to $\sim$ 1% and were removed. Figures 11a and 11b show the $\pi^+\pi^-$ effective mass spectrum after the cuts (i, iii, iv, and v) in Table 14 were made to reduce the background

FIG. 11a EFFECTIVE MASS SPECTRUM OF $\pi^+\pi^-$ FROM THE DECAY VERTEX: FALL DATA, AFTER KINEMATIC CUTS i, iii, iv and v IN TABLE 14

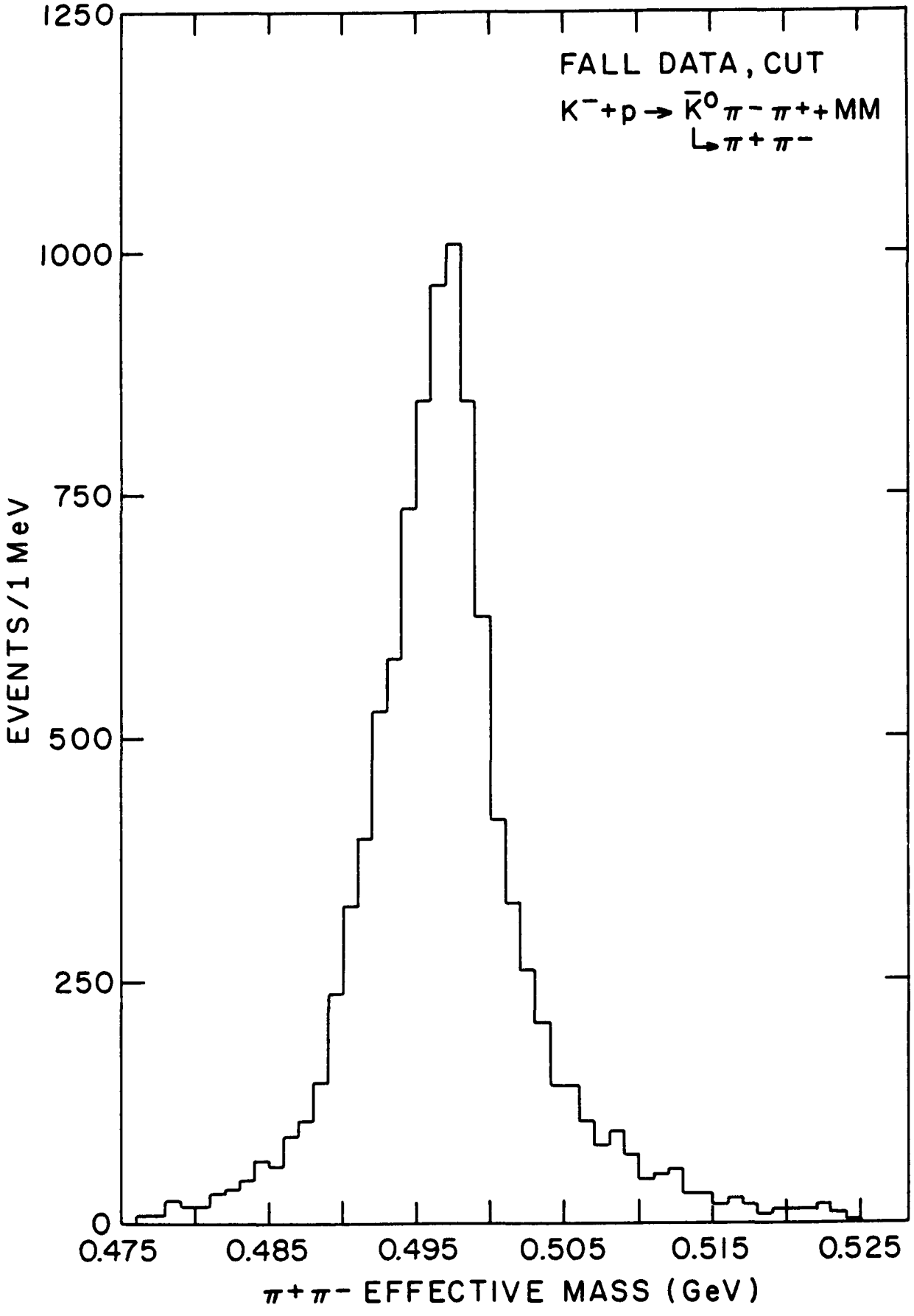
FALL DATA, CUT
K⁻+p → K̄⁰π⁻π⁺+MM
↳π⁺π⁻
EVENTS/1 MeV
1250
1000
750
500
250
0
0.475
0.485
0.495
0.505
0.515
0.525
π⁺π⁻ EFFECTIVE MASS (GeV)

FIG. 11b EFFECTIVE MASS SPECTRUM OF $\pi^+\pi^-$ FROM THE DECAY VERTEX; WINTER DATA, AFTER KINEMATIC CUTS i, iii, iv and v IN TABLE 14

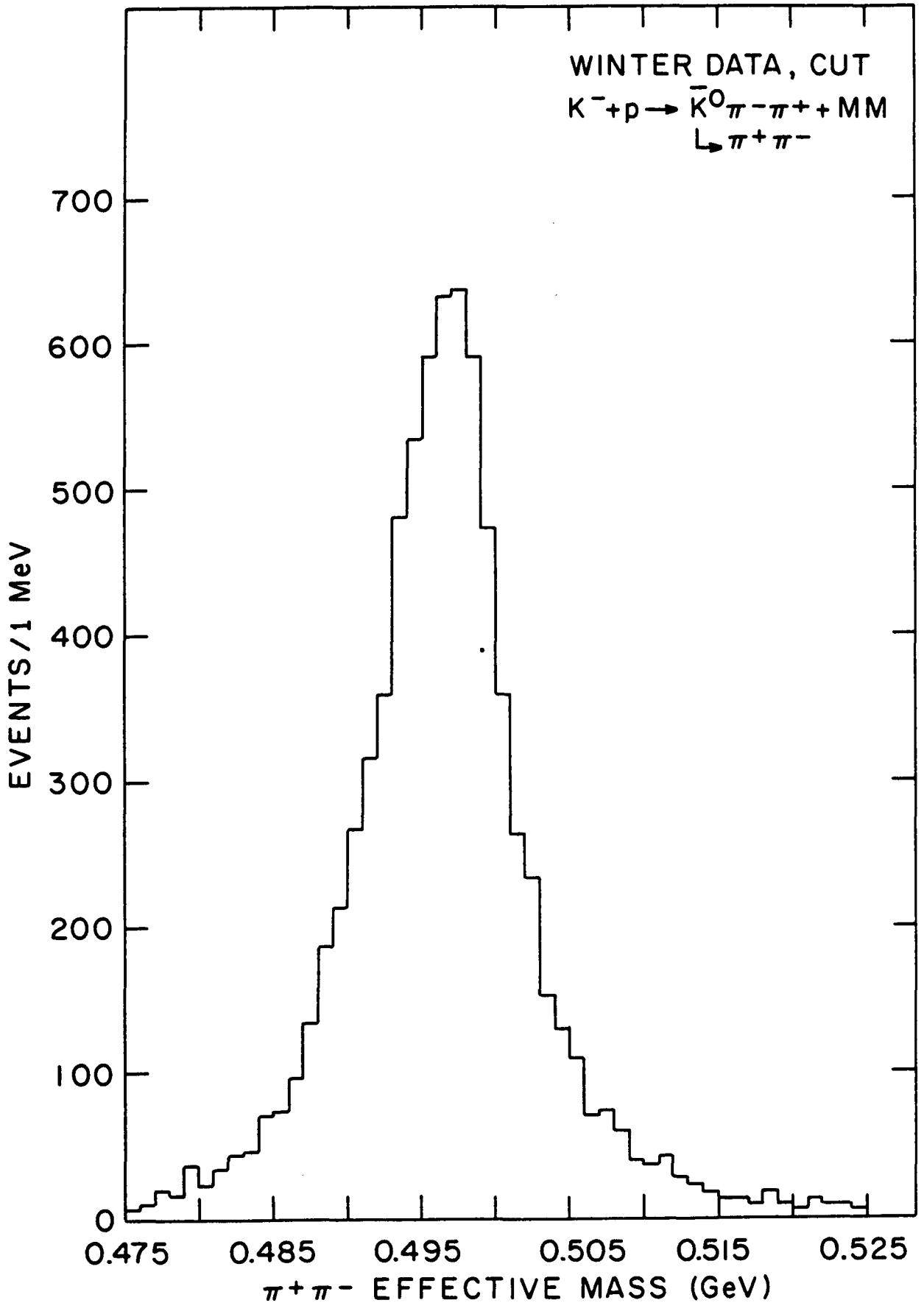
WINTER DATA, CUT
$K^- + p \rightarrow \bar{K}^0 \pi^- \pi^+ +$ MM
$\hookrightarrow \pi^+ \pi^-$
EVENTS/1 MeV
0
100
200
300
400
500
600
700
0.475
0.485
0.495
0.505
0.515
0.525
$\pi^+ \pi^-$ EFFECTIVE MASS (GeV)

under the K^o_s spectrum. The effective mass resolution (standard deviation, σ) was estimated to be

σ = 6 MeV for fall data

σ = 7 MeV for winter data.

Table 14 shows the appropriate $\pm 2\sigma$ cut for the K^o_s mass in the final data analysis.

Hence the final event sample for kinematic analysis was obtained by imposing cuts i, ii, iii, iv and v in Table 14 (in addition to the fiducial volume cut and a maximum chi-squared cut from the constrained fitting program described later) and contained a total of 13,532 events. Table 15 lists the contributions from the fall and the winter separately.

2. Corrections Applied in the Analysis

a. Beam Momentum Calibration

The incident beam spectrometer measured the incident beam momentum with respect to the nominal momentum. The absolute momentum was measured by the main spectrometer using the beam tracks. The ratio of the absolute to the nominal momentum was used to scale the incident momentum in the primary processing program.

b. $\vec{E} \times \vec{B}$ Correction

As explained in Chapter II, the spark chambers in the main spectrometer were in the MPS magnetic field ($\sim$ 10 Kg) which was mainly along the y-axis. Immediately after the ionization was caused by the charged particle going through the chamber, the electrons drifted under the influence of a DC electrostatic clearing field (in z-direction) and later under the electric field of the high voltage pulse. Coupling of

these with the y component of the MPS magnetic field resulted in a net shift in the spark position (E_z x B_y) in the x-direction. This was found to depend on the particular chamber, the region of spark formation in the chamber, the circulating gas mixture and the track angle. Some of these varied with time as well. Corrections for the spark shift were applied in the processing program in the way described below.

Beam tracks were projected onto each chamber from the beam PWC system by extrapolation through the MPS magnetic field to find the 'real' spark position. After extensive studies the difference between the 'measured' spark position and the 'real' spark position was parameterized for each chamber as

$$\Delta x = a_o + a_1(t) + b(t) \tan \theta$$

where a_o = a constant shift (chamber independent) determined by projecting the beam track on TPX1 and TPX2;

a_1 = a chamber and time dependent shift;

b = a chamber and time dependent shift.

Chamber 8SX12 and 8SX34 were reversed gap chambers, i.e., the directions of the high voltage and the clearing field were in the opposite direction from those in the other chambers. Shifts were studied more intensively in these chambers and an interesting effect was observed. The E x B shifts in the beam region were about twice as large as in the other regions. Since the data contained tracks, most of which were not in the beam region, the above parameterization obtained for the beam region was modified for the event tracks as

$$\Delta x = [a_o + a_1(t)] \times 0.4 + b(t) \tan \theta$$

The magnitude of Δx typically was 1.5 mm.

c. Energy Loss in the Target:

Before interacting with a proton in the liquid H_2 target the incident kaon lost energy by electromagnetic interaction† in the target. After the interaction charged particles lost energy the same way depending on their path length spent inside the target. The track length of the charged particles spent inside the target primarily consisted of the z-component; x and y component being negligible. Hence only the z-component of the path length was considered in this energy loss correction to calculate the missing mass. The incident K^- momentum was corrected as

$$P_{inc} = P_{beam} - (Z_{prod} - Z_{tgtu}) \times .000292 \text{ in GeV/c}$$

where

$P_{beam} \equiv$ incident momentum calculated by the analysis program;

$P_{inc} \equiv$ corrected incident beam momentum;

$Z_{tgtu} \equiv$ upstream end of the liquid Hydrogen target;

$Z_{prod} \equiv$ Z coordinate of the production vertex;

and .000292 = the energy loss coefficient in hydrogen.

The outgoing tracks momenta were corrected as:

$$P_{out} = P_o + (Z_{tgtd} - Z_{prod}) \times .000292$$

for the two pion tracks from the product vertex and,

$$P_{out} = P_o + (Z_{tgtd} - Z_{dcy}) \times .000292$$

if $Z_{tgtd} > Z_{dcy}$;

$$P_{out} = P_o$$

if $Z_{tgtd} < Z_{dcy}$ for the tracks from the decay vertex, where

$P_o \equiv$ the measured track momentum;

$P_{out} \equiv$ the corrected track momentum at the vertex;

---

† ionization loss

Z_{tgtd} ≡ downstream end of the target;

Z_{dcy} ≡ Z coordinate of the decay vertex.

This correction was applied in the summary tape processing program.

3. Treatment of the Final Data Sample and Mass Spectra

As mentioned earlier in this Chapter, the final selection of the events was done by using cuts i, ii, iii, iv and v of Table 14. Figure 12 shows the $K_s^o\pi^+\pi^-$ effective mass spectrum for the final event sample. The other cuts (vi, vii and viii) listed in Table 14 were used to select final states through different channels, e.g., intermediate isobar production.†

To understand the non-resonant background in the $K_s^o\pi^+\pi^-$ effective mass spectrum (Fig. 12), we looked into the possibility of Δ^+ production due to the reaction

$$K^-p \rightarrow K^*(890)^- + \Delta^+$$
$$\hookrightarrow \pi^+ + n$$

as follows:

The $K_s^o\pi^-$ effective mass spectrum was inspected (Fig. 13).†† The mass resolution was found to be ∿ 9 MeV by a maximum likelihood fit to the spectrum. Figure 14 shows the scatter plot of the effective mass of $K_s^o\pi^-$ vs. the missing mass recoiling from $(K_s^o\pi^-)$. A $K^*(890)$ band and some $K^*(1420)$ are apparent in Fig. 14, but there is no band in the missing mass from the $K_s^o\pi^-$ in the $\Delta(1236)$ region.

---

† In later discussions, the $K_s^o\pi^-\pi^+$ state through intermediate $K^*(890)$ isobaric decay will be referred to as '$K^*(890)$ in' channel and without the intermediate $K^*(890)$ state as '$K^*(890)$ out' channel.

†† Fall and winter data are combined unless otherwise specified.

FIG. 12 EFFECTIVE MASS SPECTRUM OF $K_S^o \pi^- \pi^+$ FROM THE FINAL DATA SAMPLE (UNCONSTRAINED DATA)

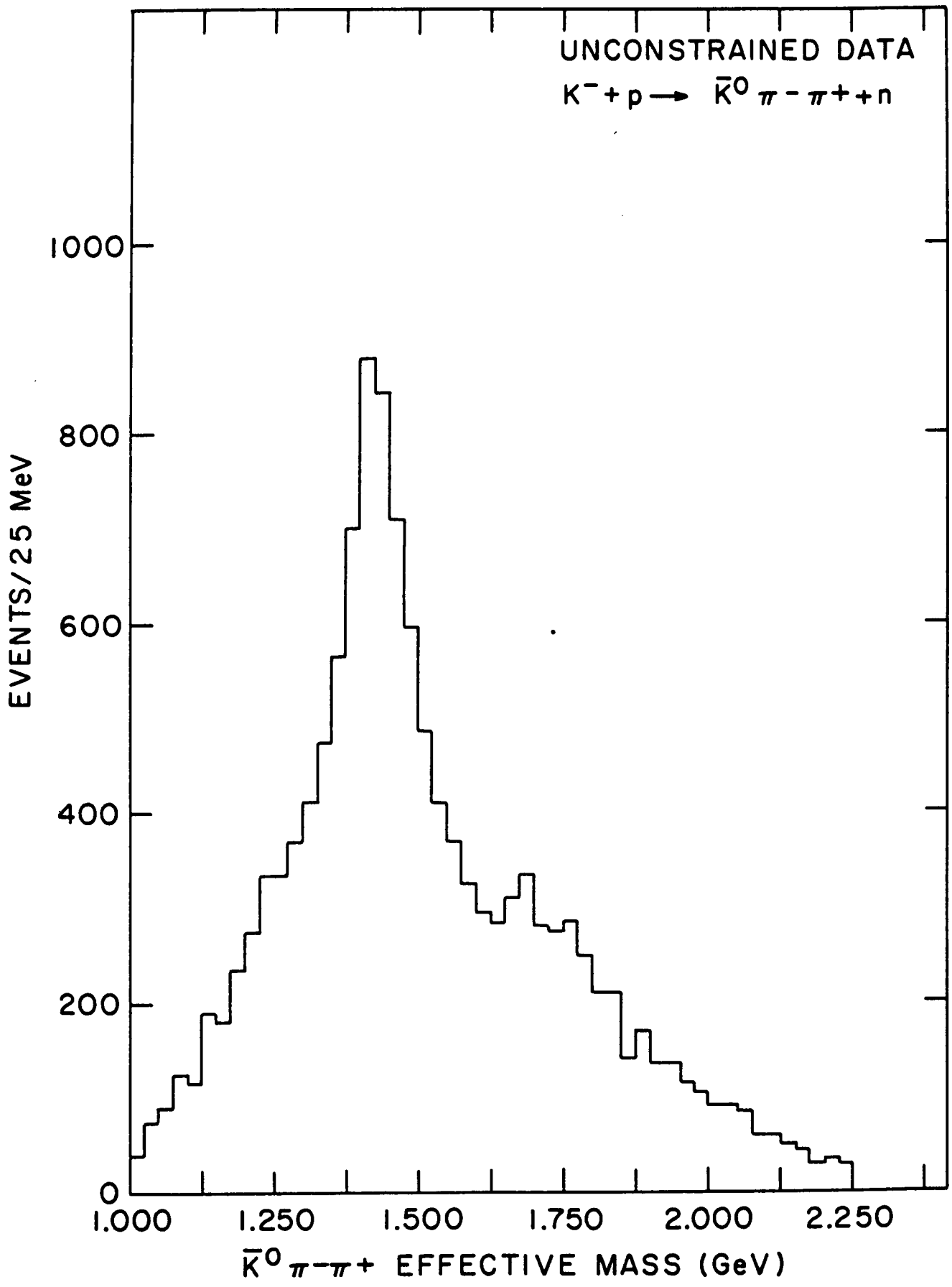
UNCONSTRAINED DATA
$K^- + p \rightarrow \bar{K}^0 \pi^- \pi^+ + n$
EVENTS/25 MeV
0
200
400
600
800
1000
1.000
1.250
1.500
1.750
2.000
2.250
$\bar{K}^0 \pi^- \pi^+$ EFFECTIVE MASS (GeV)

FIG. 13 EFFECTIVE MASS SPECTRUM OF $K_S^o \pi^-$ FROM THE FINAL DATA SAMPLE (UNCONSTRAINED DATA)

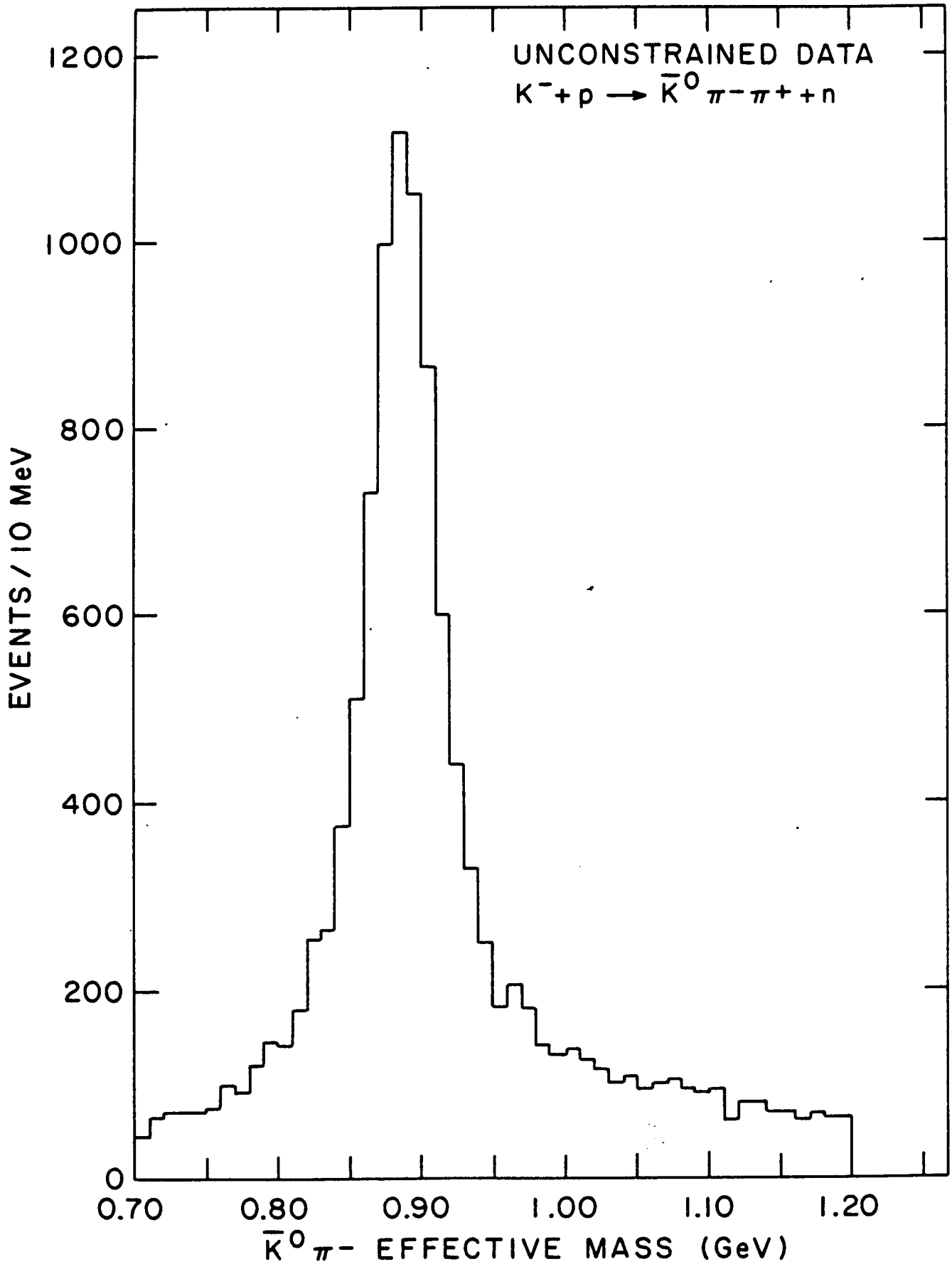
UNCONSTRAINED DATA
$K^- + p \rightarrow \bar{K}^0 \pi^- \pi^+ + n$
EVENTS / 10 MeV
1200
1000
800
600
400
200
0
0.70
0.80
0.90
1.00
1.10
1.20
$\bar{K}^0 \pi^-$ EFFECTIVE MASS (GeV)

FIG. 14 SCATTER PLOT OF THE MISSING MASS RECOILING FROM $K_s^o \pi^-$ VS. THE EFFECTIVE MASS OF $K_s^o \pi^-$

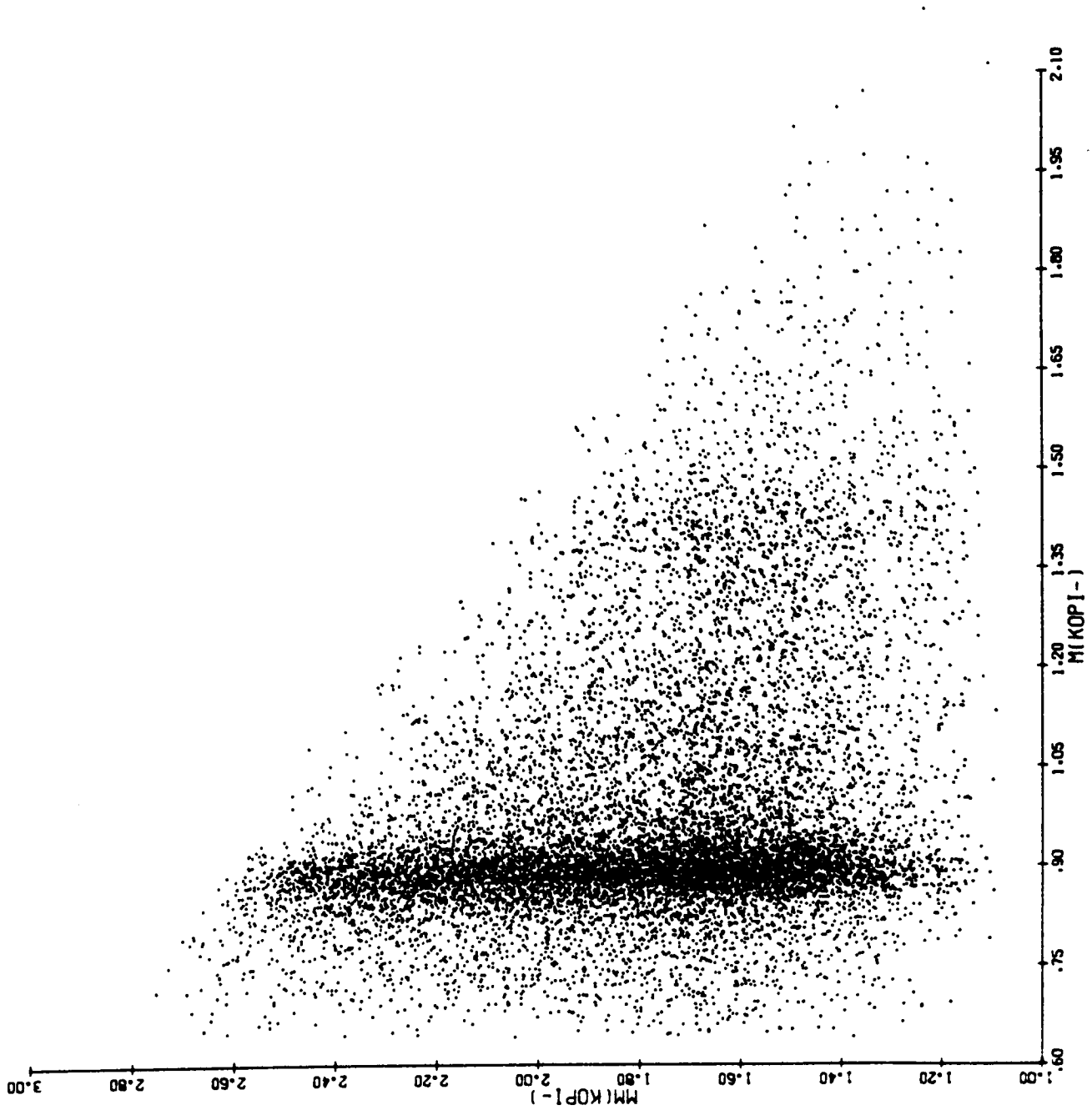
MM(KOPI-)
1.00
1.20
1.40
1.60
1.80
2.00
2.20
2.40
2.60
2.80
3.00
M(KOPI-)
.60
.75
.90
1.05
1.20
1.35
1.50
1.65
1.80
1.95
2.10

The selected data sample (with cuts i, ii, iii, iv and v, in Table 14) was then fitted using kinematic constraints on an event-by-event basis. The missing mass from $K_s^o\pi^-\pi^+$ and the effective $\pi^+\pi^-$ mass at the decay vertex were fixed as the mass of neutron and $\bar{K}^o$ respectively. The production vertex was also fitted to a point along the line of the reconstructed K_s^o, the two pion tracks (forming the production vertex) and the incident beam. All the following discussions of the data refer to the kinematically constrained data.

Figure 15 shows the $K_s^o\pi^-$ effective mass spectrum thus fitted with constraints. Figure 16 shows the $K_s^o\pi^-\pi^+$ effective mass spectrum with the same constraints. A peak at $\sim$ 1.42 GeV and another between 1.7 GeV and 1.8 GeV are apparent.

Intermediate isobar production channels:

i. K^* (890): Figures 17 and 18 show the effective mass spectra of $K_s^o\pi^-\pi^+$ which decayed through an intermediate state of K^* (890) {i.e., K^* (890) in} and the ones that did not decay through the intermediate K^* (890) {i.e., K^* (890) out} respectively. As shown in Table 14, $\pm 2\sigma$ and 3σ cuts were used for the 'K^* (890) in' and the 'K^* (890) out' decay channels respectively. Figure 17 shows a clear 1420 MeV peak and some hint of a structure at $\sim$ 1780 MeV. Figure 18 shows two almost comparable bumps at $\sim$ 1420 MeV and $\sim$ 1720 MeV, and it is a rather complicated spectrum. A maximum likelihood fit was done to both the spectra, parameters and results of which are discussed

FIG. 15 EFFECTIVE MASS SPECTRUM OF $K_S^o \pi^-$ FROM THE FINAL DATA SAMPLE (CONSTRAINED DATA)

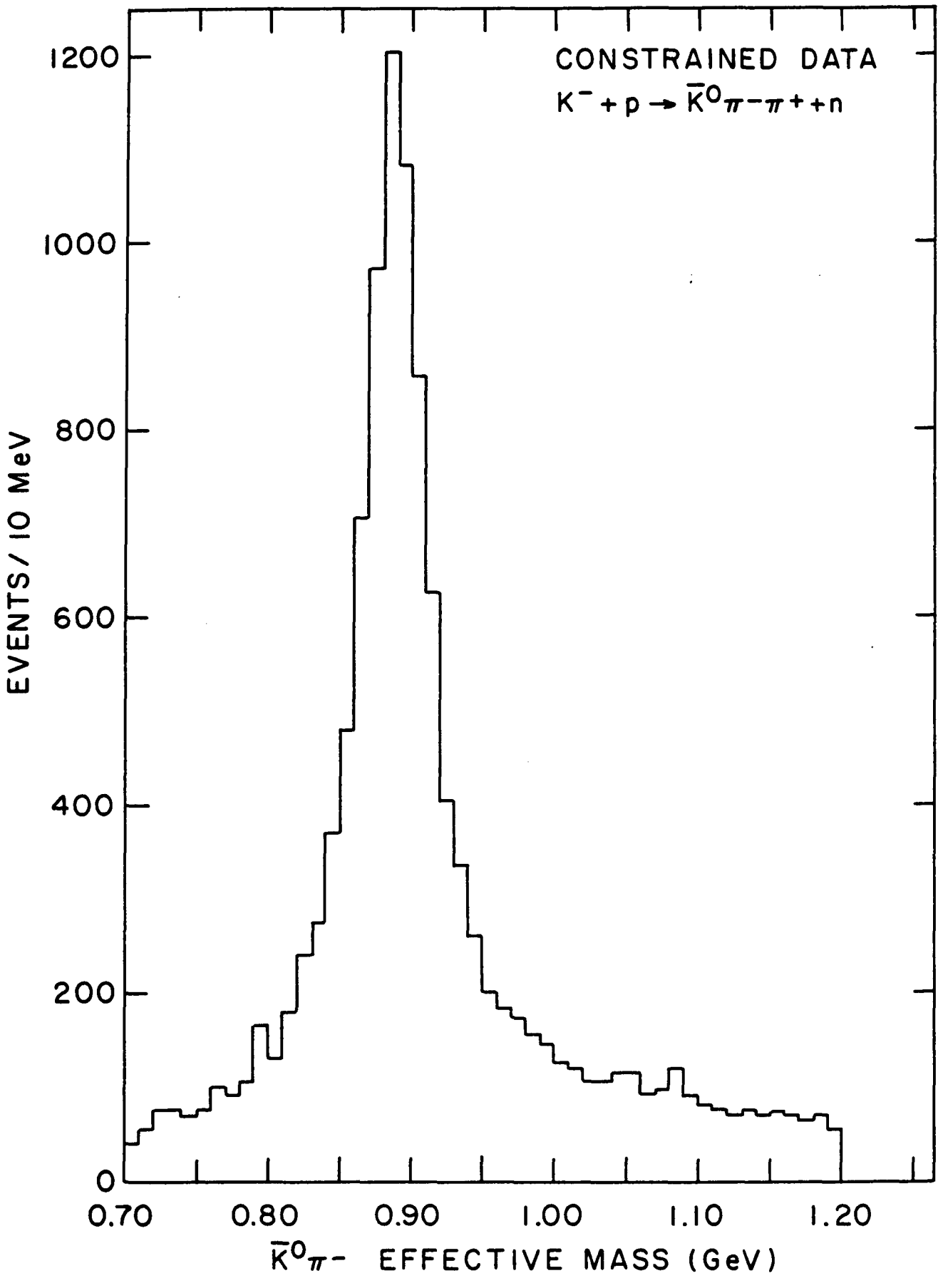
CONSTRAINED DATA
$K^- + p \rightarrow \bar{K}^0 \pi^- \pi^+ + n$
EVENTS / 10 MeV
0
200
400
600
800
1000
1200
0.70
0.80
0.90
1.00
1.10
1.20
$\bar{K}^0 \pi^-$ EFFECTIVE MASS (GeV)

FIG. 16 EFFECTIVE MASS SPECTRUM OF $K_s^o \pi^- \pi^+$ FROM THE FINAL DATA SAMPLE (CONSTRAINED DATA)

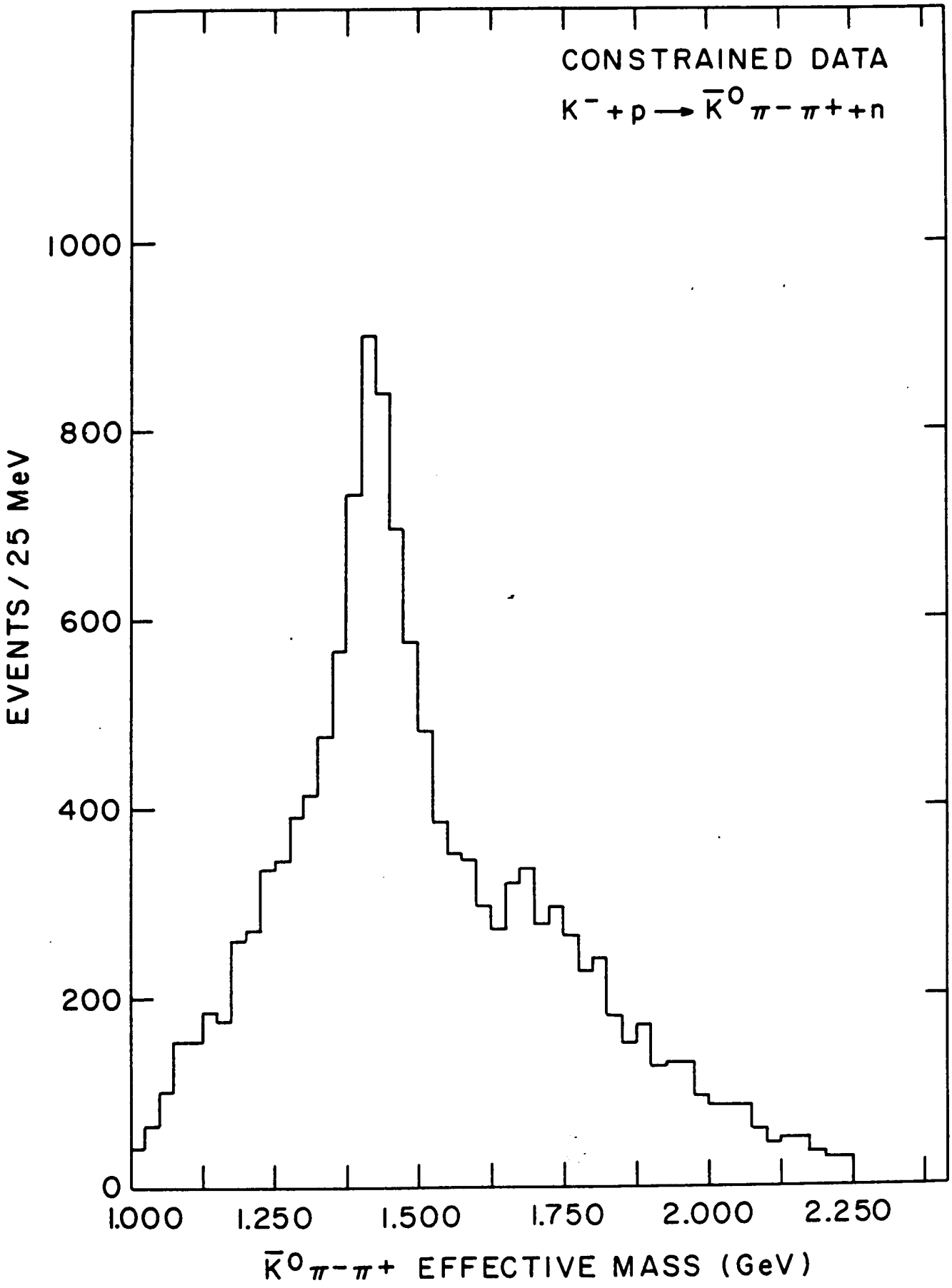
CONSTRAINED DATA
$K^- + p \rightarrow \bar{K}^0 \pi^- \pi^+ + n$
EVENTS / 25 MeV
0
200
400
600
800
1000
1.000
1.250
1.500
1.750
2.000
2.250
$\bar{K}^0 \pi^- \pi^+$ EFFECTIVE MASS (GeV)

FIG. 17 EFFECTIVE MASS SPECTRUM OF $K_S^o \pi^- \pi^+$ REQUIRING EFFECTIVE MASS OF $K_S^o \pi^-$ BETWEEN 0.83 GeV AND 0.95 GeV (CONSTRAINED DATA) -'$K^*(890)$ IN' CHANNEL

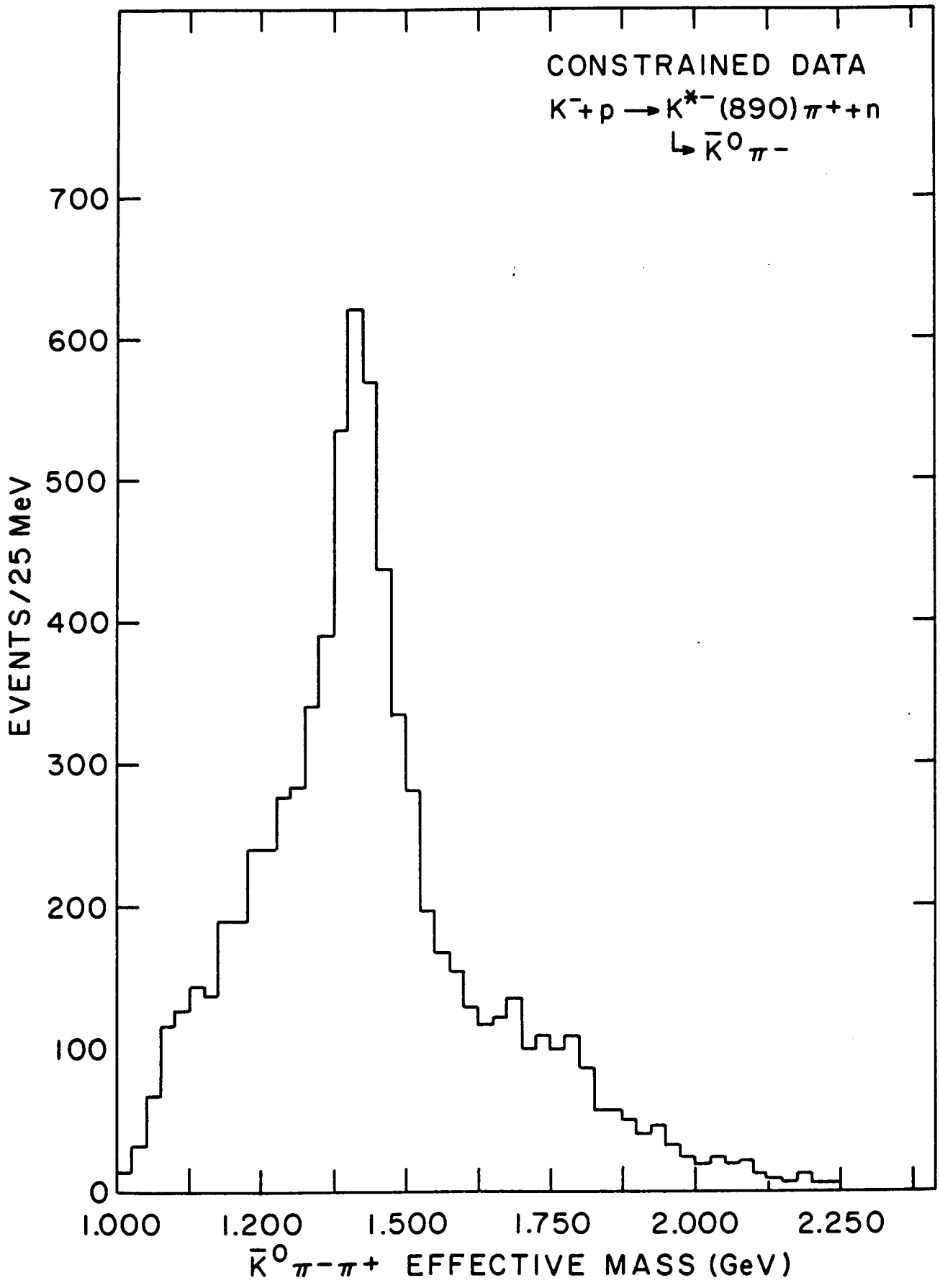
CONSTRAINED DATA
K⁻+p → K*⁻(890)π⁺+n
↳ K̄⁰π⁻
EVENTS/25 MeV
0
100
200
300
400
500
600
700
1.000
1.200
1.500
1.750
2.000
2.250
K̄⁰π⁻π⁺ EFFECTIVE MASS (GeV)

FIG. 18 EFFECTIVE MASS SPECTRUM OF $K_S^o\pi^-\pi^+$ REQUIRING THE EFFECTIVE MASS OF $K_S^o\pi^-$ TO BE OUTSIDE OF THE MASS REGION BETWEEN .80 GeV and .98 GeV (CONSTRAINED DATA) - 'K^* (890) OUT' CHANNEL.

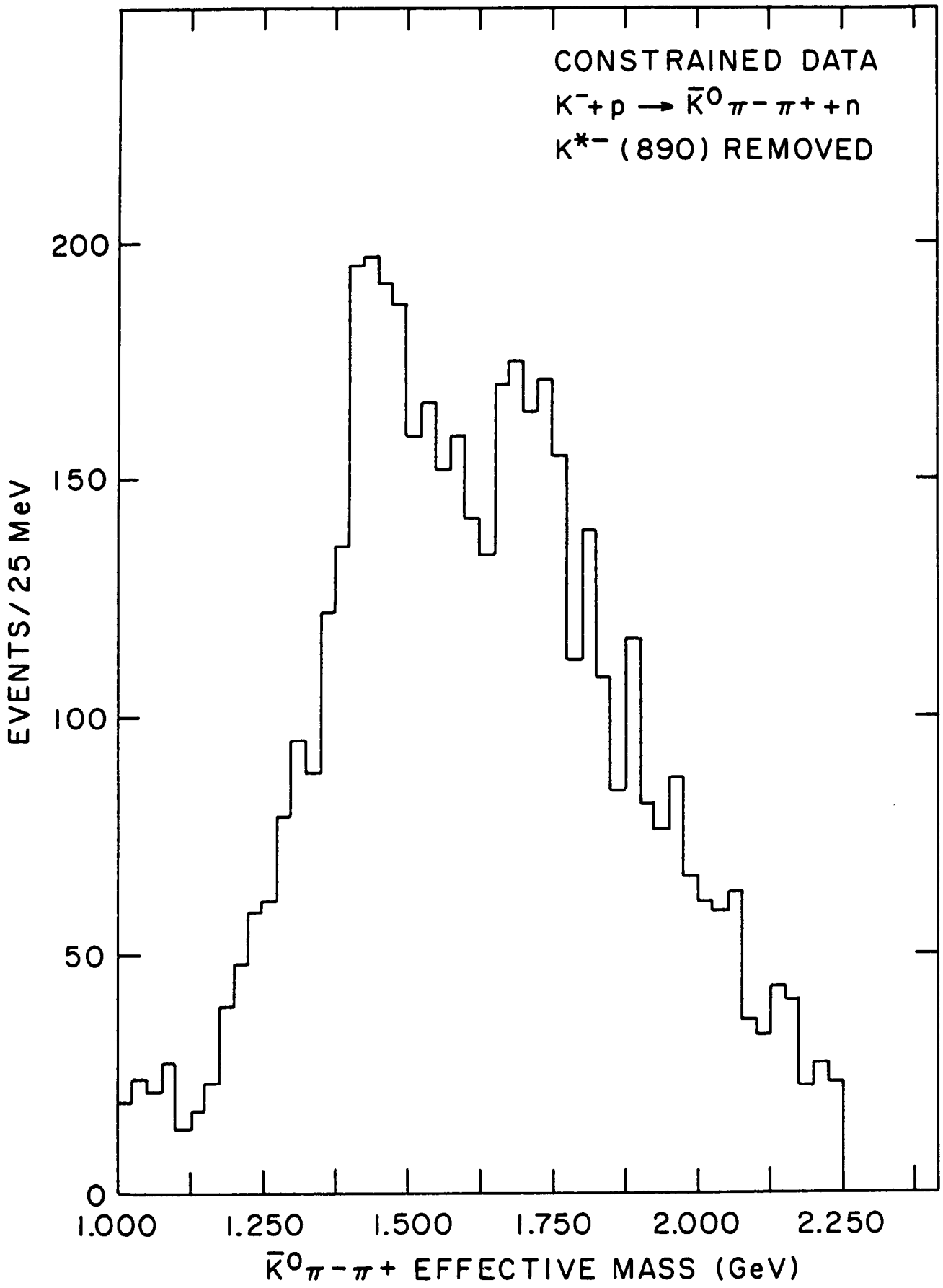
CONSTRAINED DATA
K⁻+p → K̄⁰π⁻π⁺+n
K*⁻(890) REMOVED
EVENTS/25 MeV
0
50
100
150
200
1.000
1.250
1.500
1.750
2.000
2.250
K̄⁰π⁻π⁺ EFFECTIVE MASS (GeV)

later. The acceptances used in all these cases are described in detail later as well.

ii. $\rho(770)$: Figure 19 shows the $K_s^o\pi^-\pi^+$ effective mass spectrum that decay through the intermediate $K_s^o\rho$ state. Since a big overlap between $K^*(890)$ and ρ exist in phase space and ρ is a rather wide resonance, we took the '$K^*(890)$ out' spectrum and made a ρ cut as shown in Table 14. Thus, Fig. 19 excludes the contribution from the $K^*(890)$ isobaric state. A $K^*(1420)$ bump and a structure at $\sim$ 1700 MeV are apparent in Fig. 19. Figure 20 shows a scatter plot of $K_s^o\pi^-$ effective mass vs. $\pi^+\pi^-$ (from the production vertex) effective mass. The overlap between the $K^*(890)$ and ρ is apparent.

4. Acceptance Calculation

a. Using Phase Space Only

The geometric acceptance of the apparatus was calculated using a Monte Carlo program with very high statistics. Events were generated in the center-of-mass system according to the reactions

$$K^-p \to \bar{K}^{**o} + n \qquad (1)$$
$$\bar{K}^{**o} \to K_s^o + \pi^- + \pi^+$$
$$K_s^o \to \pi^+ + \pi^-$$

$$K^-p \to \bar{K}^{**o} + n \qquad (2)$$
$$\bar{K}^{**o} \to K^*(890)^- + \pi^+$$
$$K^*(890)^- \to K_s^o + \pi^-$$
$$K_s^o \to \pi^- + \pi^+$$

FIG. 19 EFFECTIVE MASS SPECTRUM OF $K_s^o \pi^- \pi^+$ THROUGH $K_s^o \rho$ INTERMEDIATE ISOBARIC STATE (CONSTRAINED DATA). IN ORDER TO REMOVE THE OVERLAP BETWEEN $K^*(890)\pi$ AND $\bar{K}^o\rho$, EVENTS WITH $K_s^o\pi^-$ EFFECTIVE MASS BETWEEN .80 GeV and .98 GeV WERE REMOVED AS IN FIG. 18.

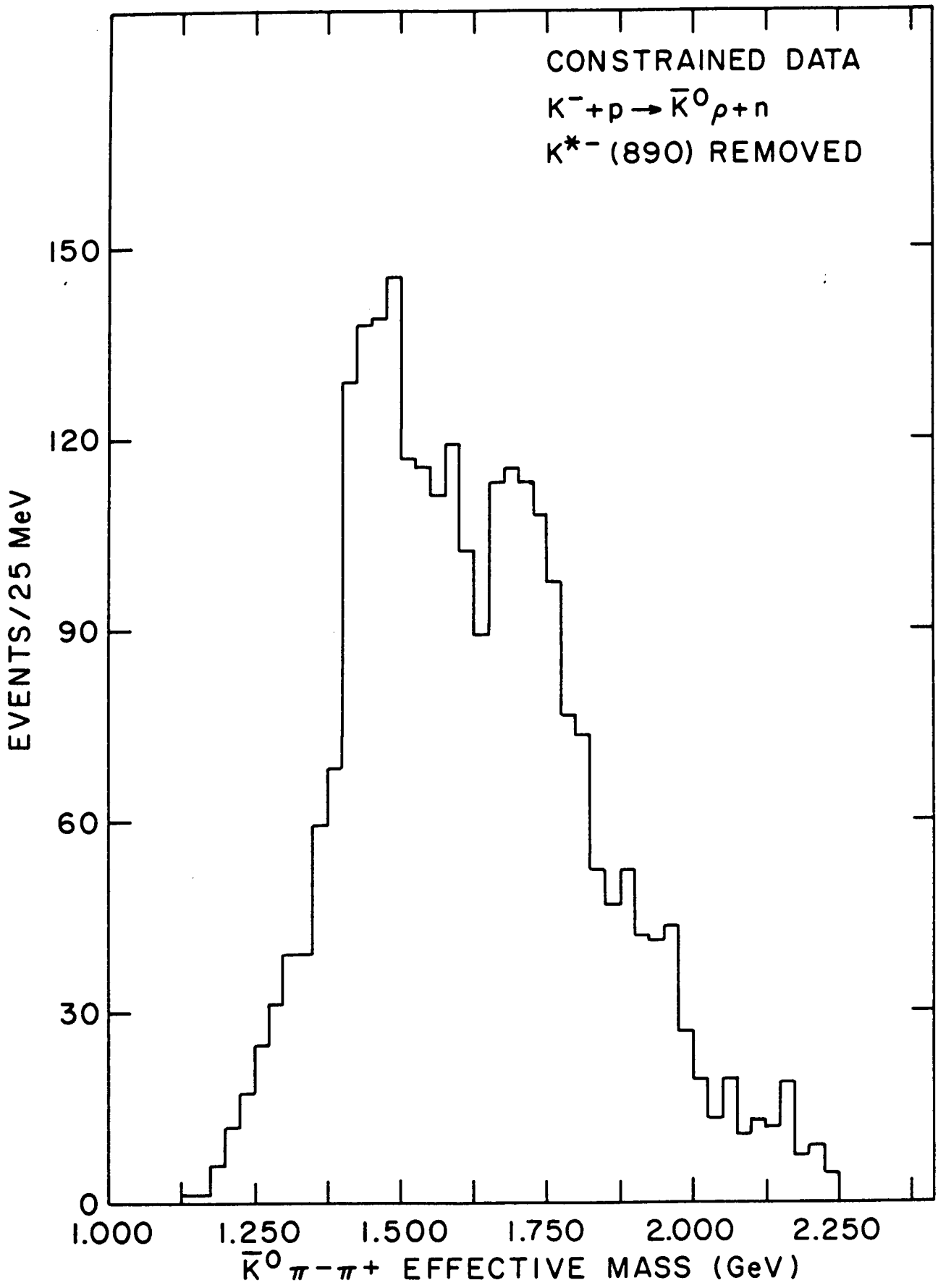
CONSTRAINED DATA
$K^- + p \rightarrow \bar{K}^0 p + n$
$K^{*-}(890)$ REMOVED
EVENTS/25 MeV
0
30
60
90
120
150
1.000
1.250
1.500
1.750
2.000
2.250
$\bar{K}^0 \pi^- \pi^+$ EFFECTIVE MASS (GeV)

FIG. 20 SCATTER PLOT OF THE EFFECTIVE MASS OF $K_s^o \pi^-$ VS. THE EFFECTIVE MASS OF $\pi^+\pi^-$, CONSTRAINED DATA

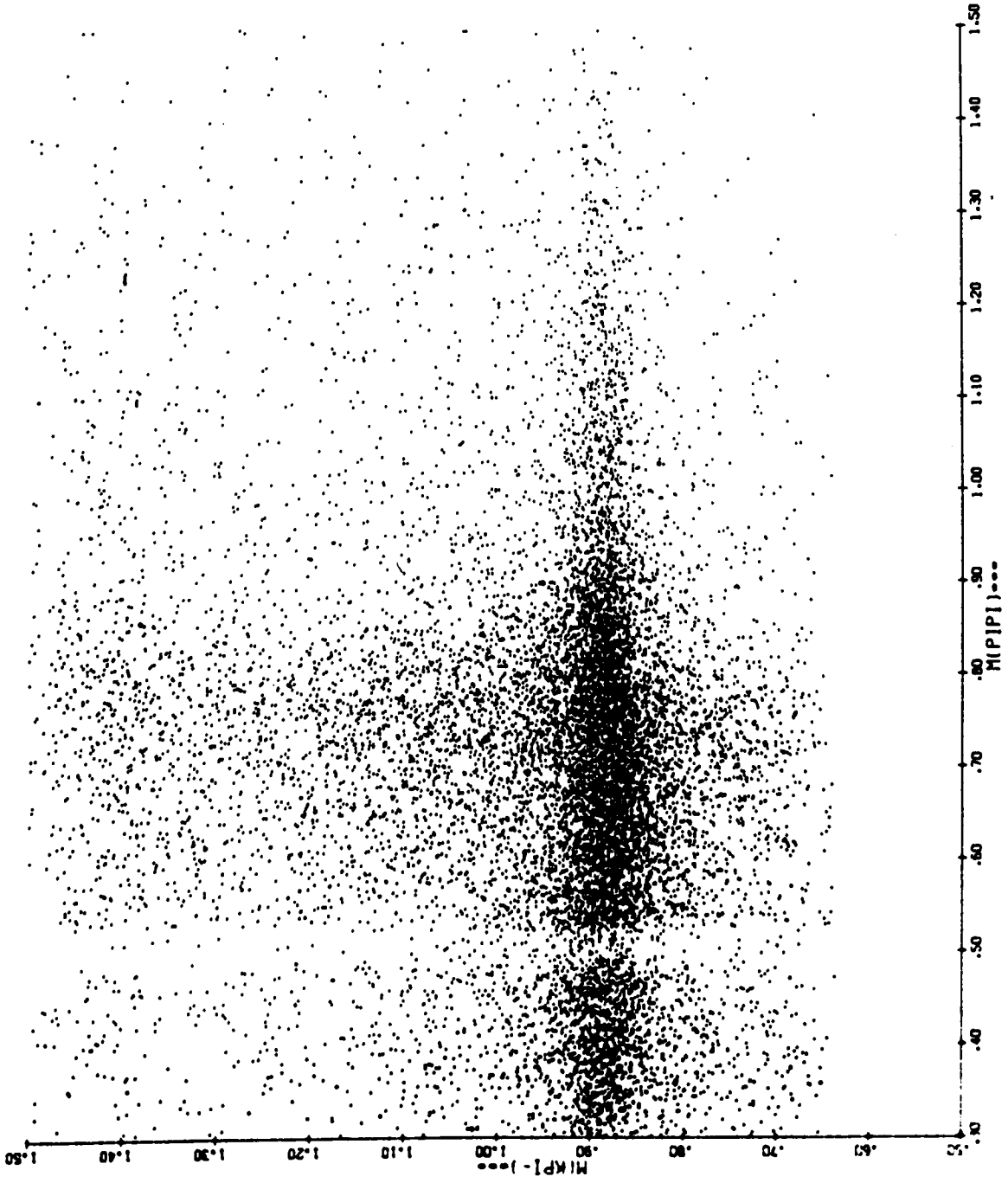
M(P1P1)***
M(KP1-)***

$$K^- p \rightarrow \bar{K}^{**o} + n \qquad (3)$$
$$\bar{K}^{**o} \rightarrow K^o_s + \rho$$
$$K^o_s \rightarrow \pi^- + \pi^+ \qquad \rho \rightarrow \pi^- + \pi^+$$

(where $\bar{K}^{**o}$ stands for the $\bar{K}^o\pi^-\pi^+$ resonance) at an incident momentum of 6 GeV/c. The production was done according to $d\sigma/dt' \propto e^{-4t'}$, where $t' = t - t_{min}$, is negative of the square of the four momentum transfer. Events were generated for a $\bar{K}^{**}$ mass range of 1.0 to 2.5 GeV. Decay of the $\bar{K}^{**}$ was performed according to 3-body phase space in Reaction 1 and 2-body final states in Reactions 2 and 3 where an intermediate stage of isobar production takes place. An isotropic angular decay distribution was assumed for the $\bar{K}^{**o}$, $K^*(890)^-$ or ρ in the respective rest system.

The geometry of the real apparatus was simulated in the program. Once the particles were generated they were swum through the MPS magnetic field with proper detector apertures. The trigger requirements were simulated by imposing equivalent constraints on the tracks generated and trigger detector efficiencies. Input from the real data was used whenever possible (e.g., the t-distribution of the data corrected for the t-acceptance was used to establish the production t-slope). Identical cuts were made in the Monte Carlo and the data.

To check if the Monte Carlo simulated the data properly, the following distributions were compared between the Monte Carlo generated events and the real data.

i. Momentum of each of the four charged pions;

ii. Event distribution vs. z (i.e., events reaching various chambers).

iii. Track length distribution vs. z (i.e., tracks reaching various chambers).

iv. Angular distribution in the Gottfried-Jackson frame of the $\bar{K}^{**}$.

Fiducial cuts were imposed on the data and the Monte Carlo events in order to accept events only from the region where the acceptance was well understood (i.e., where there was good agreement between the two). For example, reasonable agreement was obtained once all the track lengths were required to be at least as far as 5SX34 ($\sim$ 145 cm downstream from the center of the target).

The acceptances were plotted in 50 MeV bins for $K_s^o\pi^-\pi^+$ effective mass. A polynomial fit to the acceptances was used. Figure 21a shows the acceptance vs. mass curve generated using the three-body phase space (Reaction 1). Figure 21b shows the acceptance vs. mass curve for the case with the $K^*(890)$ isobar state (Reaction 2).

Figure 21c shows the acceptance for $K_s^o\pi^-\pi^+$ production in '$K^*(890)$ out' channel. This was obtained by generating $K_s^o\pi^-\pi^+$ by the 3-body phase space decay of $\bar{K}^{**}$ and removing those events for which the invariant mass of the K_s^o and π^- fell within .8 to .98 GeV [$\pm 3\sigma$ of $K^*(890)$] as shown in Table 14. Figure 21d shows the $K_s^o\pi^-\pi^+$ acceptance for $\bar{K}^o\rho$ isobaric intermediate state where the events with the $K_s^o\pi^-$ invariant mass between .8 and .98 GeV were removed.

b. Using Acceptance Moments

As described earlier in Chapter 1, a detailed analysis of the K^* resonances is quite involved mainly due to the interference of the various partial waves present in the spectrum. Ideally, in

FIG. 21a ACCEPTANCE VS. $K_s^o \pi^-\pi^+$ EFFECTIVE MASS. THREE BODY PHASE SPACE DECAY WAS ASSUMED. (Solid line denotes the polynomial fit to the acceptance.)

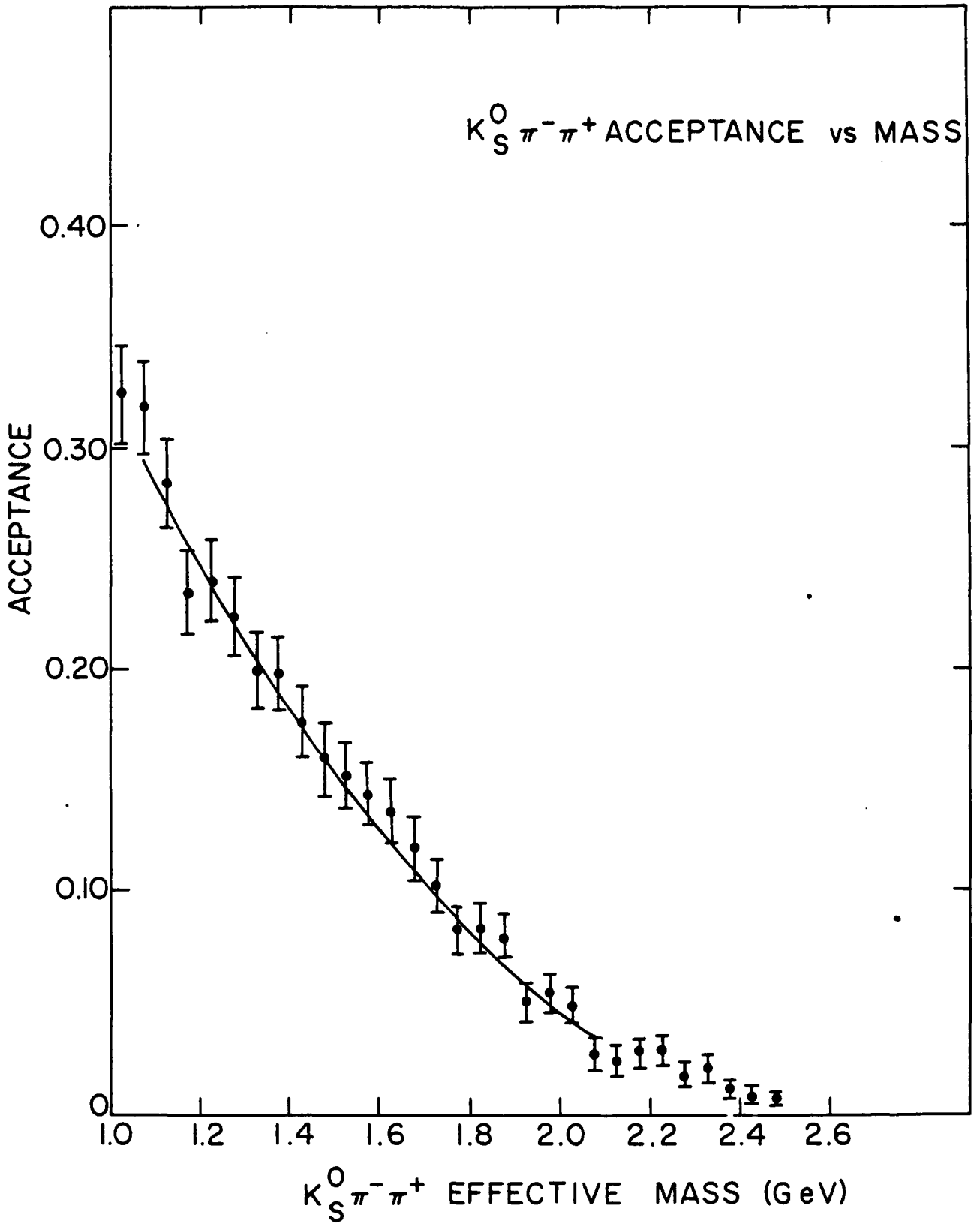
$K^0_S \pi^- \pi^+$ ACCEPTANCE vs MASS
ACCEPTANCE
0.40
0.30
0.20
0.10
0
1.0
1.2
1.4
1.6
1.8
2.0
2.2
2.4
2.6
$K^0_S \pi^- \pi^+$ EFFECTIVE MASS (GeV)

FIG. 21b ACCEPTANCE VS. $K_s^o \pi^- \pi^+$ EFFECTIVE MASS. $K^*(890)^- \pi^+$ ISOBARIC INTERMEDIATE STATE WAS ASSUMED. (Solid line denotes the polynomial fit to the acceptance.)

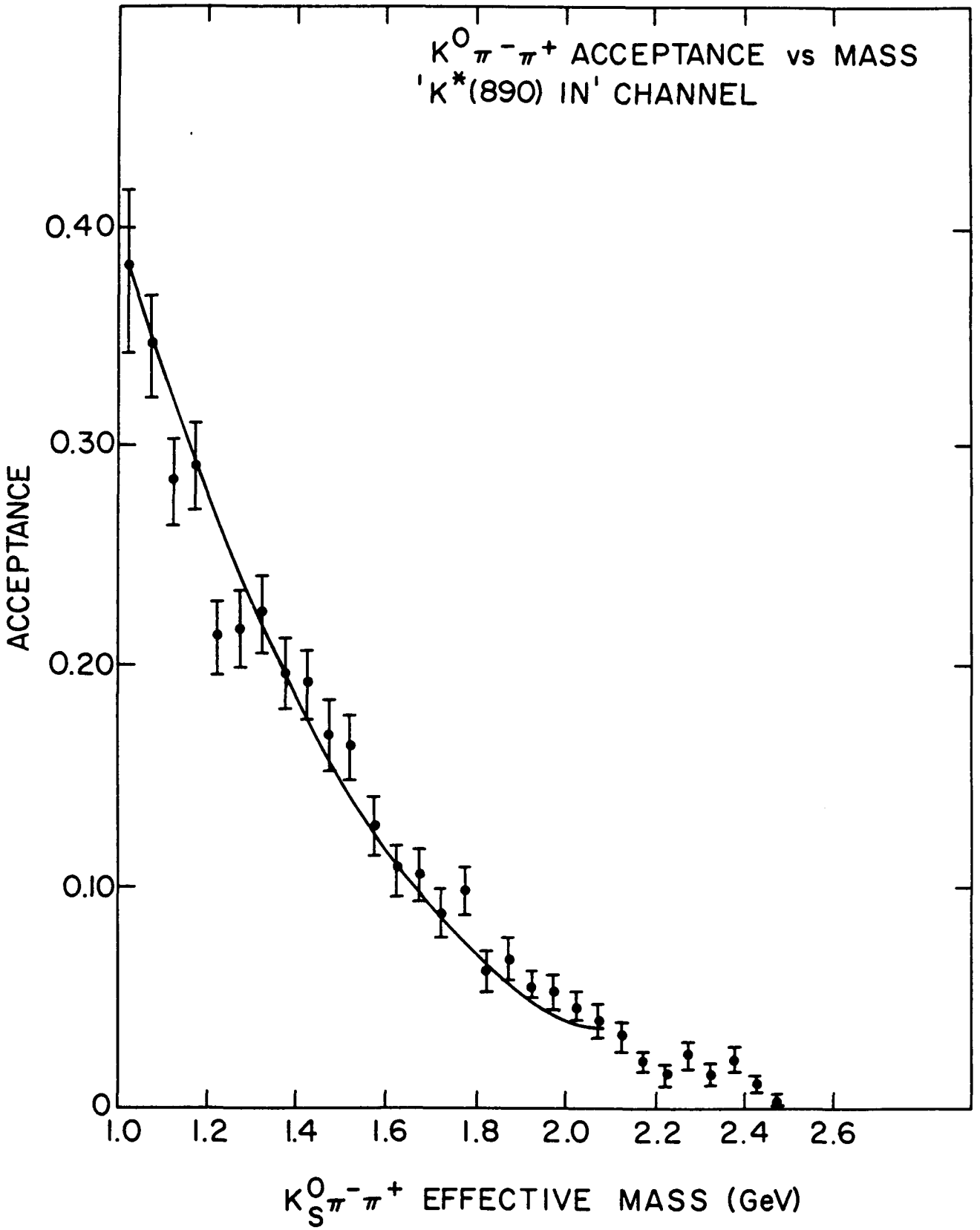
$K^0\pi^-\pi^+$ ACCEPTANCE vs MASS
'$K^*(890)$ IN' CHANNEL
ACCEPTANCE
0.40
0.30
0.20
0.10
0
1.0
1.2
1.4
1.6
1.8
2.0
2.2
2.4
2.6
$K^0_S\pi^-\pi^+$ EFFECTIVE MASS (GeV)

FIG. 21c ACCEPTANCE VS. $K_s^o \pi^- \pi^+$ EFFECTIVE MASS. THREE BODY PHASE SPACE DECAY WAS ASSUMED AND MONTE CARLO EVENTS WITH $K_s^o \pi^-$ EFFECTIVE MASS BETWEEN .80 GeV AND .98 GeV REMOVED. (Solid line denotes the polynomial fit to the acceptance.)

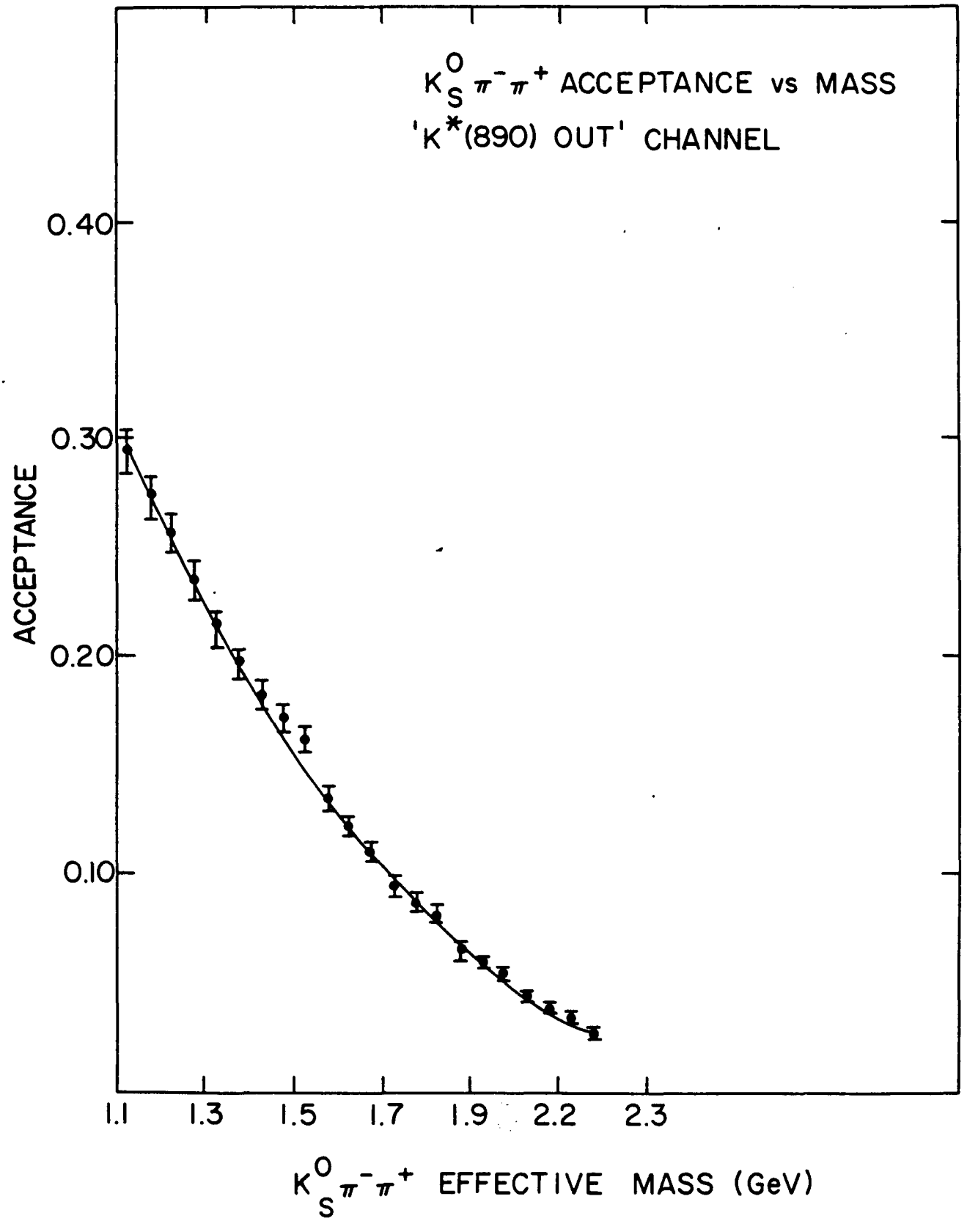
$K^0_S \pi^- \pi^+$ ACCEPTANCE vs MASS
'K*(890) OUT' CHANNEL
0.40
0.30
0.20
0.10
ACCEPTANCE
1.1
1.3
1.5
1.7
1.9
2.2
2.3
$K^0_S \pi^- \pi^+$ EFFECTIVE MASS (GeV)

FIG. 21d ACCEPTANCE VS. $K^o_s\pi^-\pi^+$ EFFECTIVE MASS. $\bar{K}^o\rho$ ISOBARIC INTERMEDIATE STATE ASSUMED. MONTE CARLO EVENTS WITH $K^o_s\pi^-$ EFFECTIVE MASS BETWEEN .80 GeV and .98 GeV WERE REMOVED. (Solid line denotes the polynomial fit to the acceptance.)

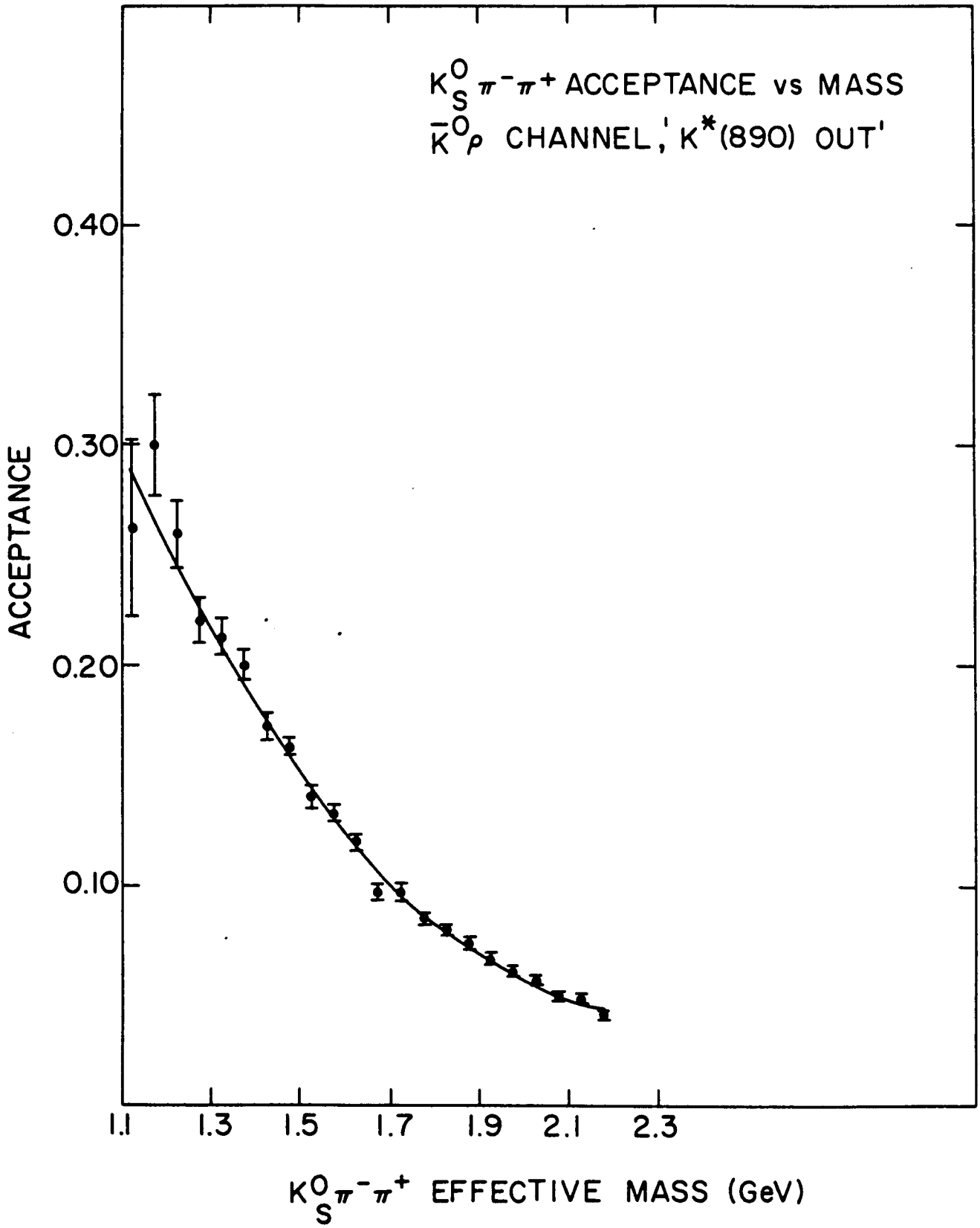
$K^0_S\pi^-\pi^+$ ACCEPTANCE vs MASS
$\bar{K}^0\rho$ CHANNEL, ' $K^*(890)$ OUT'
ACCEPTANCE
0.40
0.30
0.20
0.10
1.1
1.3
1.5
1.7
1.9
2.1
2.3
$K^0_S\pi^-\pi^+$ EFFECTIVE MASS (GeV)

addition to observing a peak in the effective mass spectrum, a complete partial wave analysis is required to understand the situation.

It was very important to determine the acceptance of the apparatus as a function of both the geometric and kinematic variables to see if the integrated phase space acceptance indeed represented the situation properly. The method is described in the Appendix in detail. In short the acceptance was expressed as a function of the geometric and the kinematic variables. For each real event a weight was calculated according to the acceptance in that particular kinematic and geometric variables of the event. Hence the weight represented the equivalent number of events for the particular event and was inversely proportional to the acceptance.

The 'final spectrum' was thus obtained by 'scaling up' each individual event by the corresponding weight. The errors were given by the sum of the squares of the weights. The ratio of the unweighted to the weighted spectrum gave an average acceptance. Figure 22a shows the 'acceptance' vs. mass (integrated over all other variables), which clearly reproduced the acceptance vs. mass generated by Monte Carlo only (Fig. 21b).†† Figures 22b and 22c show the same for the '$K^*(890)$ in' and '$K^*(890)$ out' channels, which again reproduced Figs. 21b and 21c respectively.

---

†† The acceptance for the $K^*(890)$ isobaric state (Reaction 2) was used for fitting the total data.

FIG. 22a ACCEPTANCE VS. $K_S^O \pi^- \pi^+$ EFFECTIVE MASS AS OBTAINED FROM 'ACCEPTANCE MOMENTS'

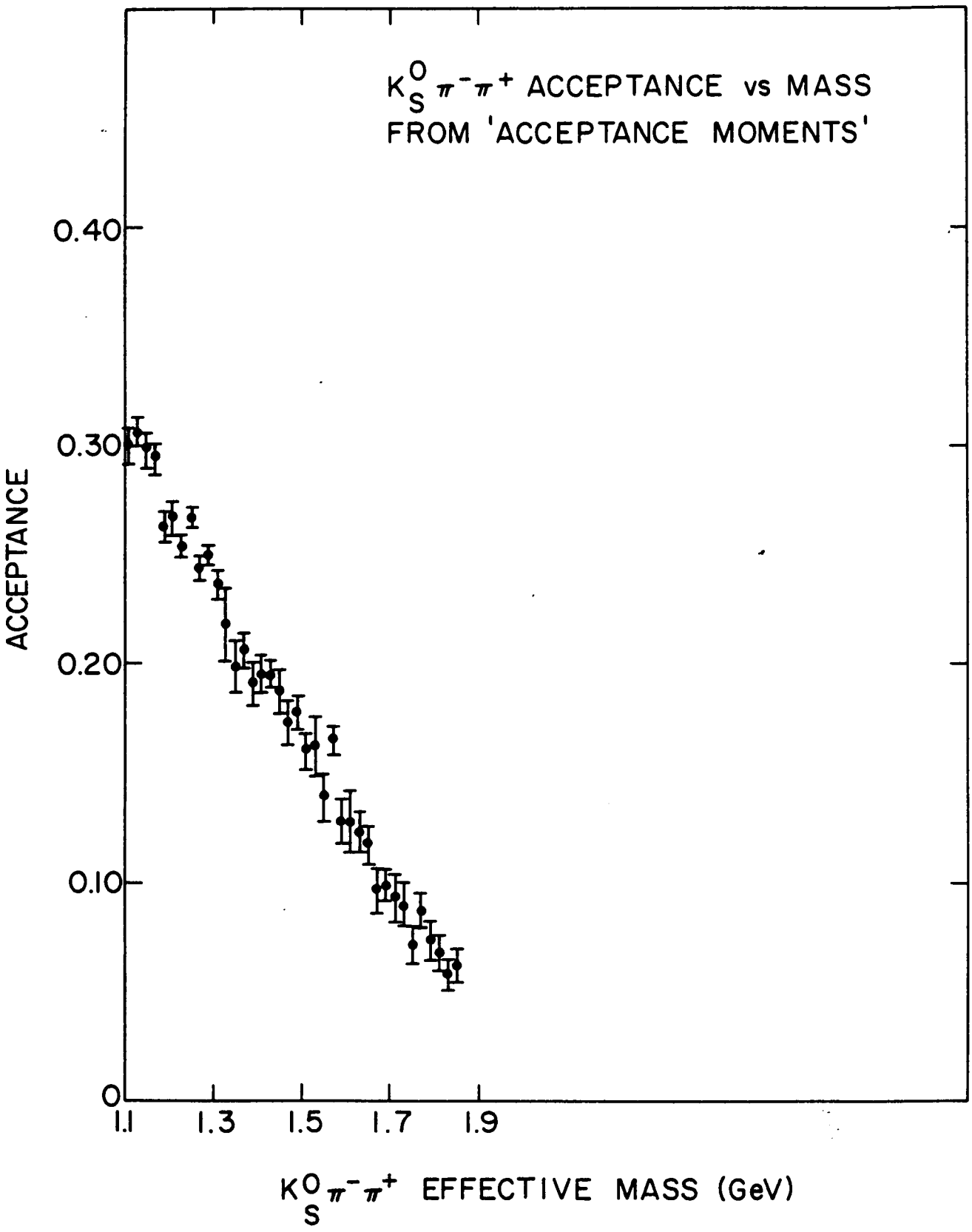
$K^0_S \pi^- \pi^+$ ACCEPTANCE vs MASS
FROM 'ACCEPTANCE MOMENTS'
ACCEPTANCE
0.40
0.30
0.20
0.10
0
1.1
1.3
1.5
1.7
1.9
$K^0_S \pi^- \pi^+$ EFFECTIVE MASS (GeV)

FIG. 22b ACCEPTANCE VS. $K^o_s\pi^-\pi^+$ EFFECTIVE MASS AS OBTAINED FROM 'ACCEPTANCE MOMENTS'. EVENTS WITH $K^o_s\pi^-$ EFFECTIVE MASS IN THE MASS REGION OF .83 GeV TO .95 GeV WERE CONSIDERED.

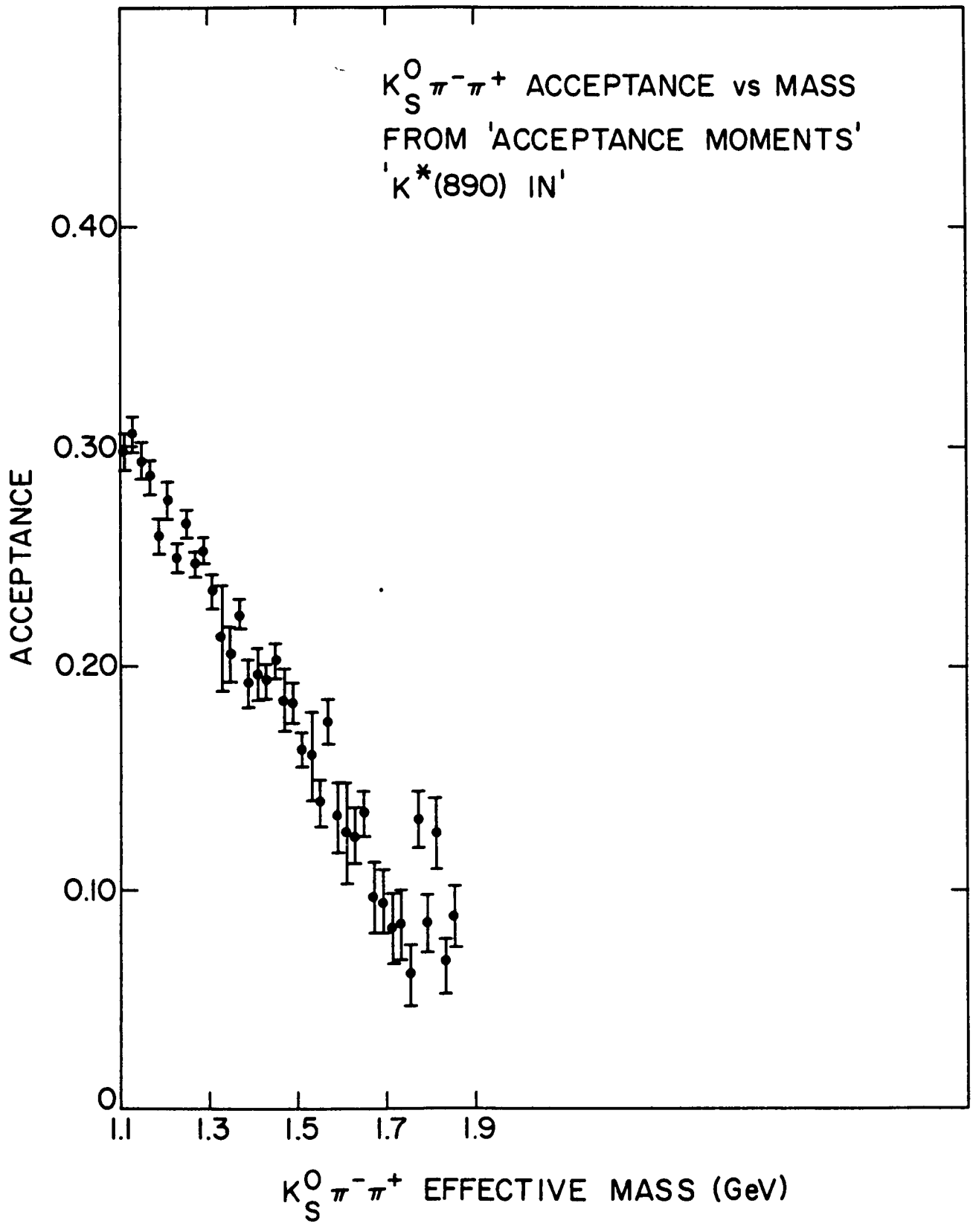
$K^0_S\pi^-\pi^+$ ACCEPTANCE vs MASS
FROM 'ACCEPTANCE MOMENTS'
'$K^*(890)$ IN'
ACCEPTANCE
0.40
0.30
0.20
0.10
0
1.1
1.3
1.5
1.7
1.9
$K^0_S\pi^-\pi^+$ EFFECTIVE MASS (GeV)

FIG. 22c ACCEPTANCE VS. $K_s^o\pi^-\pi^+$ EFFECTIVE MASS AS OBTAINED FROM 'ACCEPTANCE MOMENTS'. EVENTS WITH $K_s^o\pi^-$ EFFECTIVE MASS IN THE MASS RANGE OF .80 GeV TO .98 GeV WERE REMOVED.

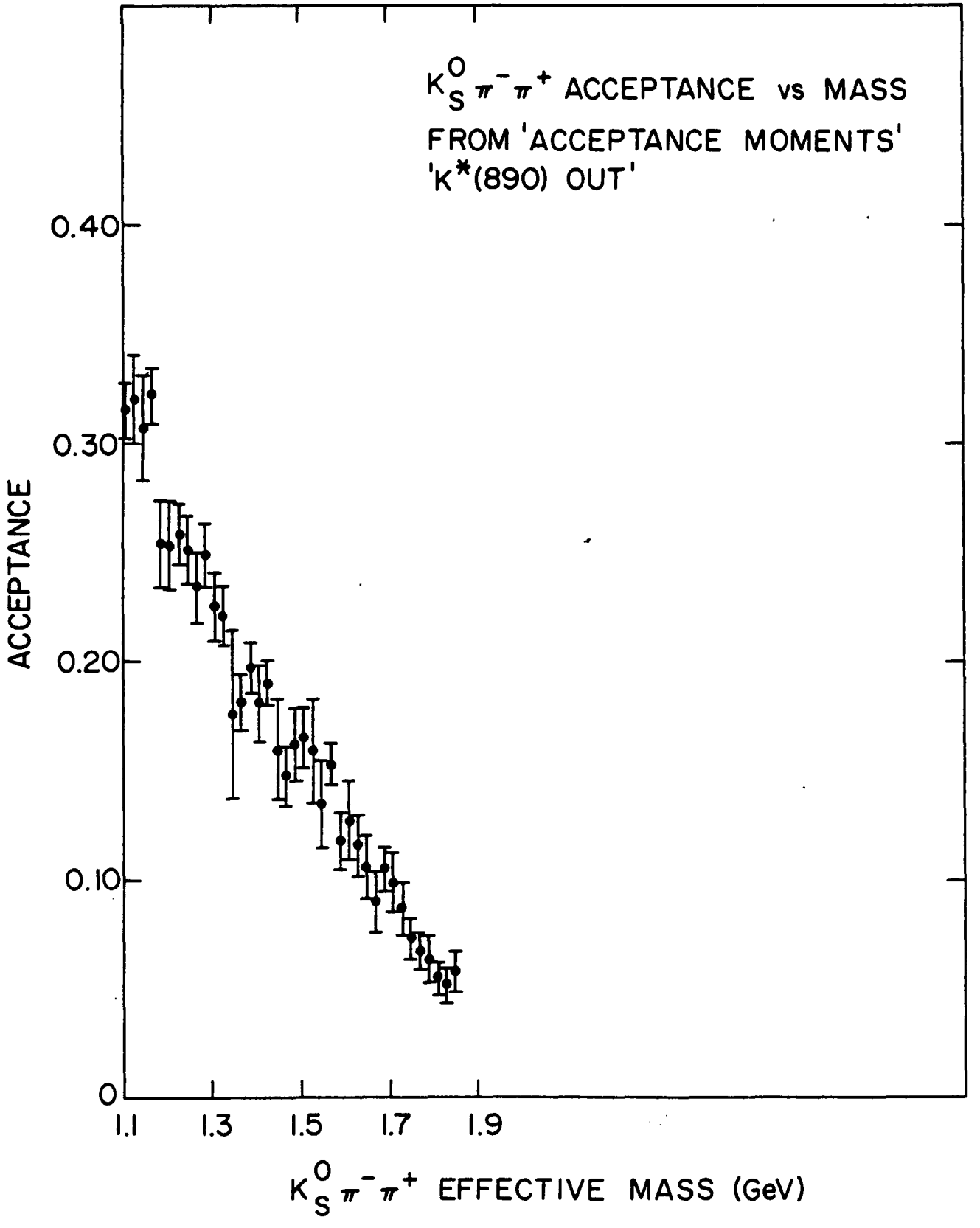
$K^0_S \pi^- \pi^+$ ACCEPTANCE vs MASS
FROM 'ACCEPTANCE MOMENTS'
'K*(890) OUT'
ACCEPTANCE
0.40
0.30
0.20
0.10
0
1.1
1.3
1.5
1.7
1.9
$K^0_S \pi^- \pi^+$ EFFECTIVE MASS (GeV)

Hence, to a first order approximation the shape of the acceptance generated by the acceptance moments taking all the kinematic and geometric variables into account is identical to that generated directly from the phase space Monte Carlo as a function of the effective mass. Therefore the latter acceptance was used for the analysis of the data.

5. Maximum Likelihood Fit to the Mass Spectra

The CERN maximum likelihood fit "Minuit" was used to fit the data sample as shown in Figs. 23a, b, c and d. The appropriate acceptances were used. The results of the fits are shown in Tables 16a, b, c and d. Fit to the total data was done using the $K^*\pi$ acceptance since, as seen from Figs. 21a and 21b, the $K_s^o\pi^-\pi^+$ acceptances with and without the $K^*(890)$ intermediate state are very similar, and as far as $K^*(1420)$ is concerned, it predominantly decays through $K^*(890)$ isobaric state.

The fits were done with one (or two) s-wave Breit-Wigner(s) with a cubic polynomial background. The mass and the width of the Breit-Wigners (in most cases), their amplitudes and the coefficients of the cubic background were left as variable parameters. The resolution was fixed at 15 MeV.†

Total Spectrum:

From the fit to the total data with one s-wave Breit-Wigner, the χ^2 was $\sim$ 95 for 68 bins (61 degrees of freedom). A contribution of 22 in the χ^2 was from the mass region of 1.645 GeV to 1.825 GeV. By counting the excess number of events over the fitted poly-

† The resolution was obtained by generating Monte Carlo events and analyzing them with the processing program. The FWHM of the difference in the $\bar{K}^o\pi^-\pi^+$ effective mass generated by the Monte Carlo and that found and obtained by the processing program was $\sim$ 15 MeV. The procedure is explained in Chapter VI in the determination of the program efficiency.

FIG. 23a MAXIMUM LIKELIHOOD FIT TO THE $K_S^o \pi^- \pi^+$ EFFECTIVE MASS SPECTRUM FROM THE 'TOTAL DATA' SAMPLE (CONSTRAINED). TWO BREIT-WIGNER SHAPES AND A CUBIC POLYNOMIAL AS BACKGROUND WERE USED FOR THE FIT.

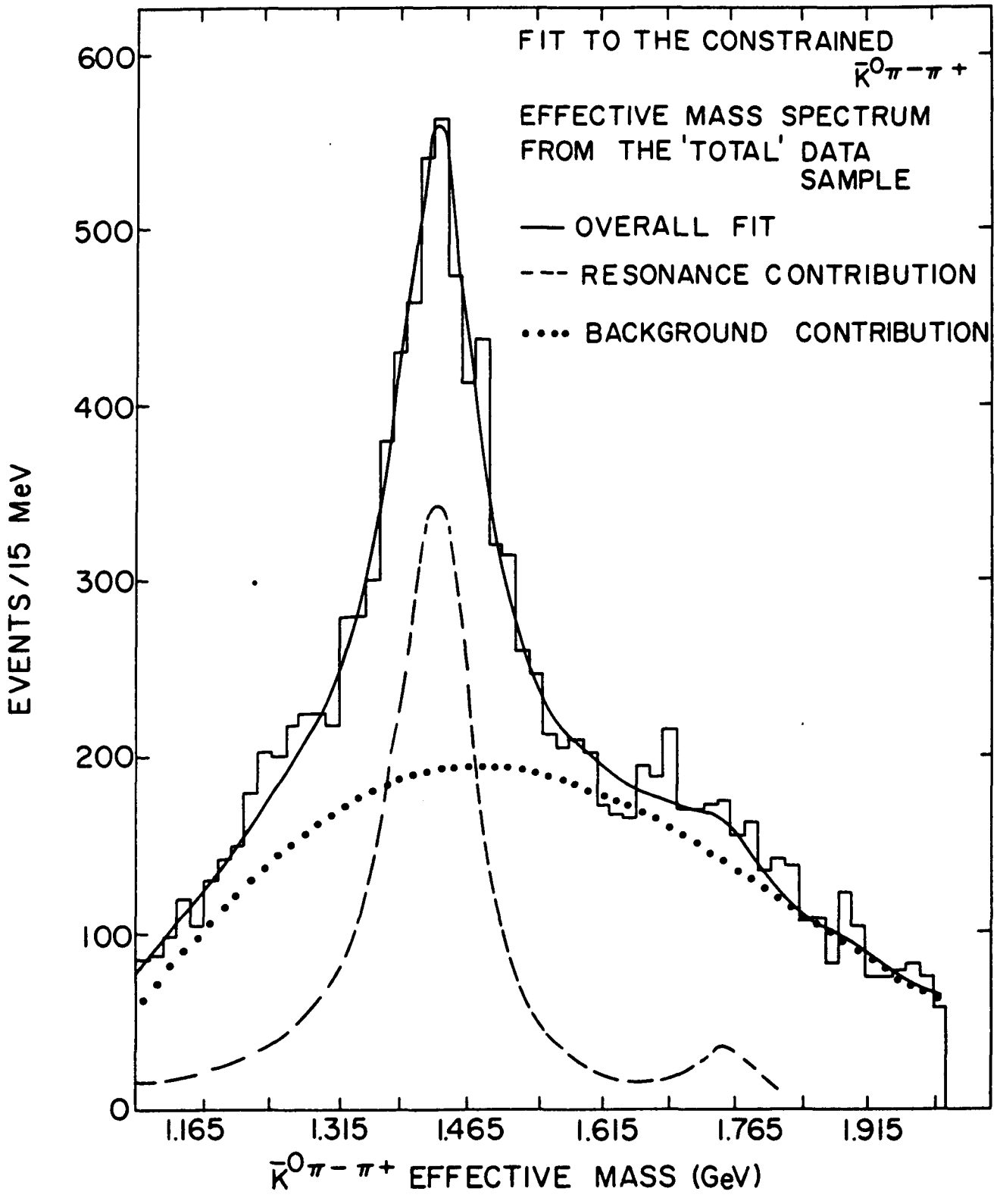
FIT TO THE CONSTRAINED
$\bar{K}^0\pi^-\pi^+$
EFFECTIVE MASS SPECTRUM
FROM THE 'TOTAL' DATA
SAMPLE
— OVERALL FIT
--- RESONANCE CONTRIBUTION
•••• BACKGROUND CONTRIBUTION
EVENTS/15 MeV
0
100
200
300
400
500
600
1.165
1.315
1.465
1.615
1.765
1.915
$\bar{K}^0\pi^-\pi^+$ EFFECTIVE MASS (GeV)

FIG. 23b MAXIMUM LIKELIHOOD FIT TO THE $K^o_s\pi^-\pi^+$ EFFECTIVE MASS SPECTRUM FROM THE 'K*(890) IN' DATA SAMPLE (CONSTRAINED) USING TWO BREIT-WIGNER SHAPES AND A CUBIC POLYNOMIAL. (EVENTS WITH $K^o_s\pi^-$ EFFECTIVE MASS IN THE MASS REGION OF .83 GeV TO .95 GeV WERE IN THIS SPECTRUM.)

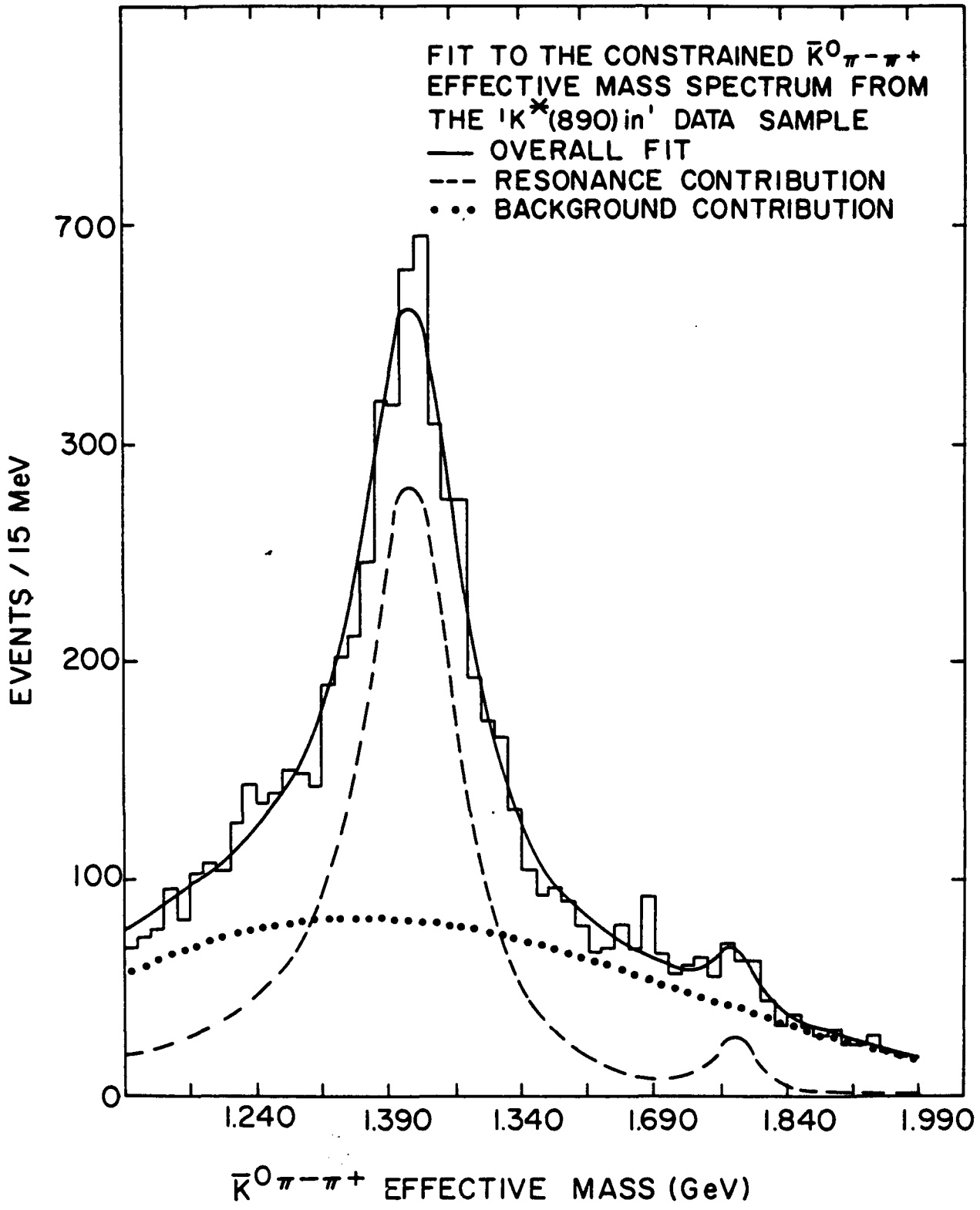
FIT TO THE CONSTRAINED $\bar{K}^0\pi^-\pi^+$ EFFECTIVE MASS SPECTRUM FROM THE $'K^*(890)in'$ DATA SAMPLE
OVERALL FIT
RESONANCE CONTRIBUTION
BACKGROUND CONTRIBUTION
EVENTS / 15 MeV
700
300
200
100
0
1.240
1.390
1.340
1.690
1.840
1.990
$\bar{K}^0\pi^-\pi^+$ EFFECTIVE MASS (GeV)

FIG. 23c MAXIMUM LIKELIHOOD FIT TO THE $K_S^o \pi^- \pi^+$ EFFECTIVE MASS SPECTRUM FROM THE 'K*(890) OUT' DATA SAMPLE (CONSTRAINED) USING TWO BREIT-WIGNER SHAPES AND A CUBIC POLYNOMIAL. (EVENTS WITH $K_S^o \pi^-$ EFFECTIVE MASS IN THE MASS REGION OF .80 GeV TO .98 GeV WERE EXCLUDED.)

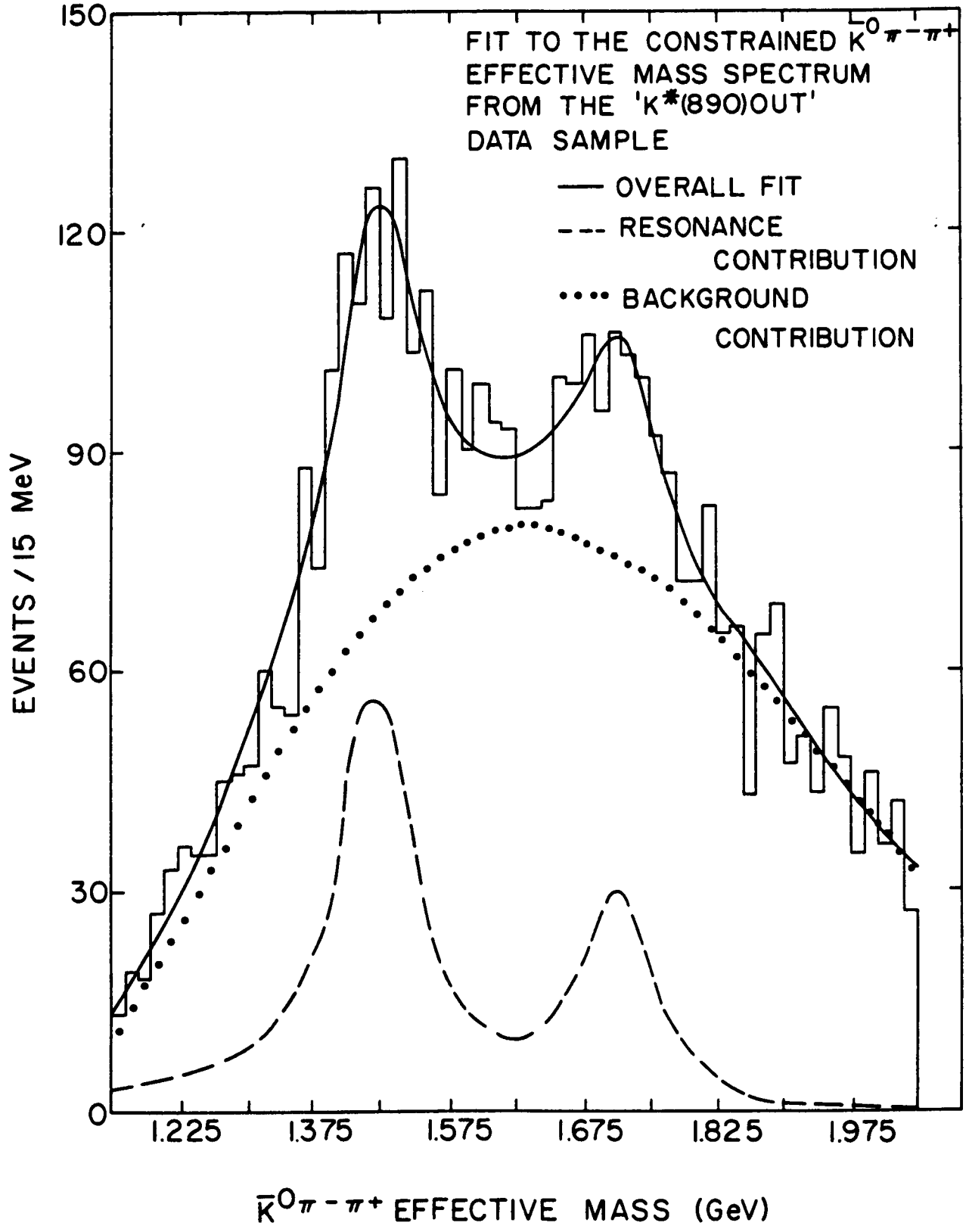
FIT TO THE CONSTRAINED $\bar{K}^0\pi^-\pi^+$ EFFECTIVE MASS SPECTRUM FROM THE 'K*(890)OUT' DATA SAMPLE
OVERALL FIT
RESONANCE CONTRIBUTION
BACKGROUND CONTRIBUTION
EVENTS / 15 MeV
0
30
60
90
120
150
1.225
1.375
1.575
1.675
1.825
1.975
$\bar{K}^0\pi^-\pi^+$ EFFECTIVE MASS (GeV)

FIG. 23d MAXIMUM LIKELIHOOD FIT TO THE $K^{o}_{S}\pi^{-}\pi^{+}$ EFFECTIVE MASS SPECTRUM FROM THE $\bar{K}^{o}\rho$ (AND '$K^{*}(890)$ OUT') DATA SAMPLE (CONSTRAINED). TWO BREIT-WIGNER SHAPES AND A CUBIC POLYNOMIAL WERE USED FOR THE FIT.

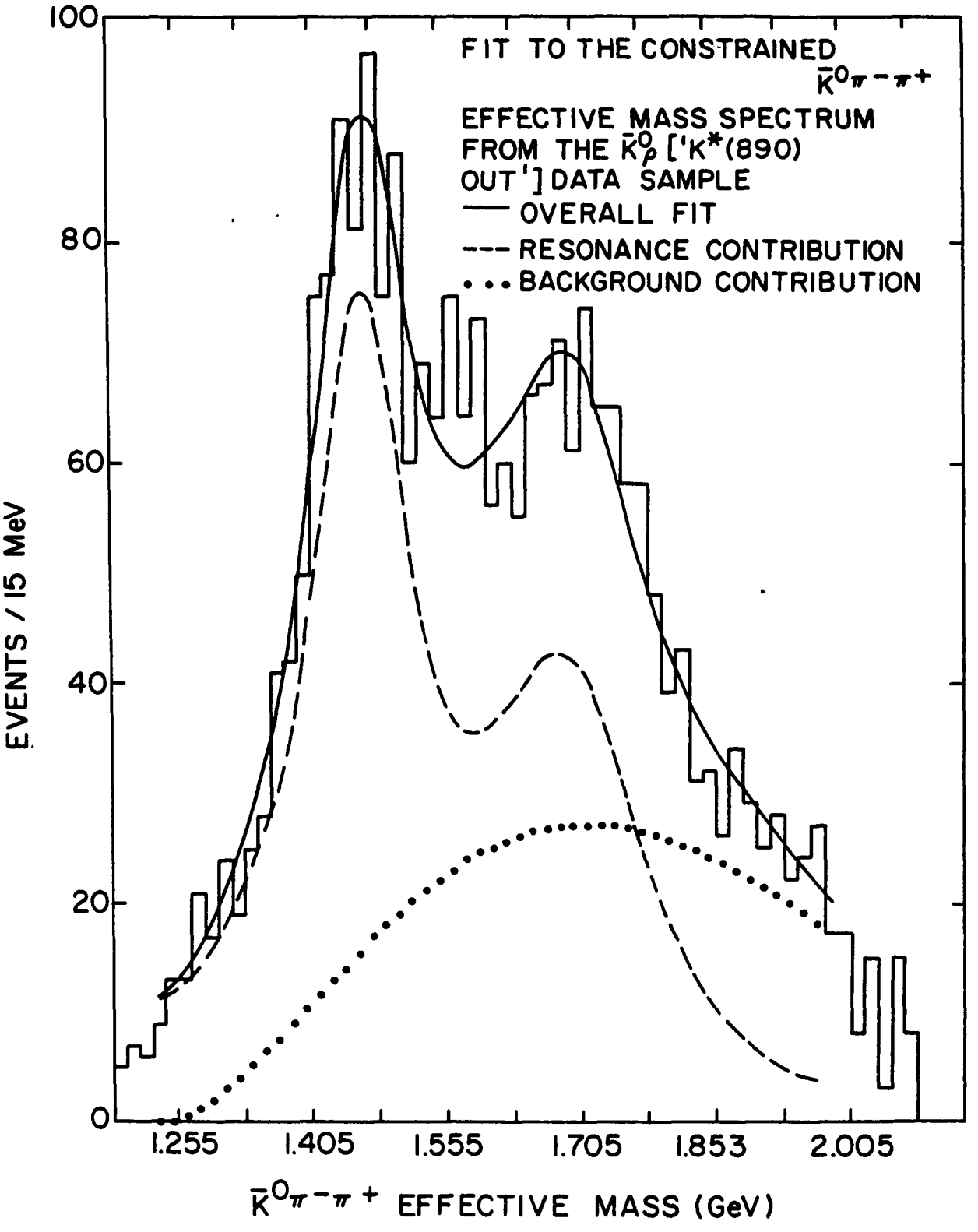
FIT TO THE CONSTRAINED
$\bar{K}^0\pi^-\pi^+$
EFFECTIVE MASS SPECTRUM
FROM THE $\bar{K}^0_\rho$ ['K*(890)
OUT'] DATA SAMPLE
OVERALL FIT
RESONANCE CONTRIBUTION
BACKGROUND CONTRIBUTION
EVENTS / 15 MeV
0
20
40
60
80
100
1.255
1.405
1.555
1.705
1.853
2.005
$\bar{K}^0\pi^-\pi^+$ EFFECTIVE MASS (GeV)

TABLE 16a

Results of Fits to the Total Data

Mass range fitted in GeV	$x^2/\Delta F$	Parameters Mass (MeV) $\Gamma/2$(MeV)	Number of acceptance corrected events in the resonance	Comments
1 resonance fit; 1.09 - 2.10	94.7/61	1426 ± 2 46 ± 3	18492.9	A 3.7σ effect between 1.645 and 1.825 GeV.
1 resonance fit; 1.09 - 2.10 1.645 to 1.825 excluded from the fit	58.8/49	1427.8 ± 2 54 ± 4	21861.3	A 8.1σ effect between 1.624 and 1.825 GeV
2 resonance fit; 1.09 - 2.10	81.2/58	1426 ± 2 50.0 ± 3 1746 ± 15 57 ± 16	20277.1 3064.7	

15 MeV bin size; resolution fixed at 15 MeV; a cubic polynomial used for the background with its coefficients left as free parameters; K*(890) π acceptance used.

Table 16b

Results of Fits to the 'K(890) in' Data

Mass range fitted in GeV	$x^2/\Delta F$	Parameters Mass MeV $\Gamma/2$ MeV	Number of acceptance corrected events in the resonance	Comments
1 resonance fit; 1.09 - 2.10	95.7/61	1422 ± 2 56 ± 4	17560.4	A 3.7σ effect between 1.735 and 1.810 GeV
1 resonance fit; 1.09 - 2.10 1.735 to 1.81 excluded from the fit	71.3/56	1423 ± 2 59.6 ± 2	18611.3	A 4.9σ effect between 1.735 and 1.810 GeV
2 resonance fit; 1.09 - 2.10	76.7/59	1423 63.6 ± 0 $1782^{+7}_{-8.5}$ 15.8^{+18}_{-14}	19479.7 1497.9	

15 MeV bin size; resolution fixed at 15 MeV; a cubic polynomial used for the background with its coefficients left as free parameters.

Table 16c

Results of Fits to the 'K(890) out' Data

Mass range fitted in GeV	$x^2/\Delta F$	Parameters Mass (MeV) $\Gamma/2$ (MeV)	Number of acceptance corrected events in the resonance	Comments
1 resonance fit 1.105 - 2.10	68.6/60	1444 ± 7 34 ± 10	1970.2	A3.5σ effect between 1.645 and 1.78 GeV
1 resonance fit 1.105 - 2.10 1.645 to 1.795 excluded from the fit	47.7/50	1447 ± 3 42 ± 7	2670.4	A 5.3σ effect between 1.645 and 1.795 GeV
2 resonance fit 1.105 -2.10	50.0/57	1449 ± 6 51 ± 9 1722 ± 11 46 ± 20	3296.0 2787.9	

15 MeV bin size; resolution fixed at 15 MeV; a cubic polynomial used for the background with its coefficients left as free parameters.

Table 16d

Results of Fit to the 'K(890) out', $K^{o}_{s}\rho$ Data

Mass range fitted in GeV	$x^2/\Delta F$	Parameters Mass (MeV) $\Gamma/2$ (MeV)	Number of acceptance corrected events in the resonance	Comments
2 resonance fit; 1.225-1.975	32.6/40	1466 ± 8 62 ± 16 1701 ± 13 109 ± 31	4741.3 7088.7	

15 MeV bin size; resolution fixed at 15 MeV; a cubic polynomial used for the background with its coefficients left as free parameters.

nomial background, this represented a 3.7 standard deviations (σ) effect. The errors quoted on the value of the mass and the width were obtained from the error matrix of the maximum likelihood program 'MINUIT'. Leaving out the bins between 1.645 and 1.825 GeV from the fit gave us a χ^2 of 58.5 for 54 bins. This gave a $> 8\sigma$ effect between 1.645 and 1.825 GeV and the resonance parameters of the '1420' peak as

$$M = 1427.3 \pm 2 \text{ MeV}; \quad \Gamma/2 = 54.4 \pm 3.7 \text{ MeV}.$$

A fit with two Breit-Wigners gave a χ^2 of 81.2 for 58 bins (58 degrees of freedom). The parameters of the resonances were

$$M_1 = 1426 \pm 2 \text{ MeV}; \quad \Gamma_1/2 = 50 \pm 3 \text{ MeV}$$

$$M_2 = 1746 \pm 15 \text{ MeV}; \quad \Gamma_2/2 = 57 \pm 16 \text{ MeV}.$$

The ratio of the two Breit-Wigner amplitudes were BW1/BW2 = 2.2/0.3. The fitted spectrum is shown in Fig. 23a.

'$K^*(890)$ in' Spectrum:

To investigate the nature of the spectrum in more detail we looked at the fits with the '$K^*(890)$ in' spectrum. With only one Breit-Wigner the χ^2 for the fit was $\sim$ 96 for 68 bins (61 degrees of freedom) with a contribution of 19 from five bins in the region of 1.735 to 1.81 GeV. This corresponded to a 3.7σ effect calculated by counting excess events over background. Leaving those bins off from the fit resulted in a χ^2 of 74 for 56 degrees of freedom, the mass and the width for the 1420 peak as

$$M = 1423 \pm 2 \text{ MeV}; \quad \Gamma/2 = 60 \pm 2 \text{ MeV},$$

and a 4.9σ effect in the mass region mentioned. Trying to fit the spectrum with two Breit-Wigners (Fig. 23b) the mass of the 1420 peak was fixed at 1423 and the parameters were

$M_1 = 1423$ MeV; $\Gamma_1/2 = 64 \pm 0$ MeV

$M_2 = 1782^{+7}_{-9}$ MeV; $\Gamma_2/2 = 16^{+18}_{-14}$ MeV.

The ratio of the amplitudes of the two Breit-Wigners was 6.9/.5. Table 16b lists the results of the fits.

'$K^*(890)$ out' Spectrum:

The fit to the '$K^*(890)$ out' spectrum with one Breit-Wigner gave a χ^2 of 68.6 for 67 bins (60 degrees of freedom) of which a χ^2 of 11 was contributed from 1.645 to 1.78 GeV. Counting excess events over background this was a 3.5σ effect. Leaving out the bins between 1.645 and 1.795 GeV from the fit gave a χ^2 of 47.7 for 50 degrees of freedom. A 5.3σ effect was obtained from the excess events over background in this mass region. The mass and the width of the 1420 peak were

$M = 1447$ MeV; $\Gamma/2 = 42$ MeV.

Trying to fit the spectrum with two Breit-Wigners (Fig. 23c) gave a χ^2 of 50; the masses and the widths were

$M_1 = 1449 \pm 6$ MeV; $\Gamma_1/2 = 51 \pm 9$ MeV

$M_2 = 1722 \pm 11$ MeV; $\Gamma_2/2 = 46 \pm 20$ MeV

and the ratio of the amplitudes BW1/BW2 = .98/.82. Table 16c lists the results of the fits.

'$K^*(890)$ out' and $K\rho$ Spectrum:

As shown in Fig. 19, statistics were limited in this spectrum compared to the others fitted earlier. Trying to fit the spectrum with two Breit-Wigners (Fig. 23d) gave a χ^2 of 32.6 for 50 bins (40 degrees of freedom) and the masses and the widths as follows:

$M_1 = 1466 \pm 8$ MeV; $\Gamma_1/2 = 62 \pm 16$ MeV

$M_2 = 1701 \pm 13$ MeV; $\Gamma_2/2 = 109 \pm 31$ MeV.

The ratio of the two Breit-Wigner amplitudes were BW1/BW2 = .80/1.30. The results of the fit are listed in Table 16d.

Discussion:

The nature of the 1420 peak is very different in each of the spectra. However, in view of the current knowledge of the K^* spectroscopy (Table 1) it is understandable since the '1420' peak is believed to be a composite structure of a 0^- ($M = 1404 \pm 15$; $\Gamma = 230 \pm 20$), a 0^+ ($M = 1425 \pm 50$; $\Gamma = 250 \pm 50$), and the 2^+ ($M = 1434 \pm 7$; $\Gamma = 100$ 4) (Ref. 1). The '$K^*(890)$ in' channel mainly excludes the $0^+(1425)$ and has the $0^-(1400)$ and the $2^+(1435)$. In addition any non-diffractively produced $Q_2(1400)$ would also be present in this channel (Ref. 7) according to its reported decay modes shown in Table 1. The peak in the '$K^*(890)$ out' spectrum in comparison is shifted towards the higher mass due to the presence of $2^+(1435)$. Due to the complexity of the K^* spectroscopy, a Partial Wave Analysis (PWA) is necessary to understand the situation in detail. We plan to begin a PWA of this data in the near future in the process of which we also expect to obtain the decay branching ratios of the $K^*(1420)$ [and possibly of other K^*'s as well].

The situation is fairly similar in the 1700-1800 MeV region. We see a wide peak ($\Gamma = 119$ MeV) at $\sim$ 1750 MeV in the total spectrum. However, in the '$K^*(890)$ in' spectrum there is some evidence of the established $3^-(1780)$ (Refs. 7, 18, 19), the width is narrower[†] than the reported value $\sim$ 135 MeV, but considering the statistics of the data it is not surprising. Yet when we look at the '$K^*(890)$ out' spectrum there is at least one resonant-like peak apparent around 1720 MeV with

---

[†] $\Gamma = 32^{+36}_{-28}$ MeV from Table 16b

$\sim$ 90 MeV width. Quite possibly there is more than one resonance in the mass region of 1700-1800 MeV. To understand the situation definitively, one has to resort to a partial wave analysis of the data with more statistics.

6. t-Dependence of the Data in the 1420 Region:

The total $K_s^o\pi^-\pi^+$ final data sample in the mass region between 1.165 and 1.99 GeV was divided into t-bins as shown in Table 17. For each of the t-bins the acceptance as a function of mass was calculated in a way similar to that described earlier. In each case a quadratic function represented the acceptance as a function of mass adequately (as determined by the least squared fit of the acceptance). The mass spectrum in each t-interval was fitted to a Breit-Wigner form and background. The mass and the width of the Breit-Wigner shape were fixed at 1427 and 108 MeV respectively (as obtained from the fit to the total data sample - Table 16a). A cubic polynomial was used in the fit to represent the background. In order to avoid the influence from the bump in the 1750 MeV region in the mass spectrum the mass region between 1645 and 1840 MeV was excluded from the fit (as was done earlier to obtain the parameters for the 1420 Breit-Wigner from the fit to the total data). Table 17 lists the results from the fits. The errors listed in Table 17 include the statistical errors of the events under the Breit-Wigner shape and the error in the acceptance determination added in quadrature. To check how dependent the results of the fits were to the shape of the background a quadratic and a fourth order polynomial were used for the background shape. The quadratic

Table 17

DISTRIBUTION OF EVENTS IN THE '1420' PEAK IN VARIOUS $|t'|$ RANGES

t' range	x^2 for 36 DF	average acceptance	Number of acceptance corrected events in the resonance κ	percentage error on N	ΔN
0.00 - 0.025	37.9	.273	2877.1	9.2%	$\pm$264.7
0.025 - 0.05	31	.270	2354.4	10.6%	$\pm$249.6
0.05 - 0.075	45.9	.278	1897.9	11.2%	$\pm$212.6
0.075 - 0.10	41.6	.272	1382.4	13%	$\pm$179.7
0.10 - 0.15	40	.270	2032.8	10.5%	$\pm$213.4
0.15 - 0.20	30.9	.252	2060	11.2%	$\pm$230.7
0.20 - 0.25	36.2	.241	1344.7	14.2%	$\pm$191
0.25 - 0.30	33.4	.244	978.9	16%	$\pm$156.6
0.30 - 0.40	22.1	.240	1646.8	11.4%	$\pm$187.7
0.40 - 0.50	43.9	.211	963.4	17%	$\pm$163.8
0.50 - 0.60	37.3	.225	502.5	24.1%	$\pm$121.1
0.60 - 0.80	36.8	.204	819.6	18.3%	$\pm$150
0.80 - 1.00	53.8	.179	848.8	18.1%	$\pm$153.6

background gave a much poorer fit and the fourth order polynomial background did not change the result by more than 5%.

Figure 24 shows the dn/dt plot vs. $|t'|$. A least squared fit to the curve was done over various $|t'|$ ranges according to Exp(bt') for the best value of b. Table 18 lists the value of the slope b and the χ^2 for each fit. Three things are apparent from the table:

i. The value of the slope b is very dependent on the t' range fitted. In the small $|t'|$ region ($|t'| < 0.15$) the average slope is 9.44, then it tends to flatten out to 4.6 or so as seen from the results of the fits in the relatively higher $|t'|$ region. This is perhaps suggestive of two different slopes and is consistent with the idea of more than one particle exchange being involved in the production mechanism. At low $|t'|$ the unnatural parity exchange (pion exchange) is the dominant process in the production mechanism, as opposed to the natural parity exchange (ρ,ω) which becomes dominant at higher $|t'|$ and manifests itself in a relatively flatter slope than that due to the pion exchange.

ii. A reasonable χ^2 is obtained as long as the last data point between $|t'|$ of 0.8 and 1.0 is not included in the fit. The χ^2 takes a big jump for the inclusion of this one data point, as seen from the fit results from various t' ranges. This may be indicative of a further flattening of the slope.

iii. No forward dip is apparent showing the absence of a major spin-flip amplitude. The total number of acceptance folded events under

FIG. 24 PLOT OF THE NUMBER OF ACCEPTANCE CORRECTED EVENTS VS. $|t'|$ IN THE '1420' PEAK. EVENTS IN EACH $|t'|$ RANGE WERE FITTED USING A BREIT-WIGNER SHAPE FOR THE '1420' PEAK AND A CUBIC POLYNOMIAL FOR THE BACKGROUND. TO AVOID ANY EFFECT FROM THE '1750' REGION, THE MASS REGION BETWEEN 1.645 GeV AND 1.840 GeV WAS EXCLUDED FROM THE FITS.

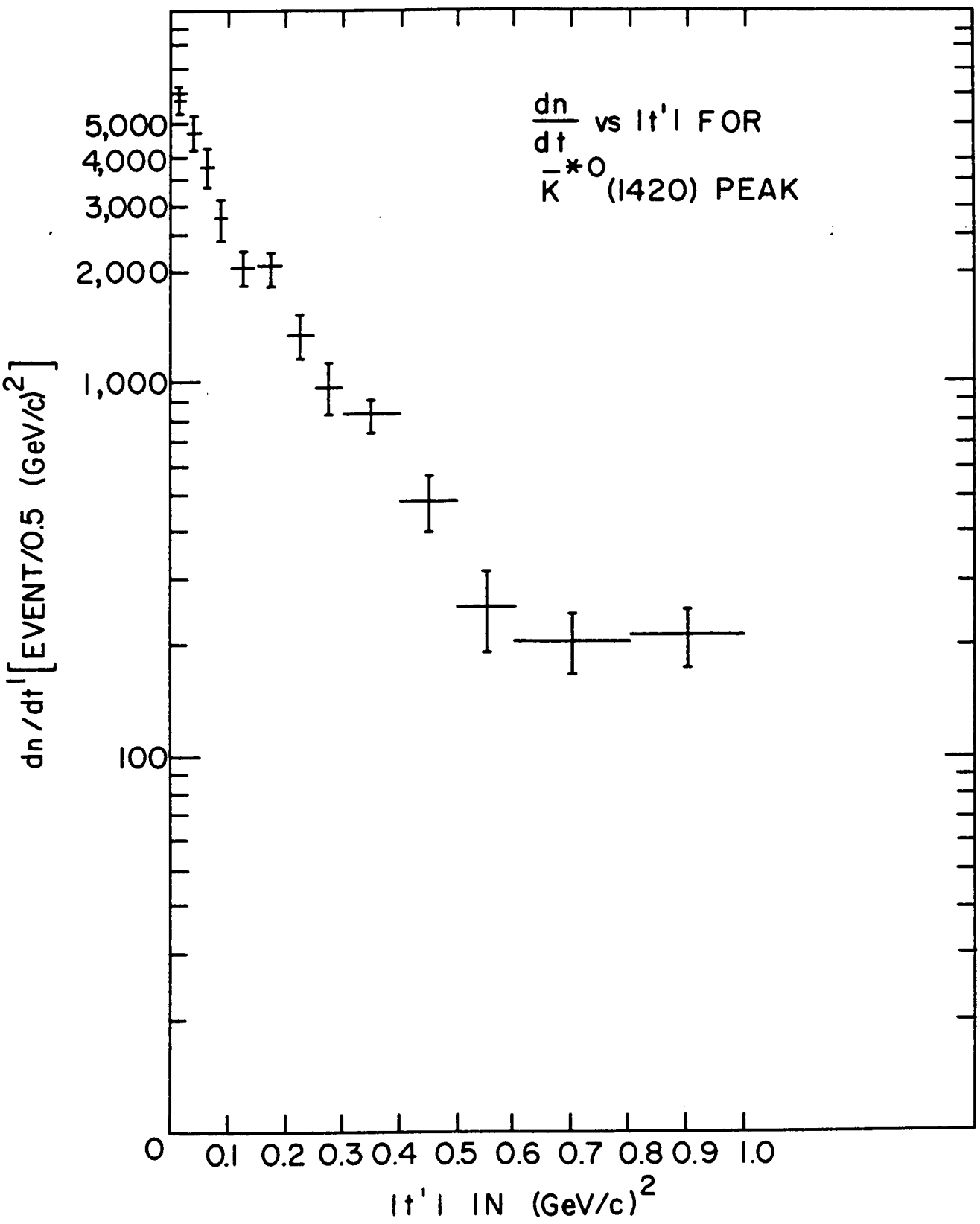
dn/dt vs |t'| FOR
K̄*0(1420) PEAK
dn/dt'[EVENT/0.5 (GeV/c)²]
5,000
4,000
3,000
2,000
1,000
100
0
0.1 0.2 0.3 0.4 0.5 0.6 0.7 0.8 0.9 1.0
|t'| IN (GeV/c)²

TABLE 18

Results of fits to the dn/dt' vs. t' plot

|t'| Range of Fit		Number of data points	Value of b	χ^2
Initial Data Point	Final Data Point			
0.00	0.10	4	9.41	.25
	0.15	5	9.47	.25
	0.20	6	7.24	6.28
	0.25	7	7.24	7.05
	0.30	8	6.70	7.27
	0.60	11	6.00	13.32
	0.80	12	5.30	17.32
	1.00	13	4.70	35.92
0.075	0.30	5	5.00	2.63
	0.60	8	4.87	3.39
	0.80	9	4.55	4.94
	1.00	10	3.91	17.17
0.30	0.60	3	5.81	.06
	0.80	4	4.30	2.04
	1.00	5	2.88	9.76

the dn/dt curve was obtained by adding up the contribution from each t' bin up to t' of 1.0 and then evaluating the integral.†

$$\int_{1}^{\infty} e^{bt'}\, dt'$$

The value of b used was 5.3. The normalized value of the integral was obtained by evaluating the area between 0 and 1 to be the total number of events, i.e.

$$\int_{0}^{1} e^{bt'}\, dt'$$

equals the total number of events between $|t'|$ of 0.0 and 1.0. The contribution of the integral between $|t'|$ of 1.0 and ∞ is approximately 0.5% of that of the total number of events.

---

† To be precise, the total number of events should be obtained by evaluating the integral up to t'_{max} instead of up to ∞. However, the contribution of the integral between t'_{max} and ∞ is negligible compared to the other errors involved.

CHAPTER VI

TOTAL AND DIFFERENTIAL CROSS SECTIONS

The product of the total cross section and the branching ratio was calculated using the formula

$$\sigma \cdot Br = \frac{N}{\rho \times N_o \times L \times \varepsilon \times A^{-1} \times Beam} = \alpha \frac{N}{Beam_{eff}}$$

where $\sigma \equiv$ total cross section,

$Br \equiv$ Branching ratio for the decay channel investigated,

$N \equiv$ observed events (acceptance corrected) of $K^- p \rightarrow K^o_s \pi^+ \pi^- + n$,

$\rho \equiv$ density of liquid hydrogen = .0708 gm/cm^3,

$A \equiv$ Atomic weight of hydrogen = 1.01,

$N_o \equiv$ Avagadro's number = 6.022045×10^{23} mole^{-1},

$Beam_{eff} \equiv$ total effective K^- beam to produce N events,

$\alpha = 1/\varepsilon \times \rho \times N_o \times L \times A^{-1}$,

$\varepsilon = \varepsilon_{pr} \times \varepsilon_{tr} \times$ (other correction factors),

$\varepsilon_{pr} \equiv$ program efficiency for event,

$\varepsilon_{tr} \equiv$ triggering efficiency of the apparatus,

$L \equiv$ length of the liquid hydrogen target = 50.8 cm.

The following sections describe the way the above factors were derived.

1. Calculation of Total Beam Flux:

The CAMAC scalers contained the information about the total number of beam, triggers etc., for each run as described earlier. The CAMAC scalers as well as the output summary of each processed tape were written out in the special records on the H-tapes. A special bookkeeping program scanned all the special records from the H-tapes

and printed out a summary of all the CAMAC scalers and output summaries of the desired L-tapes. It calculated various ratios and printed them out for each individual run. A consistency check for the runs used in the data was done by observing whether these ratios and numbers agreed with each other within tolerance. The pertinent sums are listed in Table 19. The effective beam flux used in the calculation of the cross section was derived from the total beam obtained from the scaler with corrections described below.

2. Corrections:

a. Beam

i. Failure to determine the incident beam uniquely (GDINC):

The analysis program analyzed an event only when the incident particle was uniquely defined by its position & momentum (defined as good incidents). For instance events with multiple counts in some of the beam PWC's would fail to determine the incident beam uniquely. Therefore the total number of effective incident beam was obtained by scaling the total beam flux by the number of the good incidents (GDINC's) to the number of the total triggered events ratio. Thus the beam flux corrected for the good incidents was expressed as

$$\text{Effective beam}_{\text{GDINC}} = \text{Beam} \times \left(\frac{\text{GDINC}}{\text{Trig}}\right)_{\text{profile}}$$

This ratio was taken for the profile triggers only since the data triggered events had higher multiplicity and therefore could have originated from a biased beam sample.

ii. Overcounting of Scalers:

At the beginning of every data tape the scalers had to be reset and started by someone during the experiment. This introduced

TABLE 19

Calculation of Effective Beam

	Number of runs	Total beam used from Scaler	Ratio of $\frac{\text{GDINC}}{\text{TRIG}}$ for beam	Ratio of $\frac{\text{Program Count}}{\text{Scaler Count}}$ for data trigger	Effective Beam Used
Fall	185	792, 427, 086	.945004	.999763	748.669×10^6
Winter	169	925, 085, 810	.890354	.917721	755.885×10^6

$\therefore$ Total beam for 354 runs = $1{,}504.554 \times 10^6$

a time lag between starting the scalers and the data recording on magnetic tapes. Since the total beam was obtained from the scalers, it had to be corrected by the ratio of the total trigger on magnetic tapes as analyzed by the program to that counted by the scaler.

$$\text{Beam}_{\text{eff}} = \text{Beam} \times \left(\frac{\text{GDINC}}{\text{Trig}}\right)_{\text{profile}} \times \frac{(\text{total data trigger})_{\text{program}}}{(\text{total data trigger})_{\text{scaler}}}$$

iii. Nuclear Attenuation of the K^- Beam in the Target:

The incident K^- beam was attenuated in the liquid hydrogen target by nuclear interaction. The attenuation was determined by the total K^-p inelastic cross section and the path length traversed. The path traversed was close to the full length of the target as observed from the distribution in z of the production vertices. This reduced the effective beam by a factor of $\exp(-n\sigma\chi)$

where $\chi \equiv$ length of the target = 50.8 cm,

$\sigma \equiv$ total K^- inelastic cross section = 20 m.barns,

$n \equiv$ number of scatterers/unit volume,

and $n = N_o \times \rho/A = 422139.3921 \times 10^{17}$,

$\exp(-n\sigma\chi) = .958$.

This correction is listed in Table 20 and was applied in calculating ε along with corrections described in section iv.

iv. Contamination in the Incident Beam:

a) K^- decay in flight:

The incident K^- was identified by the Cerenkov counters CV_2 and CV_3 (Fig. 2) after which it traversed a path length of $\sim$ 800 cm(L) before interacting inside the liquid Hydrogen target. It decayed weakly in the flight, probability of which in between path length ℓ and $\ell + d\ell$ is given by $\exp(-m\ell/pc\tau)$,

TABLE 20

Compilation of Correction Factors

Correction Factors	Contribution to σ	
	in '1420' Region	in '1750' Region
nuclear attenuation of K^- in the target	.958	
decay of incident K^- in Flight	.837	
inefficiency of the cerenkov counter	.985	
program efficiency for event reconstruction	.709	.679
K^o_s branching ratio	.688	
loss due to kinematic cuts	0.730	0.765
ε	.281	.282
α	$.166 \times 10^{-23}$	$.165 \times 10^{-23}$
$\sigma \cdot Br = \frac{\alpha N^*}{Beam}_{eff.}$	$.110 \times 10^{-32} \times N$	$.110 \times 10^{-32} \times N$

*Where N ≡ number of acceptance corrected events in the resonance

where m ≡ mass of K^- = .494 GeV,

p ≡ K^- momentum = 6.0 GeV/c,

$c\tau$ = 370.9,

ℓ = 800 cm.

The fraction of K^- decayed in the total path length L is given by

$$1 - \exp(-mL/pc\tau) = 1 - .837 = .163.$$

b) Detection inefficiency of the beam Cerenkov counters:

The purity of the incident K^- beam used in triggering the system depended on how efficiently the Cerenkov counter CV_2 vetoed the pions. Hence the ratio of the number of real K's to the number of particles registered as K's is given as

$$1 - \rho\varepsilon_{ineff} = .985$$

where $\rho \equiv$ pion flux/kaon flux immediately upstream of CV_2 = 1.5,

$\varepsilon_{ineff} \equiv$ inefficiency of CV_2 = .01.

b. Corrections in the Final Data Sample:

i. π-μ Decay:

The analysis program assumed the four charged particles to be pions and the analysis was performed accordingly. In case a pion decayed into a muon inside the MPS magnetic field, the momentum of the track might not be calculated correctly (depending on how far downstream the pion reached before decaying and the momentum and the direction of the muon it decayed into). The fraction of the pions decaying (for each of the four tracks) is

$$[1 - \exp(-m_\pi L_\pi / p_\pi c\tau)]$$

where $L_\pi \equiv$ path length traversed by the pion.

For an average p_π of 1.0 GeV and L_π of $\sim$ 100 cm, this was found to be $\sim$ 1.5% and was not taken into account.

ii. Program Efficiency:

The event reconstruction efficiency of the analysis program directly affected the total number of events found and thus the cross section calculation. The following procedure was used to determine this efficiency ε_{pr} in two $K^o_s\pi^-\pi^+$ effective mass regions. Results are listed in Table 21.

The Monte Carlo program described earlier was used to generate events and swim them through the MPS magnet. The coordinates and the origins of the chambers were input to the program. The coordinates where the tracks intersected the chambers were written out on a disk file for the accepted events. This file was read by the analysis program (instead of a data tape) on an event-by-event basis with a flag indicating these to be Monte Carlo events. A special unpacking was done and the 'ideal' spark positions were distorted by spreading them over a gaussian of the width of the chamber resolution. Two spark positions if less than 0.6 cm apart were merged into one (as was observed with the data). The sparks were 'detected' according to the chamber efficiencies supplied to the program. From there on pattern recognition and further analysis identical to that of the data was done. The ratio of the number of reconstructed events to that generated was a direct measure of the program efficiency.

The above procedure gave an optimistic estimate of the program efficiency since no background was included. A second estimate was obtained by mixing the Monte Carlo 'sparks' with real sparks from

Table 21

Program Efficiency Determination

Mass region	Number of events generated	Number of events reconstructed	Efficiency
1.420	3025	2467 without background	.816
		1821 with background	.602
1.750	1799	1464 without background	.814
		978 with background	.544

a profile tape prior to pattern recognition. The results of both are listed in Table 21. The average of the two estimates was used as the program efficiency and is listed in Table 20.

iii. Trigger Efficiency:

This was dependent mainly on the TPX efficiencies; the efficiency of TPX1 for two or more clusters and that of TPX2 for four or more clusters. Table 22 lists the results. However, the dead regions and the low efficiency regions of the TPX's were taken into account in the Monte Carlo program for acceptance calculation and therefore was not corrected for in the cross section calculation.

iv. K^o_s Branching Ratios:

Since only the charged decay mode of the K^o_s was observed the number of events had to be corrected for the neutral decay mode as listed in Table 20.

v. Kinematic Cuts:

Table 14 in Chapter V listed the cuts (i, ii, iii, iv, and v) to select the final data sample. The amount of signal lost due to each of these cuts was estimated the following way:

The $K^o_s\pi^-\pi^+$ effective mass spectrum for the events outside the $\pm 2\sigma$ limit of the particular cut was investigated while other cuts were left identical to those of the data. The amount of signals over background was estimated in both the 1420 and the 1750 mass regions. In case of sufficient statistics a maximum likelihood fit to the spectrum was performed by using i) a cubic polynomial for just a background and ii) the combination of a Breit-Wigner in the 1420 region

Table 22

TPX1 and TPX2 Efficiency Determination

	Fall		Winter		Average
	Single Cluster Efficiency	Multiple Cluster Efficiency	Single Cluster Efficiency	Multiple Cluster Efficiency	Multiple Cluster Efficiency
TPX1	.966	.933 for 2 cluster	.893	.797 for 2 cluster	.865
TPX2	.976	.907 for 4 cluster	.938	.774 for 4 cluster	.841

$\therefore$ average trigger efficiency = .865 x .841

= .728

and a cubic polynomial. Table 23 lists the results. The $\Delta z/\delta z$ cut listed in Table 14 was taken into account in the acceptance calculation and hence was not considered in the list in Table 23. The fraction of data lost due to each kinematic cut was independent of the others to a first approximation. Accordingly the fraction of the events that survived all the cuts was equal to the product of the fraction of the events that survived each cut. The ratio of the $K\pi\pi$ signal lost due to each kinematic cut (K^o_s effective mass cut or $K^o_s\pi^-\pi^+$ missing mass squared cut) to that of the $K\pi\pi$ signal under the Breit-Wigner shape in Fig. 23a should be equal to the ratio of the amount of signal (K^o_s or missing neutron) outside the $\pm 2\sigma$ cut of the kinematic quantity to that inside the cut. This was checked by fitting the K^o_s effective mass spectra (Figs. 11a and 11b) and the $K^o_s\pi^-\pi^+$ missing mass squared spectra (Figs. 10a and 10b) with kinematic cuts. The K^o_s effective mass spectra were fitted with a combination of two Gaussian forms (double-Gaussian)† and no background. The missing mass squared spectra were fitted with a double-Gaussian and a polynomial shaped background. In both cases the ratio of the signal outside the $\pm 2\sigma$ cut to that inside the $\pm 2\sigma$ cut was within $\sim$ 10% of the ratio of the $K\pi\pi$ signal lost in '1420' region due to the particular kinematic cut to the total $K\pi\pi$ signal under the Breit-Wigner form of '1420' in Fig. 23a.

vi. Empty Target Correction:

A small fraction of the events was from the interaction of the incident K^- with the vacuum jacket, support frames, etc. instead

---

† A poor fit was obtained with only one gaussian.

Table 23

Estimation of Event Loss by Kinematic Cut

Kinematic cut	Mass range of $K\pi\pi$ spectrum	Number of events in $K\pi\pi$ spectrum	Amount of $K\pi\pi$ signals in 1420	1750	Comments
$K\pi\pi$ missing mass squared	1.0 - 2.02	5,638	334	35	
$\bar{K}^0$ effective mass	1.0 - 2.02	3,763	981	47	
K_s^0-λ overlap	1.0 - 2.02	~ 40			negligible
$K_s^0\pi^-P$ missing mass squared	1.0 - 2.02	1,672	45		
*CHISQ/D.F. in constrained fit	1.0 - 2.02	~ 320			fitted with a polynomial background only

$\therefore$total '1420' events = 1,360†; average acceptance in this region = .181
$\therefore$total '1750' events = 82†; average acceptance in this region = .087

'therefore fraction of acceptance corrected events 'seen' in the '1420' peak
$= \frac{20,277}{27,791} = .730$

therefore fraction of acceptance corrected events 'seen' in the '1750' peak
$= \frac{3065}{4008} = .765$

* Not listed in Table 14

† $\Delta z/\delta z$ cut was not considered since it was incorporated in the Monte Carlo program to calculate the acceptance.

of the liquid hydrogen. Empty target runs were processed with the same analysis program and the summary tape processing program. The special records from them were processed as well. The cross section corresponding to this $K_s^o \pi^- \pi^+$ yield was calculated. The results are shown in Table 24. This was subtracted from the total cross section.

3. Differential and Total Cross Sections:

Table 20 shows the correction factors that were considered for calculating ε and α as well as the calculated values of ε and α. Table 25 lists the $|t'|$ intervals, the number of events and the cross sections corresponding to them. The errors shown are the statistical errors and the errors in acceptance calculation added in quadrature.

Table 26 shows the total number of acceptance corrected events obtained from fitting the total data (shown in Table 16a) for both the '1420' and the '1750' regions, and the corresponding cross-sections. It also lists the total number of acceptance corrected events in the '1420' peak obtained from adding the dn/dt in different t' intervals as listed in Table 25 and evaluating the contribution of the interval $\int \exp(bt')dt'$ as described earlier in Chapter V, and the corresponding cross section. The error listed for the fit to the total data is statistical only. That for the cross section obtained from $d\sigma/dt'$ is by adding the error from each t' bin in quadrature. Table 26 also lists the number of acceptance corrected events obtained from the empty target runs and the corresponding cross section. As shown in Table 24 there was no significant signal over background in the '1750' region from the empty target data.

The $\sigma \cdot Br$ obtained for the '1420' peak in the reaction

Table 24

Estimation of Yield from Empty Target

Number of runs with empty target	Total beam from scaler	Ratio of GDINC/TRIG for beam	Ratio of program count / scaler count for data trigger	Effective beam	Number of events in the mass region of 1420 1750		Average acceptance in the region of 1420 MeV 1750 MeV	
5	47, 389, 012	.8644	.9963	40.811×10^6	3*	1±1	.181	.087

*assuming signal to background ratio same as in the data.

TABLE 25

Differential Cross-Sections

$\|t'\|$ interval	number of acceptance corrected events	differential cross-section $d\sigma/dt'$ in μb
0.00 - 0.025	2877 ± 265	3.16 ± .29
0.025 - 0.050	2354 ± 250	2.59 ± .28
0.050 - 0.075	1898 ± 213	2.09 ± .23
0.075 - 0.10	1382 ± 180	1.52 ± .20
0.10 - 0.15	2033 ± 213	2.24 ± .23
0.15 - 0.20	2060 ± 231	2.27 ± .25
0.20 - 0.25	1345 ± 191	1.48 ± .21
0.25 - 0.30	979 ± 157	1.08 ± .17
0.30 - 0.40	1647 ± 188	1.81 ± .21
0.40 - 0.50	963 ± 164	1.06 ± .18
0.50 - 0.60	503 ± 121	0.55 ± .13
0.60 - 0.80	820 ± 150	0.90 ± .17
0.80 - 1.00	849 ± 154	0.93 ± .17

TABLE 26

Cross-Sections

Obtained From	Number of Acceptance in '1420' Region	Corrected Events in '1750' Region	σ.Br in μb For '1420'	σ.Br in μb For '1750'
fitting the total data	20,277 ± 334	3065	22.3 ± .4	3.4 ± .2
adding events from dn/dt'	19,808		21.8 ± .8	
empty target	17		.7	

$$K^- + p \rightarrow \bar{K}^{o*}(1420) + n$$
$$\hookrightarrow \bar{K}^o\pi^-\pi^+$$

was obtained to be $43.2^{\dagger} \pm .8$ μb where the error is statistical only. In addition an ∿10% systematic error was estimated. The cross section of the '1750' peak in the same branching channel was estimated as 6.8 ± 0.4 μb. Here again the error is only statistical and does not include the systematic error. From adding the cross sections obtained for each t' bin, between $|t'|$ of 0 and 1 and integrating in the $|t'|$ range of 1 and ∞, the total cross section of the '1420' in the $\bar{K}^o\pi^-\pi^+$ decay mode was 43.6 ± 1.5 μb.

Assuming the production of '1420' according to $d\sigma/dt' \propto e^{bt'}$, the value of b was found to be 5.3 ± 0.1 in the $|t'|$ range of 0.0 to 0.8 (Table 18). The error associated was obtained from the fit to the number of events in various $|t'|$ ranges vs. t' (Fig. 24).

4. Discussion:

Figure 25 shows a compilation of cross sections at various lab momenta (Ref. 7,38,39,40,41) with the current experimental point on it. The cross section obtained from this experiment is clearly consistent with the data points shown on the figure. The error associated with it is clearly much smaller relative to the neighboring points. The CERN experiment reported a cross section of ∿ 11 μb for the $J^P = 2^+$ $K^*(1420)$ at 10 GeV/c after a partial wave analysis (Ref. 7). Figure 25 shows this data point as well. No error was reported.

---

† Corrected for $\bar{K}^o$ unseen decay mode.

FIG. 25 PLOT OF THE CROSS SECTION AT VARIOUS INCIDENT K^- LAB MOMENTA FOR THE REACTION CHANNEL $K^-p \rightarrow \bar{K}^*(1420)^o + n$ $\hookrightarrow \bar{K}^o\pi^-\pi^+$

THE DATA POINTS AT 3.9 GeV/c AND 4.6 GeV/c WERE OBTAINED FROM THE TOTAL CROSS SECTION OF $K^*(1420)$ FOR THE REACTION $K^-p \rightarrow \bar{K}^*(1420)+n$ (REF. 41) AND THE BRANCHING RATIO OF $K^*(1420$ INTO $K\pi\pi$ ACCORDING TO THE PARTICLE DATA GROUP TABLES (REF. 2). STATISTICAL ERROR ON THE DATA POINT FROM THIS EXPERIMENT WAS APPROXIMATELY THE SIZE OF THE SYMBOL.

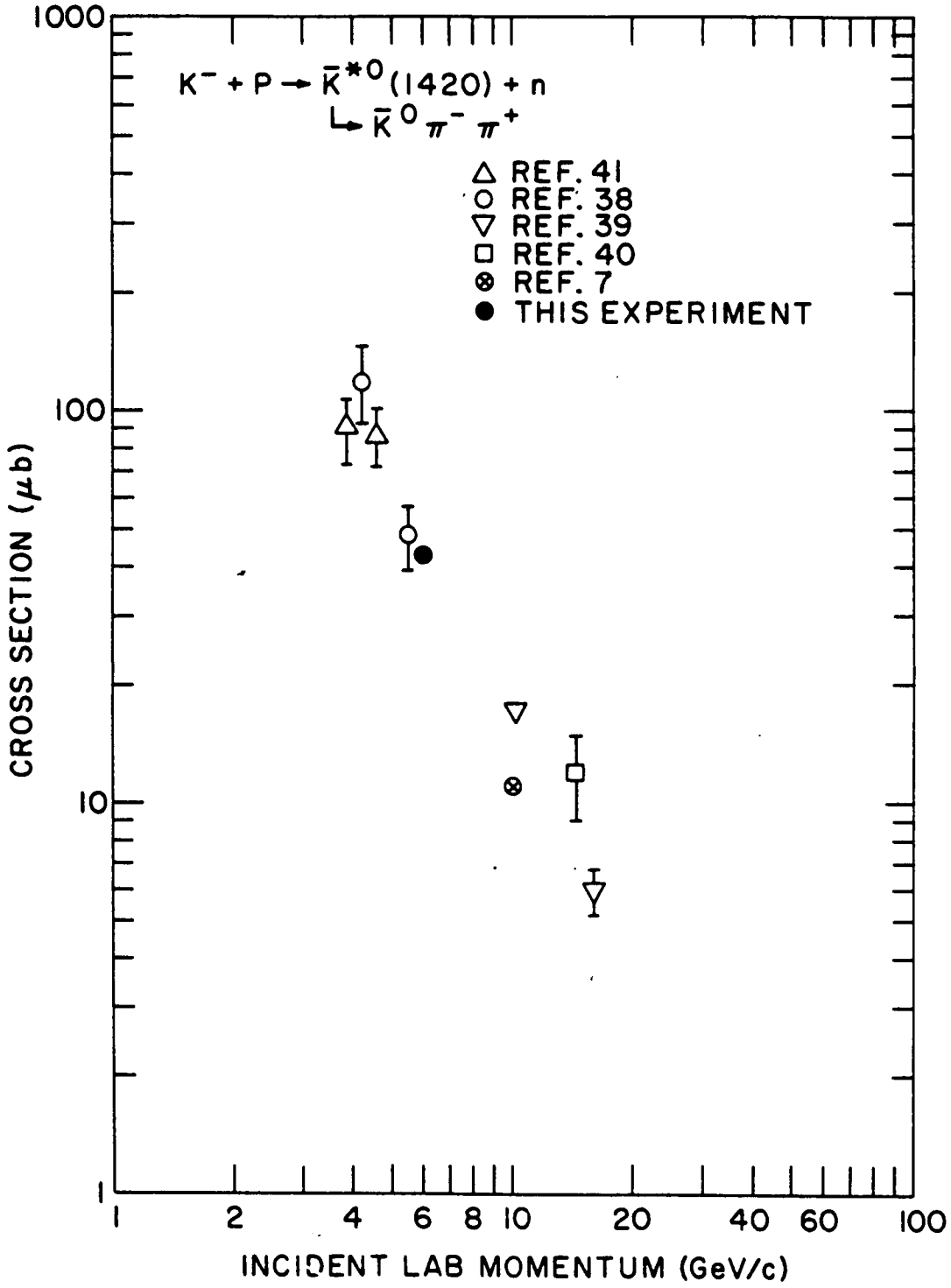
$K^- + P \rightarrow \bar{K}^{*0}(1420) + n$
$\hookrightarrow \bar{K}^0 \pi^- \pi^+$
REF. 41
REF. 38
REF. 39
REF. 40
REF. 7
THIS EXPERIMENT
CROSS SECTION (μb)
1000
100
10
1
1
2
4
6
8
10
20
40
60
100
INCIDENT LAB MOMENTUM (GeV/c)

Likewise, the slope obtained from fitting various ranges of the dn/dt' curve showed very definite indication of the flattening of the slope with increasing $|t'|$ observed in numerous experiments. When fitted by a single exponential, a slope of 5.3 $(GeV/c)^{-2}$ was obtained in the $|t'|$ range of 0.0 to 0.8 for an incident K^- momentum of 6 GeV/c.

CHAPTER VII

SUMMARY AND CONCLUSIONS

The present experiment represents the world's largest data sample in the reaction channel.

$$K^- + p \rightarrow K^o_s \pi^- \pi^+ + n$$

The data for the final analysis contained $\sim$ 14,000 events. After a careful kinematic analysis a very clear '1420' peak was observed. The mass and the width found were 1426 ± 2 MeV and 100 ± 6 MeV respectively. A cross section of 43.2 ± .8 μb was obtained for the reaction channel

$$K^- + p \rightarrow \bar{K}^*(1420) + n$$
$$\hookrightarrow \bar{K}^o \pi^- \pi^+$$

The error quoted is statistical. In addition, a systematic error of $\sim$ 10% was estimated. The cross section not only agreed well with the various experimental measurements at different momenta, but it established the cross section at 6 GeV/c with a very small error compared to the measurements at the neighboring momenta as seen from Fig. 25. The production slope obtained from the differential cross section ($d\sigma/dt' \propto e^{bt'}$) measurements was found to be 5.3 ± 0.1 in the $|t'|$ interval of 0.0 to 0.8. This also has a relatively small measurement error associated with it and was found consistent with numerous other experiments. In addition the slope was observed to be flatter in the higher $|t'|$ region, which is strongly indicative of the unnatural spin parity exchange (pion exchange) being mainly responsible at low $|t'|$ and the natural spin parity exchange (ρ,ω) being dominant at high $|t'|$ in the production mechanism.

In the 1700-1800 MeV region we observe a pronounced enhancement at $\sim$ 1750 MeV, of $\sim$ 114 MeV width. The cross section for the '1750' in the decay channel $\bar{K}^{o}\pi^{-}\pi^{+}$ was found to be $6.8 \pm .4\ \mu b$. The error shown is only statistical. However, an interesting effect was observed when the spectrum was investigated through various kinematic channels. The decay through $K^{*}(890)$ isobaric state showed a mass enhancement at $\sim$ 1780 MeV and the decay through $\bar{K}^{o}\pi^{-}\pi^{+}$ excluding the $K^{*}(890)$ intermediate state showed a pronounced peak at $\sim$ 1720 MeV. Hence, quite possibly there is more than one resonance in the mass region of 1700 - 1800 MeV, which in the total spectrum shows up as a single resonance at $\sim$ 1750 MeV.

To resolve the situation more definitively one needs to resort to the partial wave analysis, which with more statistics† would be undertaken.

---

† An extension of this experiment is due in 1979.

APPENDIX A

MAGNETIC FIELD COEFFICIENTS FOR EVALUATING THE MPS MAGNETIC FIELD

About ten thousand field coefficients were necessary to properly interpolate the MPS field at any given point. These coefficients were calculated for thirteen xy planes at z = 0, 50, 100, 125, 150, 162.5, 175, 187.5, 200, 212.5, 225, 237.5 and 250 cm (with z = 0 as the center of the magnet), and twenty-eight regions on each plane as shown below.

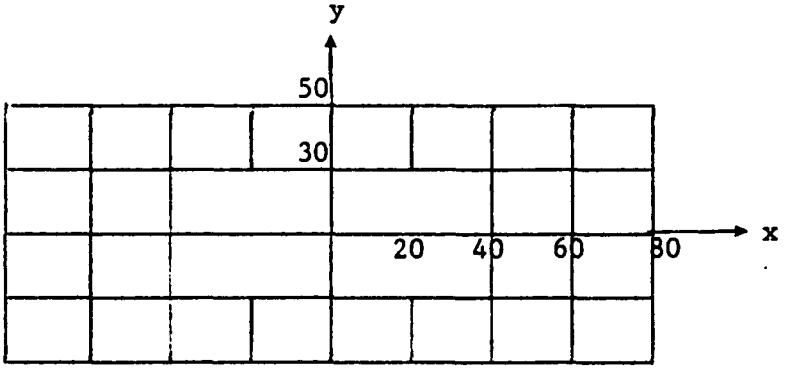

The field in the upstream half was calculated by using the symmetry under reflection about the z = 0 plane. In each region the field was expressed (for each of the three components) as

$$B_x = a_{x1} + a_{x2}x + a_{x3}x^2 + a_{x4}y + a_{x5}y^2 + a_{xi}xy$$

where i = 6, 7, 8, or 9 depending on the subregion. (Each region was divided into four equal sub-regions, the cross-term coefficients, a_{xi}'s, were different for each of them.) Similar expressions were used to express B_y and B_z at any point on a plane.

For an arbitrary point between the planes the following interpolation was done. In the central region B_z at $z = z_o$ (z_o < 100 cm)

was calculated by a linear interpolation, i.e.

$$B_z(x_o y_o z_o) = B_z(x_o y_o z_1) + \frac{\{B_z(x_o y_o z_2) - B_z(x_o y_o z_1)\}\ (z_o - z_1)}{(z_2 - z_1)}$$

where $B_z\ (x_o y_o z_1)$ and $B_z(x_o y_o z_2)$ were the z components of B at the two nearest xy planes ($z_1 < z_0 < z_2$) at $x = x_o$ and $y = y_o$. Beyond the central region ($100 < z_0 < 250$) a quadratic interpolation was used using the three equidistant xy planes nearest to $z = z_o$

$$B_z(x_o y_o z_o) = B_z(x_o y_o z_1) + \frac{[B_z(x_o y_o z_2) - B_z(x_o y_o z_1)](z_o - z_1)}{z_2 - z_1} +$$

$$\frac{1}{2}\,\frac{(z_o - z_1)(z_0 - z_2)[B_z(x_o y_o z_3) + B_z(x_o y_o z_1) - 2B_z(x_o y_o z_2)]}{(z_2 - z_1)(z_3 - z_2)}$$

where $z_1 < z_2 < z_3$; $z_1 < z_0 < z_3$.

B_{x_o} and B_{y_o} were expressed similarly (B_z's r laced by B_x's or B_y's). The field components were calculated in subroutine 'FIELD' given any x_o, y_o, z_o. The coefficients were stored in the large core memory (LCM) of the 7600.

APPENDIX B

WORKING PRINCIPLES OF 'GEOMETRY'

1. Least Squared Fit in 'GEOMETRY' to Obtain the Track Parameters:

The track coordinates for the ith data point were expressed in terms of the parameters as

$$S = S(u_i, x_o, y_o, \phi_o, s_o, c_o)$$

where

$x_o y_o \equiv$ x and y coordinates of the track at the upstream end of it;

$\phi_o \equiv$ azimuth of the track at the upstream end of it;

$S_o \equiv$ dip or pitch of the track at the upstream end of it;

$c_o \equiv$ curvature of the track at the upstream end;

$u_i \equiv$ arc length to the ith data point, and

$S \equiv$ the coordinate corresponding to the spark (x,y,u or v).

The deviation of the spark from the ith data point on the track is then

$$d_i = S_i^m - S_i(u_i;\beta_j); \quad j = 1, \text{---} 5 \text{ and } \beta\text{'s are track}$$

parameters. After a first order Taylor expansion about the approximate values $d_i^{(0)}$ corresponding to the initial values

$$d_i = d_i^{(0)} + \sum_{j=1}^{5} (\beta_i - \beta_j^{(0)}) \left(\frac{\partial d_i}{\partial \beta_j}\right)^{(0)}$$

Then χ^2, defined as

$$\sum_i \frac{d_i^2}{\sigma_i^2}$$

is at a minimum when

$$\frac{\partial \chi^2}{\partial \beta_\mu} = \frac{\partial}{\partial \beta_\mu} \sum_i \left[d_i^{(0)} + \sum_{j=1}^{5} (\beta_j - \beta_j^{(0)}) \left(\frac{\partial d_i}{\partial \beta_j}\right)^{(0)} \right] / \sigma_i^2 = 0$$

where $\mu \equiv 1,---,5$ and σ_i is the error associated with the ith measurement (and is discussed later). These equations, when solved for the β_j's yield

$$\boxed{\beta_j = \beta_j^{(0)} - \sum_{\mu=1}^{5} (G^{-1})_{j\mu} Y_\mu}$$

where $j = 1,----5$

$$Y_\mu = \sum_i \left(\frac{\partial d_i}{\partial \beta_\mu}\right)^{(0)} \frac{d_i^{(0)}}{\sigma_i}$$

$$G_{j\mu} = \sum_i \left(\frac{\partial d_i^{(0)}}{\partial \beta_j}\right) \cdot \frac{\partial d_i^{(0)}}{\partial \beta_\mu} \cdot \frac{1}{\sigma_i^2}$$

The β_j's were the best values of the track parameters. (The Y_μ and $G_{j\mu}$'s were calculated as the orbit was propagated through the MPS in stage two mentioned in the text in the explanation of the Geometry program package.

In stage three of the same subroutine, AUX calculated the inverse matrix $G^{-1}_{j\mu}$. It also evaluated the error matrix ε_{ij} (symmetric about the diagonal) where the final error was a combination of the

measurement error (chamber resolution in position measurement .1 cm for spark chamber and .3 cm for TPX) and the error due to multiple scattering.

An average σ_{ij}^2 (multiple scattering) was used assuming a kaon mass for the particular track at the momentum p obtained by the fit. The elements of σ_{ij}^2 were as following

$$\sigma_{11}^2 = < \delta\phi_{coul}^2 > = \frac{1k}{6 \cos^2\lambda}$$

$$\sigma_{22}^2 = < \delta S_{coul}^2 > = \frac{1k}{3 \cos^4\lambda}$$

$$\sigma_{33}^2 = < \delta q_{coul}^2 > = \frac{4k}{3 c_p^2 \, 1 \cos^4\lambda}$$

$$\sigma_{13}^2 = <\delta\phi\delta q_{coul} > = \frac{-k}{6 c_p \cos^4\lambda}$$

where the subscript coul stands for the contribution due to coulomb interaction and

l = the length of the track

k = mean squared angle of scattering per unit thickness

s = tan λ, pitch of the helix = dy/du

q = 1/p cos λ

c_p = a constant of magnetic field.

2. Working Principles of Subroutine 'XTRAPT'

Subroutine XTRAPT was called to swim a track from the ith data point to the plane of the i+1 th one. The arc-length between ith point and (z of) the plane of the i+1 th point was calculated using the parameters of the track at the ith point. If the projection of the arc

length on the xz plane was greater than 10 cm it was broken into segments of 10 cm (projected) length. (The last segment could be less.) Then the track was swum to the mid-point of the first arc segment where the value of the magnetic field was calculated by calling subroutine MFIELD (Appendix A). A new curvature corresponding to the center of the segment was then calculated using this value of the field. The track was now swum to the end of the first segment using the 'average' curvature of the segment. The swimming was done by using a circular extrapolation in the xz plane and a quadratic expression in y given as

$$y = y_o + x_o u + \frac{c_y u^2}{2}$$

where y_o and $s_o = dy/du$ are the values corresponding to the beginning of the segment and c_y = curvature calculated at the center of the segment. The procedure of swimming the track was repeated for each segment (using the curvature at the mid-point of the segment) until the last segment was used and the desired plane was reached approximately. A linear extrapolation was now done in xz to within .01 cm of the plane.

APPENDIX C

CALCULATION OF THE ACCEPTANCE MOMENTS

The Monte Carlo used for the calculation of the phase space acceptance was used in this case for the generation of the events. Approximately 320K events were generated per 100 MeV of K^{**} mass (M) above 1.5 GeV and $\sim$ 200K below 1.5 GeV. The mass range of K^{**} used was 1.1 to 2.24 GeV.

If α, β and γ were the three-ruler angles of the decay normal of $K^{o}_{s}\pi^{-}\pi^{+}$ in the Gottfried-Jackson frame of K^{**}, then $\cos\beta$ distribution was equivalent to that of the conventional $\cos\theta$ in the Gottfried-Jackson frame. Since no angular bias was imposed according to the spin or the polarization of the K^{**}, the generation of the events were uniform in α, $\cos\beta$ and γ. The phase space variables were the two Dalitz plot variables $M^{2}_{K\pi}$ and $M^{2}_{\pi^{-}\pi^{+}}$. So the five dimensional acceptance function was expressed as

$$a(M) = a(M, \alpha, \beta, \gamma, M^{2}_{\pi^{+}\pi^{-}}, M^{2}_{K^{o}\pi^{-}})$$

Once this distribution was obtained from the Monte Carlo, this was expressed as an expansion in a set of orthonormal functions in the five dimensional space as

$$I(R,r) = \sum_{LMN} \sum_{I=0}^{\infty} \sum_{K=0}^{I} \frac{(2L+1)}{(2\pi)^{3}} H(LMNIK) \cdot D^{L^{*}}_{MN}(R)\, \phi^{*}_{IK}(r) \qquad (1)$$

where $I(R,r)$ is the distribution $a(M, \alpha, \beta, \gamma, M^{2}_{\pi^{+}\pi^{-}}, M^{2}_{K\pi})$ averaged over an interval ΔM of M(ΔM = 40 MeV in this case)

R denotes the rotation angles α, β, γ;

$D^L_{MN}(R)$ denotes the rotation functions of order L

where $D^L_{MN}(R) = e^{iM}\, d^{\ell}_{mn}\, e^{iN}$

and $d^{\ell}_{mn} \equiv$ the small rotation function and form a complete set of orthonormal functions.

$\phi(r)$ forms a set of orthonormal functions in the Dalitz plot variables (r) in the phase space where r stands for T and θ. T and θ are found to form the orthonormal set $\phi(T\theta)$ and are different from $M_{K\pi}$ or $M^2_{\pi\pi}$.

θ_i is the angle between the K^o_s or the π^- in the $K^*(890)$ rest frame with the $K^*(890)$ direction in the $K^o_s\pi^-\pi^+$ rest frame.

T_i is defined as $\sin(T_i/2) = q_i/q_o$, $q_o = \max(q_i)$, where q_i = momentum of K^o_s in the K^* rest frame.

$q_i = q_o$ when π^+ has minimum momentum in the K^{**} rest frame.

The $\phi(T\theta)$ functions (of the order IK) are given as

$$\phi_{IK}(T\theta) = 2^K \Gamma(K+1)\, \left[(2K+1)\, \frac{(I+1)\,\Gamma(I-K+1)}{\Gamma(I+K+2)}\right]^{1/2}$$

$$\times\ e^{iK\pi/2} (\sin T)^K\, C^{K+1}_{I-K}(\cos T)\, P_K(\cos\theta)$$

$P_K(\cos\theta)$ is the Legendre Polynomial, $C^{K+1}_{I-K}(\cos T)$ is the Gegenbauer Polynomial ($I \geq K$), and

$$C^{\alpha}_n(\cos T) = \frac{1}{\Gamma(\alpha)} \sum_{m=0}^{n/2} (-)^m\, \frac{\Gamma(\alpha+n-m)}{m!\,(n-2m)!}\, (2\cos T)^{n-2m}$$

also $\phi_{ik}(T\theta)$ are normalized such that

$$\int \phi_{I'K'}(T\theta)\, \phi^*_{IK}(T\theta)\, dr = \pi \delta_{KK'} \delta_{II'}.$$

where dr is the phase space element $d(\cos T)\, d(\cos\theta)$ and $\phi_{00}(T\theta) = 1$.

In equation 1, H(LMNIK) are the coefficients of the products of D^L_{MN} and the ϕ_{IK} functions and are known as the 'acceptance moments'. $0 \leq M \leq (2L + 1)$; $-M \leq N \leq M$ are the ranges of M and N. The value of L is determined by how many terms are needed in the expansion for $I(R,\gamma)$ to represent $a(\alpha, \beta, \gamma, M^2_{\pi\pi}, M^2_{K\pi})$ properly.

The acceptance moments are determined by using

$$H(LMNIK) = \int dR dr\ D^L_{MN}(R)\ \phi_{ik}(\gamma)\ I(R\gamma)$$

with the normalization H(0000) = 1. Once the H's are obtained $I(R,\gamma)$ is expressed in terms of the polynomial. Then each event from the real data is read in, the five-dimensional phase space element occupied by it determined, and a weight (α 1/acc) corresponding to the number of events it is equivalent to is calculated.

BIBLIOGRAPHY

1. D.W.G.S. Leith, In Proceedings of the Fifth International Conference on Experimental Meson Spectroscopy, Boston, Mass., 1977, edited by E. von Goeler and R. Weinstein (Northeastern University Press, Boston, 1977) p. 207.

2. Review of Particle Properties; Particle Data Group, Rev. Mod. Phys., 48, #2, part II (1976).

3. D. Morgan, Phys. Lett. 51B, 71 (1974).

4. P. Lauscher et al., Nucl. Phys. B86, 189 (1975).

5. D. Vigraud et al., "PWA of the $K^+\pi^-$ system produced in $K^+n \to K^+\pi^-\overline{p}$ at 4.6, 8.25 and 12 GeV/c", paper submitted to the XVIII Int. Conf. on High Energy Physics, Tbilisi, July, 1976.

6. S.U. Chung, Private Communication.

7. E. Königs et al., Preprint Aachen III B/6-77 (1977); E. Königs et al., Phys. Lett. 74B, 282 (1978).

8. D.D. Carmony et al., Phys. Rev. Letts. 18, 615 (1967).

9. M. Jobes et al., Phys. Lett. 26B, 49 (1967).

10. S.U. Chung et al., Phys. Lett. 51B, 413 (1971).

11. G. Charriere et al., Nucl. Phys. B51, 317 (1972).

12. D.D. Carmony et al., Phys. Rev. Lett., 27, 1160 (1971).

13. A. Firestone et al., Phys. Letts. 36B, 513 (1971).

14. M. Aguilar-Benitez et al., Phys. Rev. Lett. 30, 672 (1973).

15. G.W. Brandenburg et al., Phys. Lett. 60B 478 (1976); G.W. Brandenburg et al., "The $K\pi$ system in the reactions $K^+p \to K^+\pi^-\Delta^{++}$ and $K^-p \to K^-\pi^+n$ at 13 GeV", paper submitted to the XVIII Int. Conf. on High Energy Physics, Tbilisi, July 1976.

16. M. Spiro et al., "New Evidence for K^* (1780) Production", SACLAY preprint, D.PhPE 75-12; Phys. Lett. 60B, 389 (1976).

17. M. Grassler et al., "Evidence for K^* (1850) Production in the Reaction $K^-p \to \overline{K}^-\pi^+ n$ at 10 and 16 GeV/c", paper submitted to the XVIII Int. Conf. on High energy Physics, Tbilisi, July 1976.

18. R. Baldi et al., "Observation of the K^* (1780) in the Reaction $K^+p \to K^0_s\pi^+p$ at 10 GeV/c", paper submitted to the XVIII Int. Conf. on High Energy Physics, Tbilisi, July 1976; R. Baldi et al., Phys. Lett. 63B, 344 (1976).

19. S.U. Chung et al., Phys. Rev. Lett. 40, 355 (1978).

20. G. Otter et al., Nucl. Phys. B106, 77 (1976); and other references therein.

21. R.J. Hemingway, in Proceedings of the Fifth International Conference on Experimental Meson Spectroscopy, Boston, Mass., 1977, edited by E. Von Goeler and R. Weinstein (Northeastern University Press, Boston, 1977) p.295.

22. J. Bartsch et al., Phys. Lett. 22, 357 (1966).

23. J. Bartsch et al., Phys. Lett. 33B, 186 (1970).

24. K. Barnham et al., Nucl. Phys. B25, 49 (1972).

25. P.J. Davis et al., Phys. Rev. D 5, 2688 (1972).

26. H.H. Bingham et al., PHys. Rev. D 5, 589 (1972).

27. D.C. Colley et al., Nucl. Phys. B26, 71 (1971).

28. M. Deutschmann et al., Phys. Lett. 49B, 388 (1974).

29. C.T. Murphy and J.D. Fox, "Characteristics of MESB: Description for Users", (EP&S-73-2), (1973), unpublished.

30. Eugene Halik, "Multiparticle Spectrometer Magnet (MPS)", MPS note No. 17, (1972), unpublished.

31. R.M. Edelstein, "Note on Beam Cerenkov Counters for MESB/MPS", MPS note No. 16, (1973), unpublished.

32. K.J. Foley et al., Nucl. Instrum. and Methods, 108, 33 (1973).

33. W. Love, M. Kramer, A. Saulys, "On-Line Programming for the MPS", MPS note No. 19, (1973), unpublished.

34. T. Morris, "Track Recognition Program", MPT note No. 9, (1972), unpublished.

35. T.W. Morris, "Skeleton Guide to TPX12, SXPLUS, and Other Conudrums", MPS note No., 33, (1975), unpublished.

36. T.W. Morris, "MPGP - Multi-Particle Geometry Program", MPS note NO. 18, (1973), unpublished.

37. S.M. Berman and M. Jacob, Phys. Rev. 139B, 1023 (1965).

38. F. Schweingruber et al., Phys. Rev. 166, 1317 (1968).

39. G. Otter et al., Nucl. Phys. B84, 331 (1975).

40. R. Barloutaud et al., Nucl. Phys. B59, 374 (1973).

41. M. Aguilar-Benitez et al., Phys. Rev. D 4, 2583 (1971).